Letter-of-Intent to PAC46

# Physics with Positron Beams at Jefferson Lab 12 GeV


John Arrington[1], Harut Avakian[4], Marco Battaglieri[2], Jan Bernauer[3], Angela Biselli[10], Mariangela Bondi'[12], Volker Burkert[4], Lawrence Cardman[4], Lucien Causse[5], Andrea Celentano[2], Pierre Chatagnon[5], Maxime Defurne[6], Raphaël Dupré[5], Mathieu Ehrhart[5], Latifa Elouadrhiri[4], Frédéric Georges[4], François-Xavier Girod[4], Joseph Grames[4], Michel Guidal[5], Ho-San Ko[5], Dominique Marchand[5], Luca Marsicano[2,7], Carlos Muñoz Camacho[5], Marzio De Napoli[12], Silvia Niccolai[5], Andrew Puckett[11], Axel Schmidt[3], Youri Sharabian[4], Daria Sokhan[8], Stepan Stepanyan[4], Michael Tiefenback[4], Raffaella De Vita[2], Eric Voutier[5], Rong Wang[5], Shenying Zhao[5]

[1] *Argonne National Laboratory*
*Physics Division*
*9700 S. Cass Avenue, Argonne, Illinois 60439, USA*

[2] *Istituto Nazionale di Fisica Nucleare*
*Sezione di Genova*
*Via Dodecaneso, 33 - 16146 Genova, Italia*

[3] *Laboratory for Nuclear Science*
*Massachusetts Institute of Technology*
*77 Massachusetts Avenue, Cambridge, Massachusetts 02139, USA*

[4] *Thomas Jefferson National Accelerator Facility*
*12000 Jefferson Avenue, Newport News, Virginia 23606, USA*

[5] *Institut de Physique Nucléaire*
*Université Paris-Sud & Paris-Saclay*
*15 rue Georges Clémenceau, 91406 Orsay cedex, France*

[6] *Institut de Recherche sur les Lois Fondamentales de l'Univers*
*Commissariat à l'Energie Atomique, Université Paris-Saclay*
*91191 Gif-sur-Yvette, France*

[7] *Universita' Di Genova*

*Via Balbi, 5 - 16126 Genova, Italia*

[8] *University of Glasgow*
*University Avenue, Glasgow G12 8QQ, United Kingdom*

[10] *Fairfield University*
*1073 N Benson Road, Fairfield, Connecticut 06824, USA*

[11] *University of Connecticut*
*Department of Physics*
*2152 Hillside Road, Storrs, Connecticut U-3046, USA*

[12] *Istituto Nazionale di Fisica Nucleare*
*Sezione di Catania*
*Via Santa Sofia, 64 - 95123 Catania, Italia*

Letter-of-Intent as of 30 May 2018

*Contact persons: grames@jlab.org, voutier@ipno.in2p3.fr*

**Abstract**

**Table of contents**

# 1 Introduction

Quantum Electrodynamics (QED) is one of the most powerful quantum physics theories. The highly accurate predictive power of this theory allows not only to investigate numerous physics phenomena at the macroscopic, atomic, nuclear, and partonic scales, but also to test the validity of the Standard Model. Therefore, QED promotes electrons and positrons as unique physics probes, as demonstrated worldwide over decades of scientific research at different laboratories.

Both from the projectile and the target point of views, spin appears nowadays as the finest tool for the study of the inner structure of matter. Recent examples from the experimental physics program developed at the Thomas Jefferson National Accelerator Facility (JLab) include: the measurement of polarization observables in elastic electron scattering off the nucleon [Jon00, Gay02, Puc10], that established the unexpected magnitude and behaviour of the proton electric form factor at high momentum transfer (see [Pun15] for a review); the experimental evidence, in the production of real photons from a polarized electron beam interacting with unpolarized protons, of a strong sensitivity to the orientation of the longitudinal polarization of the electron beam [Ste01], that opened the investigation of the 3-dimensional partonic structure of nucleons and nuclei via the Generalized Parton Distributions (GPDs) [Mul94] measured through the Deeply Virtual Compton Scattering (DVCS) [Ji97, Rad97]; the achievement of a unique parity violation experimental program [Arm05, Ani06, And13] accessing the smallest polarized beam asymmetries ever measured ($\sim 10^{-7}$), which provided the first determination of the weak charge of the proton [And13] and allowed for stringent tests of the Standard Model at the TeV mass-scale [You06]; etc. Undoubtebly, polarization became an important capability and a mandatory property of the current and next generation of accelerators.

The combination of the QED predictive power and the fineness of the spin probe led to a large but yet limited variety of impressive physics results. Adding to this tool-kit charge symmetry properties in terms of polarized positron beams will provide a more complete and accurate picture of the physics at play, independently of the size of the scale involved. In the context of the experimental study of the structure of hadronic matter carried out at JLab, the electromagnetic interaction dominates lepton-hadron reactions and there is no stringent difference between the physics information obtained from the scattering of electrons or positrons off an hadronic target. However, every time a reaction process is a conspiracy of more than one elementary mechanisms, the comparison between electron and positron scattering allows us to isolate the quantum interference between these mechanisms. This is of particular interest for studying limitations of the one-photon exchange Born approximation in elastic and inelastic scatterings [Gui03]. It is also essential for the experimental determination of the GPDs where the interference between the known Bethe-Heitler (BH) process and the unknown DVCS requires polarized and unpolarized electron and positron beams for a model independent extraction of the different contributions to the cross section [Vou14]. Such polarized lepton beams also provide the ability to test new physics beyond the frontiers of the Standard Model via the precise measurement of electroweak coupling parameters [Zhe09] or the search for new particles related to dark matter [Woj09, Mar17].

The production of high-quality polarized positron beams to suit these many applications remains however a highly difficult task that, until recently, was feasible only at large scale accelerator facilities. Relying on the most recent advances in high polarization and high intensity electron sources [Add10], the PEPPo (Polarized Electrons for Polarized Positrons) technique [Abb16], demonstrated at the injector of the Continuous Electron Beam Accelerator Facility (CEBAF), provides a novel and widely accessible approach based on the production, within a tungsten target, of polarized $e^+e^-$ pairs from the circularly polarized bremsstrahlung radiation of a low energy highly polarized electron beam. As opposed to other schemes operating at GeV lepton beam energies [Sok64, Omo06, Ale08], the operation of the PEPPo technique requires only energies above the pair-production threshold and is therefore ideally suited for a polarized positron beam at CEBAF.

This letter presents the physics merits and technical challenges of an experimental program with high energy unpolarized and polarized positron beams at Jefferson Lab. The next section discusses the benefit of a positron beam on the basis of the additional experimental observables available for elastic scattering and deeply virtual Compton scattering off the nucleon, and for the dark matter search. The following section discusses the possible schemes for implementing a PEPPo-based positron beam at CEBAF, particularly beam production and transport issues, and the necessary R&D effort toward this end. The next sections are composed of specific letters describing in details the physics motivations and experimental configuration of a given measurement using the proposed 11 GeV positron beam. The corresponding positron experimental program is summarized in the last section.

## 2 Physics motivations

### *2.1 Elastic lepton scattering*

The measurement of the electric form factor of the nucleon ($G_E$) at high momentum transfer, in the perspective of the experimental assessment of perturbative Quantum Chromo-Dynamics (QCD) scaling laws [Bro81], motivated an intense experimental effort supported by the advent of high energy continuous polarized electron beams. Indeed, the polarization observables technique [Akh74, Arn81] is expected to be more sensitive to $G_E$ than the cross section method relying on a Rosenbluth separation [Ros50]. However, the strong disagreement between the results of these two experimental methods (Fig. 1) came as a real surprise. Following the very first measurements of polarization transfer observables in the $^1\mathrm{H}(\vec{e},e\vec{p})$ reaction [Jon00], the validity of the Born approximation for the description of the elastic scattering of electrons off protons was questioned. The eventual importance of higher orders in the

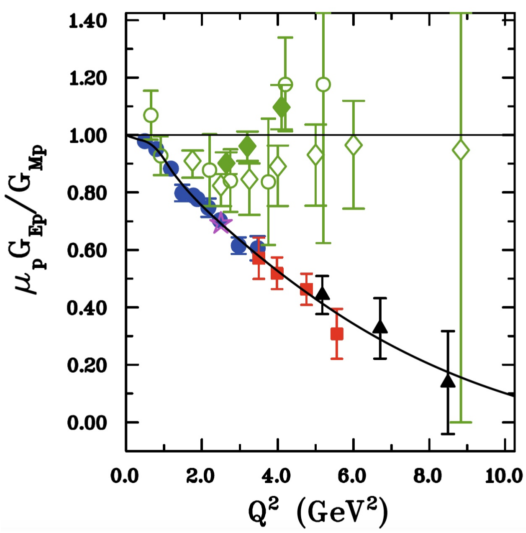


Figure 1. Rosenbluth (green symbols) and polarization transfer (blue, red, and black symbols) experimental data for the ratio between the electric and magnetic form factor of the proton, together with an empirical fit of polarization data [Pun15].

$\alpha$-development of the electromagnetic interaction was suggested [Gui03] as a hypothesis to reconciliate cross section and polarization transfer experimental data. This prevents a model-independent experimental determination of the nucleon electromagnetic form factors via only electron scattering.

Considering the possible existence of second-order contributions to the electromagnetic current, the so-called $2\gamma$-exchange, the $eN$-interaction is no longer characterized by 2 real form factors but by 3 generalized complex form factors

$$\widetilde{G}_M = e\,G_M + \delta\widetilde{G}_M\,, \quad \widetilde{G}_E = e\,G_E + \delta\widetilde{G}_E\,, \quad \widetilde{F}_3 = \delta\widetilde{F}_3\,, \tag{1}$$

where $e$ represents the lepton beam charge. These expressions involve up to 8 unknown real quantities that should be recovered from experiments [Rek04]. Considering unpolarized leptons, the non point-like structure of the nucleon can be expressed by the reduced cross section

$$\begin{aligned}\sigma_R^e = \tau G_M^2 + \epsilon G_E^2 + 2e\,\tau G_M\,\Re e\left[\delta\widetilde{G}_M\right] \\ + 2e\,\epsilon\,G_E\,\Re e\left[\delta\widetilde{G}_E\right] + e\sqrt{\tau(1-\epsilon^2)(1+\tau)}G_M\,\Re e\left[\delta\widetilde{F}_3\right]\end{aligned} \tag{2}$$

where the charge-dependent terms denote the additional contributions from the $2\gamma$-exchange mechanisms. The variable $\epsilon$ characterizing, in the $1\gamma$-exchange approximation, the virtual photon polarization can be written as

$$\epsilon = \left[1 - 2\frac{\vec{q}\cdot\vec{q}}{Q^2}\tan^2\left(\frac{\theta_e}{2}\right)\right]^{-1} \tag{3}$$

where $\theta_e$ is the electron scattering angle, and $q \equiv (\vec{q}, \omega)$ is the virtual photon with four-mometum transfer $Q^2{=}-q\cdot q$, and $\tau{=}Q^2/4M^2$ with $M$ representing

the nucleon mass. In absence of lepton beams of opposite charge, the Rosenbluth method, consisting in the measurement of the reduced cross section at different $\epsilon$-values while keeping $Q^2$ constant, allows the determination of a combination of $1\gamma$ and $2\gamma$ electromagnetic form factors. Consequently, it requires a model-dependent input to further separate the electric and magnetic form factors.
The transfer of longitudinal polarization by a lepton beam via scattering elastically off a nucleon, provides 2 additional linear combinations of the same physics quantities in the form of the transverse ($P_t^e$) and longitudinal ($P_l^e$) polarization components of the nucleon

$$\begin{aligned} \sigma_R^e \, P_t^e &= -\,\lambda\,\sqrt{2\epsilon\tau(1-\epsilon)}\,\Bigg( G_E G_M + e\,G_E \Re e\left[\delta\widetilde{G}_M\right] \\ &\qquad + e\,G_M \Re e\left[\delta\widetilde{G}_E\right] + e\,\sqrt{\frac{1+\epsilon}{1-\epsilon}} G_E \Re e\left[\delta\widetilde{F}_3\right]\Bigg) \end{aligned} \tag{4}$$

$$\sigma_R^e P_l^e = \lambda\,\tau\sqrt{1-\epsilon^2}\left(G_M^2 + e\,\left[2+\sqrt{\frac{1+\tau}{\tau(1-\epsilon)}}\,\right] G_M \Re e\left[\delta\widetilde{F}_3\right]\right), \tag{5}$$

where $\lambda$ is the lepton-beam polarization. The combination of polarized and unpolarized beam observables for elastic electron scattering involves up to 6 unknown real quantities, requiring at least 6 independent experimental observables. Therefore, taking into account $2\gamma$-exchange mechanisms electron beams alone can no longer provide a pure experimental determination of the electromagnetic form factors of the nucleon. However, comparing polarized electron and positron beams, one can separate the charge-dependent and independent contributions of experimental observables, andthus separate the $1\gamma$ and $2\gamma$ form factors. For instance,

$$\frac{\sigma_R^+ + \sigma_R^-}{2} = \tau G_M^2 + \epsilon G_E^2 \tag{6}$$

$$\begin{aligned} \frac{\sigma_R^+ - \sigma_R^-}{2} &= 2\tau G_M\,\Re e\left[\delta\widetilde{G}_M\right] \\ &\quad + 2\,\epsilon\,G_E\,\Re e\left[\delta\widetilde{G}_E\right] + \sqrt{\tau(1-\epsilon^2)(1+\tau)}G_M\,\Re e\left[\delta\widetilde{F}_3\right] \end{aligned} \tag{7}$$

and similarly for polarized observables. Consequently, the measurement of polarized and unpolarized elastic scattering of both electrons and positrons provides the necessary data for a model-independent determination of the nucleon electromagnetic form factors.

### *2.2 Deep inelastic lepton scattering*

The understanding of the partonic structure and dynamics of hadronic matter is one of the major goals of modern Nuclear Physics. The availability of high intensity continuous polarized electron beams with high energy together

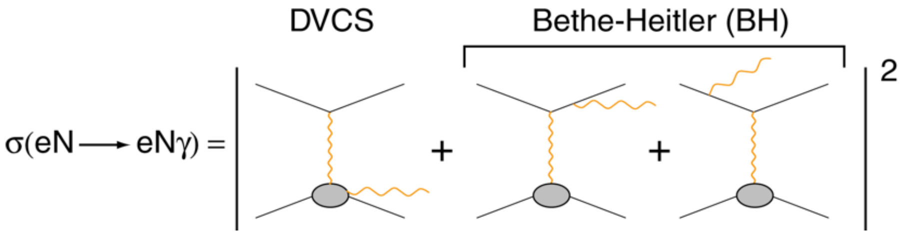


Figure 2. Lowest order QED amplitude of the electroproduction of real photons off nucleons.

with performant detector systems at different facilities is providing today an unprecedented but still limited insight into this problem. Similarly to the elastic scattering case, the combination of measurements with polarized electrons and polarized positrons in the deep inelastic regime will allow to obtain unique experimental observables enabling a more accurate and refined interpretation.

The GPD framework [Mul94] constitutes the most appealing and advanced parameterization of hadron structure. It encodes the internal structure of matter in terms of quarks and gluons and unifies within the same framework electromagnetic form factors, parton distributions, and the description of the nucleon spin (see [Die03, Bel05] for a review). GPDs can be interpreted as the probability to find a parton at a given transverse position and carrying a certain fraction of the longitudinal momentum of the nucleon. The combination of longitudinal and transverse degrees of freedom is responsible for the richness of this universal framework.

GPDs are involved in any deep process and are preferentially accessed in hard lepto-production of real photons (i.e. DVCS). This process competes with the known BH reaction [Bet34] where real photons are emitted from the initial or final leptons instead than from the probed hadronic state (Fig. 2). The lepton beam charge and polarization dependence of the $eN(A)\gamma$ cross section off nucleons(nuclei) writes [Die09]

$$\sigma^{e}_{\lambda 0} = \sigma_{BH} + \sigma_{DVCS} + \lambda\,\widetilde{\sigma}_{DVCS} + e\,\sigma_{INT} + e\lambda\,\widetilde{\sigma}_{INT} \tag{8}$$

where the index $INT$ denotes the interference contribution to the cross section originating from the quantum interference of the BH and DVCS processes. Polarized electron scattering provides the experimental observables

$$\sigma^{-}_{00} = \frac{\sigma^{-}_{+0} + \sigma^{-}_{-0}}{2} = \sigma_{BH} + \sigma_{DVCS} - \sigma_{INT}\,, \tag{9}$$

$$^{1}\Delta^{-}_{\lambda 0} = \frac{\sigma^{-}_{+0} - \sigma^{-}_{-0}}{2} = \lambda\,\left[\widetilde{\sigma}_{DVCS} - \widetilde{\sigma}_{INT}\right] \tag{10}$$

involving unseparated combinations of the unknwon $INT$ and $DVCS$ reaction amplitudes. The comparison between polarized electron and polarized positron reactions provides the additional observables

$$\Delta\sigma_{00} = \frac{\sigma_{00}^{+} - \sigma_{00}^{-}}{2} = \sigma_{INT} \tag{11}$$

$$^{2}\Delta_{\lambda 0} = \frac{^{1}\Delta_{\lambda 0}^{+} - {}^{1}\Delta_{\lambda 0}^{-}}{2} = \lambda\, \widetilde{\sigma}_{INT} \tag{12}$$

which isolate the interference amplitude. Consequently, measuring real photon lepto-production off nucleons with opposite charge polarized leptons allows to separate the four unknown contributions to the $eN\gamma$ cross section.
For a spin $s$ hadron, one can define $(2s+1)^2$ parton-helicity conserving and chiral-even elementary GPDs that can be accessed through DVCS. They appear in the reaction amplitudes in the form of unseparated linear and bilinear expresssions. Their separation requires additional observables that can be obtained considering polarized targets ($S$) [Bel02]. The full lepton beam charge and polarizations dependence of the $eN\gamma$ cross section can be written as [Die09]

$$\begin{aligned} \sigma_{\lambda S}^{e} = {} & \sigma_{\lambda 0}^{e} \\ & + S\left[\lambda\, \Delta\sigma_{BH} + \lambda\, \Delta\sigma_{DVCS} + \Delta\widetilde{\sigma}_{DVCS} + e\lambda\, \Delta\sigma_{INT} + e\, \Delta\widetilde{\sigma}_{INT}\right] , \end{aligned} \tag{13}$$

where $\Delta\sigma_{BH}$ is the known sensitivity of the BH process to the target polarization and the remaining terms feature four combinations of the nucleon GPDs to be isolated. Polarized electron scattering provides the combinations

$$^{1}\Delta\sigma_{0S}^{-} = \frac{\sigma_{0+}^{-} - \sigma_{0-}^{-}}{2} = S\,\left[\Delta\widetilde{\sigma}_{DVCS} - \Delta\widetilde{\sigma}_{INT}\right] \tag{14}$$

$$^{2}\Delta_{\lambda S}^{-} = \frac{^{1}\Delta_{\lambda +}^{-} - {}^{1}\Delta_{\lambda -}^{-}}{2} = S\,\lambda\,\left[\Delta\sigma_{BH} + \Delta\sigma_{DVCS} - \Delta\sigma_{INT}\right] \tag{15}$$

and the comparison between polarized electrons and positrons yields

$$^{2}\Delta\sigma_{0S} = \frac{^{1}\Delta\sigma_{0S}^{+} - {}^{1}\Delta\sigma_{0S}^{-}}{2} = S\,\Delta\widetilde{\sigma}_{INT} \tag{16}$$

$$^{3}\Delta_{\lambda S} = \frac{^{2}\Delta_{\lambda S}^{+} - {}^{2}\Delta_{\lambda S}^{-}}{2} = S\,\lambda\,\Delta\sigma_{INT}\,, \tag{17}$$

which once again isolates the interference contribution and allows to separate the four reaction amplitudes of interest.
Therefore, polarized positron beams appear as a necessary complement to polarized electron beams to achieve a model-independent determination of nucleon GPDs.

### *2.3 Test of the Standard Model*

... to continue...

## 3 Polarized positron beam at CEBAF

... to continue...

## 4 TPE @ CLAS12 & Hall A/C

# Studying two-photon exchange contributions in elastic $e^+$-p and $e^-$-p scattering at Jefferson Lab


### Abstract

The proton elastic form factor ratio can be measured either via Rosenbluth separation in an unpolarized beam and target experiment, or via the use of polarization degrees of freedom. However, data produced by these two approaches show a discrepancy, increasing with $Q^2$. The proposed explanation of this discrepancy – two-photon exchange – has been tested recently by three experiments. The results support the existence of a small two-photon exchange effect but cannot establish that theoretical treatment at the measured momentum transfers are valid. At larger momentum transfers, theory remains untested, and without further data, it is impossible to resolve the discrepancy. A positron beam at Jefferson Lab allows us to directly measure two-photon exchange over an extended $Q^2$ and $\varepsilon$ range with high precision. With this, we can validate whether the effect reconciles the form factor ratio measurements, and test several theoretical approaches, valid in different parts of the tested $Q^2$ range.



*Spokesperons: J. Bernauer (bernauer@mit.edu), A. Schmidt (schmidta@mit.edu), J. Arrington, V. Burkert*

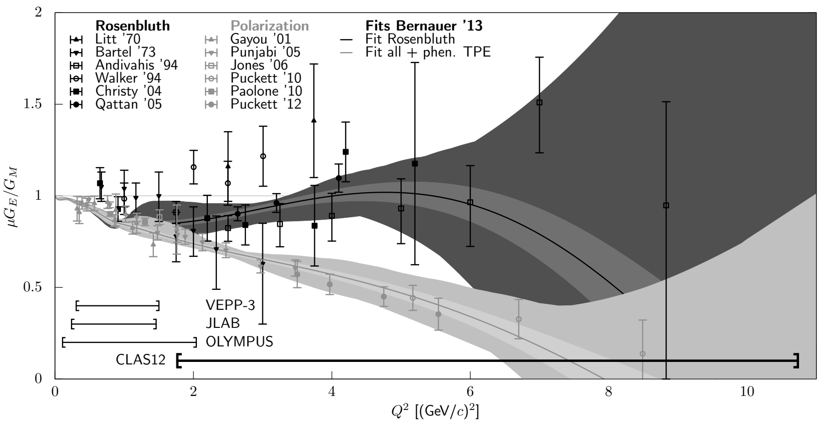


Figure 3. The proton form factor ratio $\mu G_E/G_M$, as determined via Rosenbluth-type (black points, from [Lit70, Bar73, And94, Wal94, Chr04, Qat05]) and polarization-type (gray points, from [Gay01, Pun05, Jon06, Puc10, Pao10, Puc12]) experiments. While the former indicate a ratio close to 1, the latter show a distinct linear fall-off. Curves are from a phenomenological fit [Ber14], to either the Rosenbluth-type world data set alone (dark curves) or to all data, then including a phenomenological two-photon-exchange model. We also indicate the coverage of earlier experiments as well as of the experiment described below.

Over more than half a century, proton elastic form factors have been studied in electron-proton scattering with unpolarized beams. These experiments have yielded data over a large range of four-momentum transfer squared, $Q^2$. The form factors were extracted from the cross sections via the so-called Rosenbluth separation. Among other things, they found that the form factor ratio $\mu G_E/G_M$ is in agreement with scaling, i.e., that the ratio is constant. Somewhat more recently, the ratio of the form factors was measured using polarized beams, with different systematics and increased precision especially at large $Q^2$. However, the results indicate a roughly linearly fall-off of the ratio. The result of the different experimental methods, as well as some recent fits, are compiled in Fig. 3. The two data sets are clearly inconsistent with each other, indicating that one method (or both) are failing to extract the proton's true form factors. The resolution of this "form factor ratio puzzle" is crucial to advance our knowledge of the proton form factors, and with that, of the distribution of charge and magnetization inside the proton.

The differences observed by the two methods have been attributed to two-photon exchange (TPE) effects [Gui03, Car07, Arr11, Afa17], which are much more important in the Rosenbluth method than in the polarization transfer method, where they partially cancel out in the ratio. Two-photon exchange corresponds to a group of diagrams in the second order Born approximation of lepton scattering, namely those where two photon lines connect the lepton and proton. The so-called "soft" case, when one of the photons has negligible momentum, is included in the standard radiative corrections, like Ref. [Mo69, Max00], to cancel infrared divergences from other diagrams. The "hard" part, where both photons can carry considerable momentum, is not. It is important to note here that the division between soft and hard part is arbitrary, and

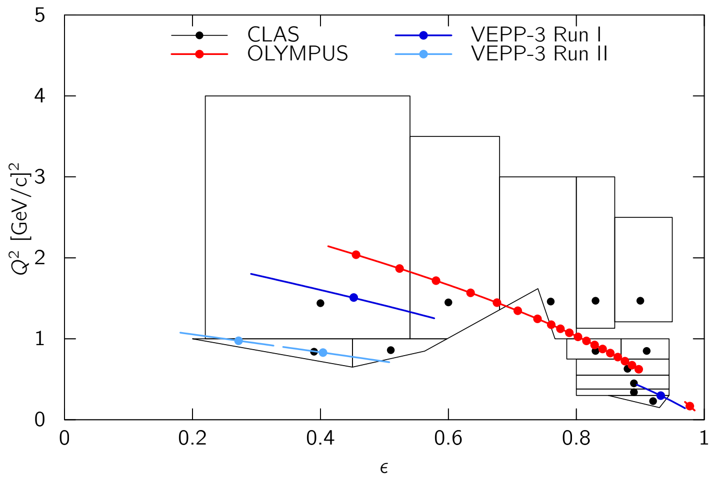


Figure 4. Kinematics covered by the three recent experiments to measure the two-photon exchange contribution to the elastic $ep$ cross section.

different calculations use different prescriptions.

It is obviously important to study this proposed solution to the discrepancy with experiments that have sensitivity to two-photon contributions. The most straightforward process to evaluate two-photon contribution is the measurement of the ratio of elastic $e^+p/e^-p$ scattering. Several experiments have recently been carried out to measure the 2-photon exchange contribution in elastic scattering: the VEPP-3 experiment at Novosibirsk [Rac15], the CLAS experiment at Jefferson Lab [Mot13, Adi15, Rim17], and the OLYMPUS experiment at DESY [Hen17]. The kinematic reach of these experiments was limited, however, as shown in Fig. 4. The combined evaluation of all three experiments led the authors of the review [Afa17] to the conclusion that although the results show that the hypothesis of the absence of two-photon effects is excluded with 99.5% confidence, "The results of these experiments are by no means definitive", and that "There is a clear need for similar experiments at larger $Q^2$ and at $\varepsilon < 0.5$".

In this letter, we propose a new definitive measurement of the TPE effect that would be possible with a positron source at CEBAF. By alternately scattering positron and electron beams from a liquid hydrogen target and detecting the scattered lepton and recoiling proton in coincidence with the large acceptance CLAS-12 spectrometer, the magnitude of the TPE contribution between $Q^2$ values of 2 and 10 GeV$^2$ could be significantly constrained. With such a measurement, the question of whether or not TPE is at the heart of the "proton form factor puzzle" could be answered.

Another option is use of the Super-Rosenbluth technique, a Rosenbluth separation using only proton detection. This approach is less sensitive to the difference between electron and positron beam runs, allowing for a precise study of TPE effects with a positron-only measurement (combined with existing electron data). The $Q^2$ range is lower, from 0.4 GeV$^2$ to 4-5 GeV$^2$, and the measurement extracts the TPE contribution to the $\varepsilon$-dependence of the cross section, rather than the cross section at a fixed value of $Q^2$ and $\varepsilon$. However, it does not require frequent changes between electron and positron beams, and is less sensitive to beam quality issues.

### 4.2 Previous work

One significant challenge is that hard TPE cannot be calculated in a model-independent way. There are several model-dependent approaches. A full description of the available theoretical calculations are outside of the scope of this letter. Suffice it to say that they can be roughly divided into two groups: hadronic calculations, e.g. [Blu17], which should be valid for $Q^2$ from 0 up to a couple of GeV$^2$, and GPDs based calculations, e.g. [Afa05], which should be valid from a couple of GeV$^2$ and up.

Three contemporary experiments have tried to measure the size of TPE, based at VEPP-3 [Rac15], Jefferson Lab (CLAS, [Mot13, Adi15, Rim17]) and DESY (OLYMPUS, [Hen17]). These experiments measured the ratio of positron-proton to electron-proton elastic cross sections. The next order correction to the first order Born calculation of the elastic lepton-proton cross section contains terms corresponding to the product of the diagrams of one-photon and two-photon exchange. These terms change sign with the lepton charge sign. It is therefore possible to determine the size of TPE by measuring the ratio of positron to electron scattering:

$$R_{2\gamma} = \frac{\sigma_{e^+}}{\sigma_{e^-}} \approx 1 + 2\delta_{TPE}\,. \tag{18}$$

The kinematic reach of the three experiments is shown in Fig. 4. The kine-

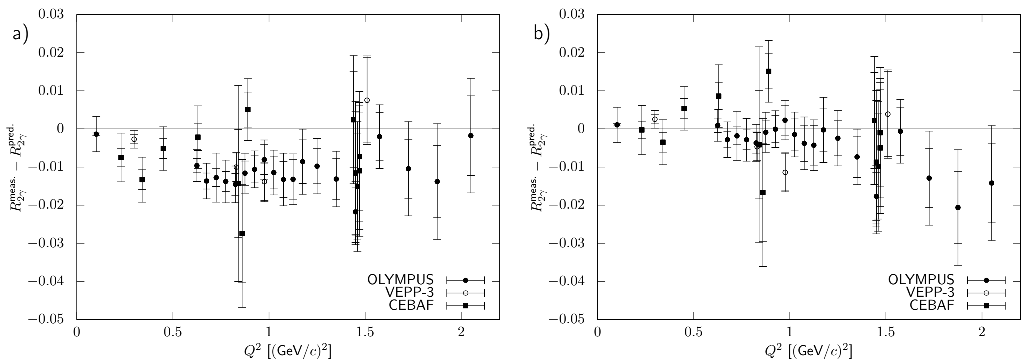


Figure 5. Difference of the data of the three recent TPE experiments [Rac15, Rim17, Hen17] to the calculation in [Blu17] (a) and the phenomenological prediction from [Ber14] (b).

matic coverage in these experiments is limited to $Q^2 < 2$ GeV$^2$, and $\varepsilon > 0.5$, where the two-photon effects are expected to be small, and systematics of the measurements must be extremely well controlled. Figure 5 depicts the difference of the data of the three experiments to the calculation by Blunden et al. [Blu17] and the phenomenological prediction by Bernauer et al. [Ber14]. It can be seen that the three data sets are in good agreement which each other, and appear about 1% low compared to the calculation. The prediction appears closer for most of the $Q^2$ range, however over-predicts the effect size at large $Q^2$. This is worrisome, as this coincides with the opening of the divergence in the fits depicted in Fig. 3 and might point to an additional effect beyond TPE that drives the difference. The combination of the experiments prefer the phenomenological prediction with a reduced $\chi^2$ of 0.68, the theoretical calculation achieves a reduced $\chi^2$ of 1.09, but is ruled out by the normalization information of both the CLAS experiment and OLYMPUS to a 99.6% confidence level. No hard TPE is ruled out with a significantly worse reduced $\chi^2$ of 1.53.

The current status can be summarized as such:

- TPE exists, but is small in the covered region;
- Hadronic theoretical calculations, supposed to be valid in this kinematical regime, might not be good enough yet;
- Calculations based on GPDs, valid at higher $Q^2$, are so far not tested at all by experiment;
- A comparison with the phenomenological extraction allows for the possibility that the discrepancy might not stem from TPE alone.

We refer to [Afa17] for a more in-depth review. The uncertainty in the resolution of the ratio puzzle jeopardizes the extraction of reliable form factor information, especially at high $Q^2$, as covered by the Jefferson Lab 12 GeV program. Clearly, new data are needed.

### *4.3 Experimental configuration*

Both theories and phenomenological extractions predict a roughly proportional relationship of the TPE effect with $1-\varepsilon$ and a sub-linear increase with $Q^2$. However, interaction rates drop sharply with smaller $\varepsilon$ and higher $Q^2$, corresponding to higher beam energies and larger electron scattering angles. This puts the interesting kinematic region out of reach for storage-ring experiments, and handicaps external beam experiments with classic spectrometers with comparatively small acceptance.

With the large acceptance of CLAS12, combined with an almost ideal coverage of the kinematics, measurements of TPE across a wide kinematic range are possible, complementing the precision form factor program of Jefferson Lab, and testing both hadronic (valid at the low $Q^2$ end) as well as GPD-based (valid at the hight $Q^2$-end) theoretical approaches. Figure 6 shows the angle coverage for both the electron (left) and for the proton (right). There is a one-to-one correlation between the electron scattering angle and the proton recoil angle. For the kinematics of interest, say $\varepsilon < 0.6$ and $Q^2 > 2$ GeV$^2$ for the chosen beam energies from 2.2 to 6.6 GeV, nearly all of the electron scattering angles falls into a polar angle range from 40° to 125°, and corresponding to the proton polar angle range from 8° to 35°. These kinematics are most suitable for accessing the two-photon exchange contributions. The setup will also be able to measure the reversed kinematics with the electrons at forward angle and the protons at large polar angles. This is in fact the standard CLAS12

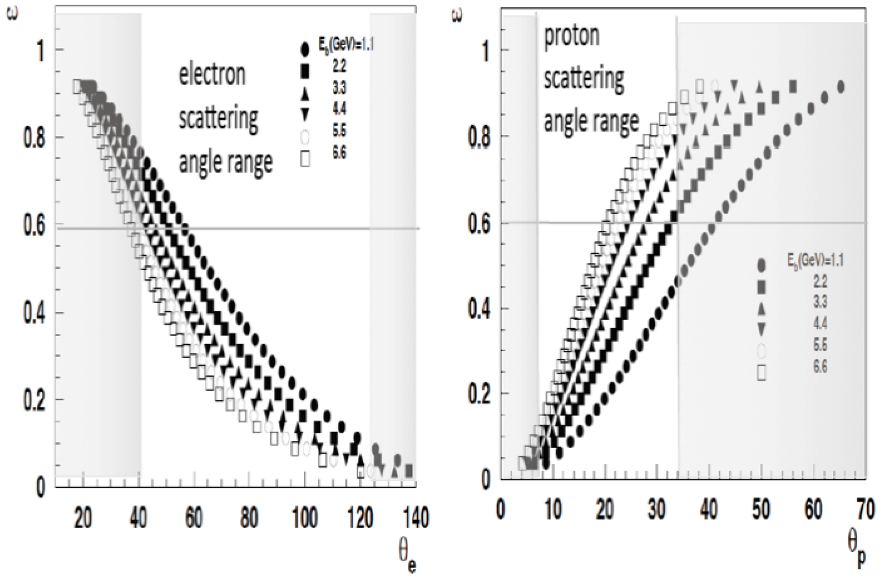


Figure 6. Polar angle and $\varepsilon$ coverage for electron detection (left) and for proton detection (right).

configuration of DVCS and most other experiments. While the two-photon exchange is expected to be small in this range, the sign change in TPE seen in the experiments, but not predicted by current theories, can be studied. Figure 7 shows the expected elastic scattering rates covering the ranges of highest interest, with $\varepsilon < 0.6$ and $Q^2 = 2-10\ \mathrm{GeV}^2$. Sufficiently high statistics can be achieved within 10 hrs for the lowest energy and within 1000 hrs for the highest energy, to cover the full range in kinematics. Note that all kinematic bins will be measured simultaneously at a given energy, and the shown rates are for the individual bins in ($Q^2$,$\varepsilon$) phase-space. In order to achieve the

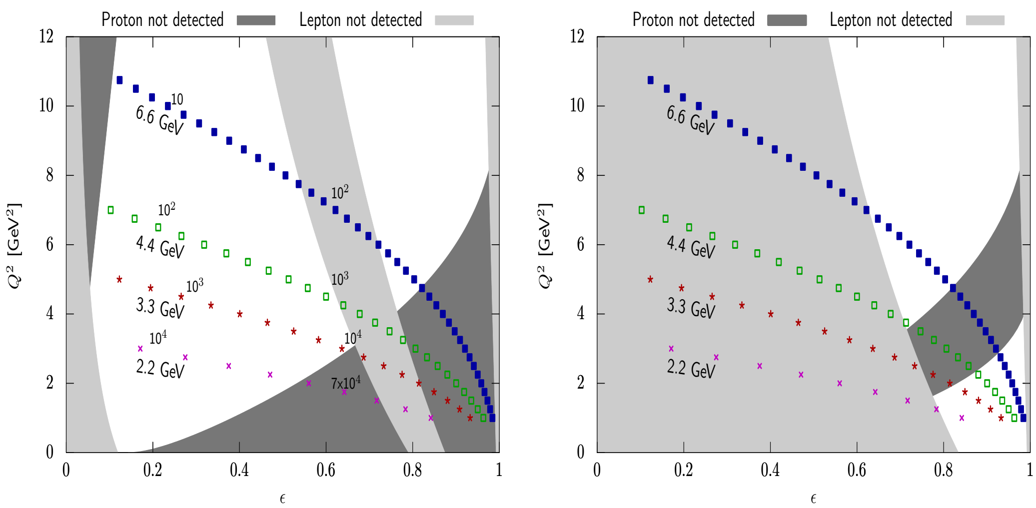


Figure 7. Expected elastic event rates per hour for energies 2.2, 3.3, 4.4, 6.6 GeV in the $\varepsilon$ - $Q^2$ plane. Shaded areas are excluded by the detector acceptance. Left: proposed experiment; Right: standard setup

desired kinematics reach in $Q^2$ and $\varepsilon$ the CLAS12 detection system has to be

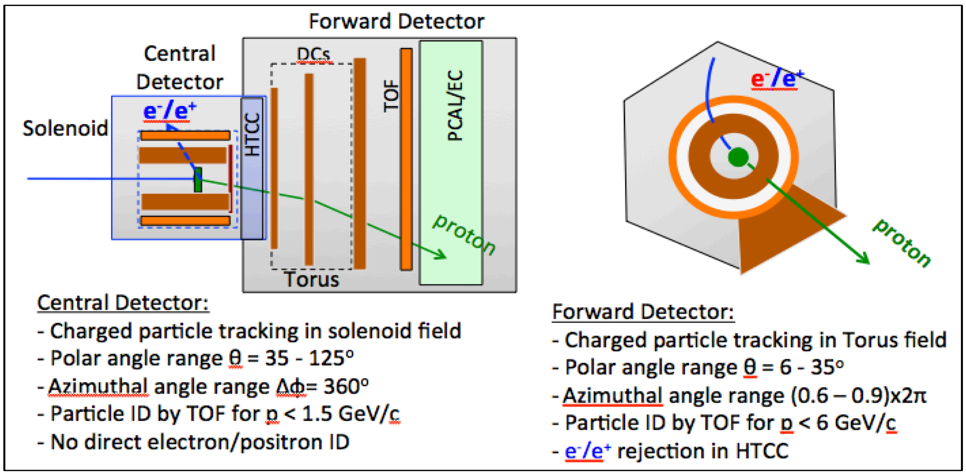


Figure 8. CLAS12 configuration for the elastic $e^-p/e^+p$ scattering experiment (generic). The central detector will detect the electron/positrons, and the bending in the solenoid magnetic field will be identical for the same kinematics. The proton will be detected in the forward detector part. The torus field direction will be the same in both cases. The deflection in $\phi$ due to the solenoid fringe field will be of same in magnitude of $\Delta\phi$ but opposite in direction. The systematic of this shift can be controlled by doing the same experiment with opposite solenoid field directions that would result in the sign change of the $\Delta\phi$.

used with reversed detection capabilities for electrons. The main modification will involve replacing the current Central Neutron Detector with a central electromagnetic calorimeter (CEC). The CEC will need very good resolution, which is provided by the tracking detectors, but will only be used for trigger purposes and for electron/pion separation. The strict kinematic correlation of the scattered electron and the recoil proton should be sufficient to select the elastic events. The CLAS12 configuration suitable for this experiment is shown in Fig. 8.

### *4.4 Projected measurements at CLAS12*

For the rate estimates and the kinematical coverage we have made a number of assumptions that are not overly stringent:

*i)* Positron beam currents (unpolarized), $I_{e^+} \approx 60$ nA;
*ii)* Beam profile, $\sigma_x,\ \sigma_y < 0.4$ mm;
*iii)* Polarization not required, so phase space at the source maybe chosen for optimized yield and beam parameters;
*iv)* Operate experiment with 5 cm liquid $H_2$ target and luminosity of $0.8 \times 10^{35}$ cm$^{-2}$·sec$^{-1}$;
*v)* Use the CLAS12 Central Detector for lepton ($e^+/e^-$) detection at $\Theta_l$=40°-125°;
*vi)* Use CLAS12 Forward Detector for proton detection at $\Theta_p$=7°-35°.

We propose to take data at beam energies of 2.2, 3.3, 4.4 and 6.6 GeV, for

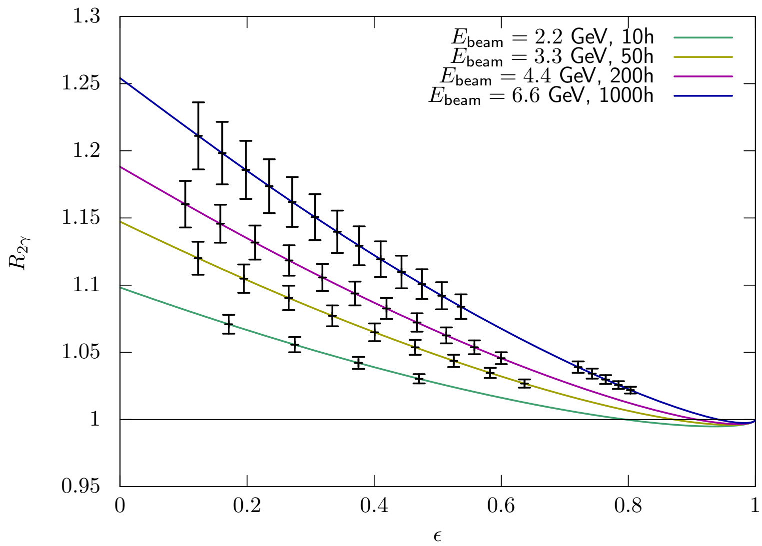


Figure 9. Predicted effect size and estimated errors for the proposed measurement program at CLAS12. We assume bins of constant $\Delta Q^2$=0.25 GeV$^2$.

10 h, 50 h, 200 h and 1000 h respectively, split 1:1 in electron and positron running. The expected statistical errors, together with the expected effect size (phenomenological extraction from [Ber14]) are shown in Fig. 9. The quality of the measured data will quantify hard two-photon-exchange over the whole region of precisely measured and to-be-measured cross section data, enabling a model-free extraction of the form factors from those. It will test if TPE can reconcile the form factor ratio data where the discrepancy is most significantly seen, and test for the first time GPD-based calculations.

*Systematics of the comparison between electron and positron measurements*

The main benefit to measure both lepton species in the same setup closely together in time is the cancellation of many systematics which would affect the result if data of a new positron scattering measurement is compared to existing electron scattering data. For example, one can put tighter limits on the change of detector efficiency and acceptance changes between the two measurements if they are close together in time, or optimally, interleaved.
For the ratio, only relative effects between the species types are relevant; the absolute luminosity, detector efficiency, etc. cancel. Of special concern here is the luminosity. While an absolute luminosity is not needed, a precise determination of the species-relative luminosity is crucial. Precise relative measurement methods, for example based on Møller scattering, exist, but only work when the species is not changed. Switching to Bhabha scattering for the positron case and comparing with Møller scattering is essentially as challenging as an absolute measurement. More suitable is a measurement of the lepton-proton cross section itself at extreme forward angles, i.e., $\varepsilon \approx 1$, where TPE should be negligible and the cross section is the same for both species. To make use of these cancellations, it is paramount that the species switch-over can happen in a reasonable short time frame ($<$ 1 day) to keep the accelerator

and detector setup stable. For the higher beam energies, where the measurement time is longer, it would be ideal if the species could be switched several times during the data taking period. To keep the beam properties as similar as possible, the electron beam should not be generated by the usual high quality source, but employ the same process as the positrons.

### *4.5 Direct $e^+$-p/$e^-$-p comparisons in Hall A and C*

We also examined the possibilities for elastic measurements using the spectrometers in Halls A and C. The main kinematic considerations are the limited momentum reach of the spectrometers in Hall A and the limited angular range for the SHMS in Hall C. The SHMS in Hall C is limited to forward angles, but could be used to detect the protons instead of the leptons, providing measurements at low $\varepsilon$ with the benefit of different systematical uncertainties. BigBite in Hall A is limited in the maximum momentum. However, the large acceptance allows measurements at very low values of $\varepsilon$ with excellent precision.

| $E_{\text{beam}}$ (GeV) | 3.10 | | | 3.55 | | | 4.01 | | |
|---|---|---|---|---|---|---|---|---|---|
| Spectrometer angles (°) | 30 | 70 | 110 | 52.7 | 70 | 110 | 42.55 | 70 | 110 |
| $Q^2$ [(GeV/$c$)$^2$)] | 1.79 | 3.99 | 4.75 | 3.99 | 4.75 | 5.56 | 3.99 | 5.55 | 6.4 |
| $\epsilon$ | 0.82 | 0.32 | 0.1 | 0.49 | 0.30 | 0.09 | 0.60 | 0.28 | 0.08 |
| Time [days/species] | 1 | | | 2 | | | 3 | | |

Table 1. Proposed measurement program for Hall A. Angle values correspond, in order, to the central angles of the two main spectrometers and the central angle of BigBite.

| $E_{\text{beam}}$ (GeV) | 3.1 | | 3.55 | | 4.01 | |
|---|---|---|---|---|---|---|
| Spectrometer angles (°) | 79.7 | 7.64 (120) | 70 | 9.95 (100) | 18 | 16.57 (65) |
| $Q^2$ [(GeV/$c$)$^2$)] | 4.25 | 4.84 | 4.76 | 5.43 | 1.3 | 5.35 |
| $\varepsilon$ | 0.244 | 0.06 | 0.302 | 0.122 | 0.935 | 0.33 |
| Time [days/species] | 3 | | 2 | | 1 | |

Table 2. Proposed measurement program for Hall C. Central angles correspond to the HMS (leptons) and the SHMS (protons) spectrometers positions, with the equivalent lepton angle in parenthesis.

With a beam current of 1 µA for unpolarized positrons on a 10 cm liquid hydrogen target, one could measure at a comparatively high luminosity of $\mathcal{L}$=2.6 pb$^{-1}$·s$^{-1}$. A sketch of a possible measurement program for Hall A and Hall C is listed in Tab. 1 and Tab. 2, respectively. While these measurements could provide precise measurements over a range of $\varepsilon$ values in a short run period, they cover a limited range of beam energies. Because they suffer from the same beam-related systematics, they would benefit from rapid changeover between positrons and electrons, as well as an independent small-angle luminosity monitor to provide checks on the luminosity of the electron and positron beams. Figure 10 show the estimated errors and predicted effect size for Hall A (a) and Hall C (b). A high-impact measurement is possible with a

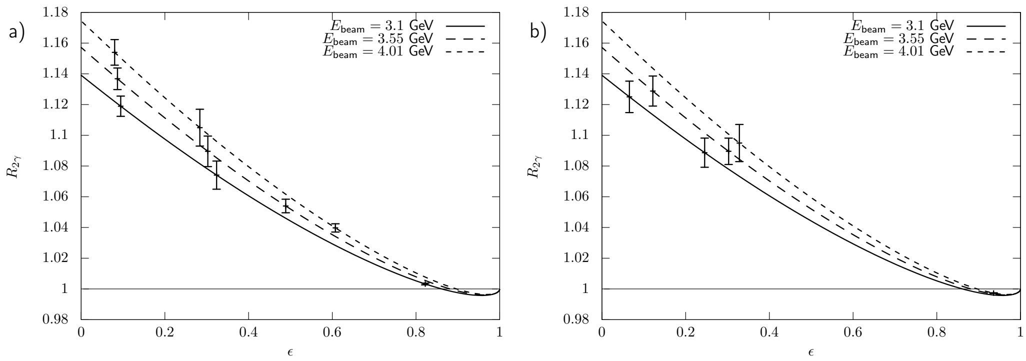


Figure 10. Predicted effect size and estimated errors for the proposed measurement program in Hall A (a) and Hall C (b).

comparatively small amount of beam time. Even in the case the final positron beam current is lower than assumed here, the experiment remains feasible.

### *4.6 "Super-Rosenbluth" measurements with positrons*

Both the modified CLAS12 and Hall A/C projected results shown above are direct extractions of $R_{2\gamma}$. The CLAS12 coincident detection make clean identification of elastic events at large $Q^2$ values possible even with modest kinematic resolution, and the Hall A/C measurements rely on the good resolution of the spectrometers to allow clean identification of elastic scattering from inclusive measurements. The drawback is that a direct comparison of electron and positron scattering is sensitive to differences between the electron and positron beams, as well as any time-dependent efficiency drifts if the time to change between electron and positron beams is long. These issues can be avoided by performing precise Rosenbluth separations with positrons, for direct comparison to form factors extracted using electrons. With sufficient precision, this can provide a very sensitive probe of TPE corrections, free from uncertainties associated with the different conditions of the positron and electron beams.

The so-called "Super-Rosenbluth" technique, involving only the detection of the struck proton, was used by JLab experiments E01-001 and E05-017 to provide a more precise Rosenbluth extraction of the ratio $G_E/G_M$ for comparison to precise polarization measurements [Qat05]. The improved precision comes from the fact that $G_E/G_M$ is independent of systematic effects that yield an overall renormalization of the measurements at a fixed $Q^2$, combined with the fact that many of the experimental conditions are unchanged when detecting $ep$ scattering at fixed $Q^2$ over a range of $\varepsilon$ values. The proton momentum is fixed, and so momentum-dependent corrections drop out in the extraction of $G_E/G_M$. In addition, the cross section dependence on $\varepsilon$ is dramatically reduced when detecting the proton, while the sensitivity to knowledge of the beam energy, spectrometer momentum, and spectrometer angle is also reduced. Finally, the large, $\varepsilon$-dependent radiative corrections also have reduced $\varepsilon$ dependence for proton detection.

These advantages are also beneficial in making precise comparisons of electron

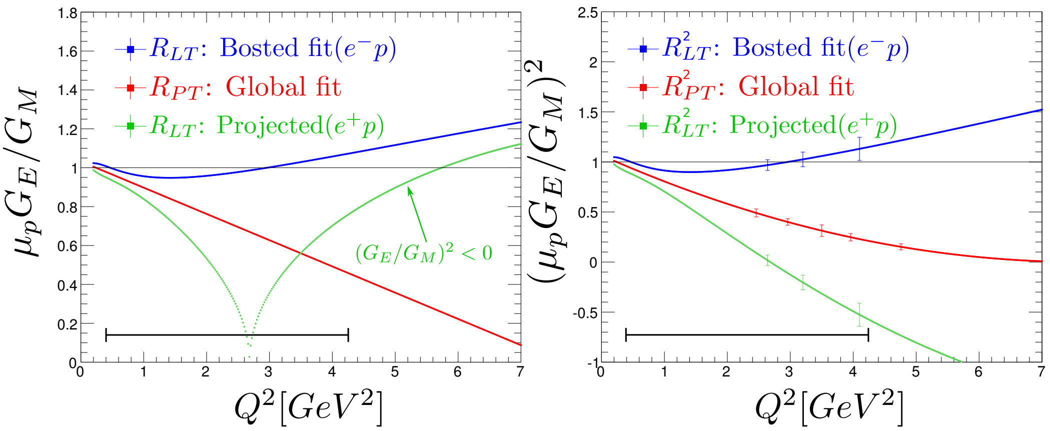


Figure 11. Parameterizations of $R = \mu_p G_E/G_M$ (left) and $R^2$ (right) from LT and polarization data, along with the results expected for positrons assuming that TPE corrections fully explain the LT-Polarization discrepancy. The right figure indicates the $Q^2$ range that could be covered under the assumptions provided in the text, and the point for the electron and positron $R^2_{LT}$ results indicate the uncertainties from the previous Hall A Super-Rosenbluth extraction [Qat05].

and positron scattering. Because most of the systematic uncertainties cancel when looking at the $\varepsilon$ dependence with electrons (or positrons), the measurement does not rely on rapid change of the beam polarity, or on a precise cross normalization or comparison of conditions for electron and positron running. Because extensive data were taken using this technique with electrons during the 6 GeV era, we would propose to use only positrons and extract $G_E/G_M$ which depends only on the *relative* positron cross sections as a function of $\varepsilon$. If rapid changes in the beam polarity are possible, then this approach would allow direct comparison of the cross sections with the advantage that the acceptance is unchanged, while electron detection would require a change of polarity for the Hall A/C measurements, and the overall coincidence acceptance is modified for the CLAS12 measurements. However, for this letter we assume that we would take only positron data for comparison to the existing E01-001 and E05-017 data sets. This approach can give a sensitive comparison of electron- and positron-proton scattering, with minimal systematic uncertainties and no need to cross-normalize electron and proton measurements. It does not provide direct comparisons of the $e^+p/e^-p$ cross section ratio, but does provide a direct and precise comparison of the $\varepsilon$ dependence of the elastic cross section, for which the $G_E$ contribution is identical for positrons and electrons, and the TPE contribution changes sign.

The general measurements would be identical to the E05-017 experiment, with the exception of using a low intensity positron beam rather than the 30-80 $\mu$A electron beam. Assuming a 1 $\mu$A positron beam and the 4 cm $LH_2$ target used in E05-017, an 18 days run could provide measurements with sub-percent statistical uncertainties from 0.4-4.2 GeV$^2$, yielding total uncertainties comparable to the electron beam measurements. This could be extended to >5 GeV$^2$ with the use of a 10 cm target, or if higher beam currents are available. Figure 11 shows projections for positron Super-Rosenbluth measurements under the assumption that the discrepancy between Rosenbluth and polarization extractions is fully explained by TPE contributions. It has been shown [Arr07] that the extraction of the high-$Q^2$ form factors is not limited by our understanding of the TPE contributions, as long as the assumption that the Rosenbluth-Polarization discrepancy is explained entirely by TPE contributions. The propose measurement would test this assumption, and also provide improved sensitivity to the overall size of the linear TPE contribution that appears as a false contribution to $G_E$ when TPE contributions are neglected. The measurement is also sensitive to non-linear contributions [Tva06] coming from TPE, and would provide improved sensitivity compared to existing electron measurements. More details are provided in Ref. [Yur17].

### *4.7 Summary*

Despite recent measurements of the $e^+p/e^-p$ cross section ratio, the proton's form factor discrepancy has not been conclusively resolved, and new measurements at higher momentum transfer are needed. With a positron source at CEBAF, the enormous capabilities of the CLAS12 spectrometer could be brought to bear on this problem and provide a wealth of new data over a widely important kinematic range. Only one major detector configuration change would be necessary to support such a measurement, the installation of the central electromagnetic calorimeter. In designing the JLab positron source, it will be crucial for this and several other experiments to keep to a minimum the time necessary to switch between electron and positron modes, in order to reduce systematic effects.

Another option, utilizing the Super-Rosenbluth technique, would allow for precise LT separations using only positron beams. This is a sensitive test of TPE contributions that does not require the rapid changeover between positrons and electrons, but it does not directly compare positron and electron scattering at fixed kinematics. Instead, it measures the impact of TPE on the Rosenbluth extraction of $\mu_p G_E/G_M$ with high precision.

The data that the proposed experiments could provide will be able to map out the transition between the regions of validity for hadronic and partonic models of hard TPE, and make definitive statements about the nature of the proton form factor discrepancy.

## 5 TPE @ SBS

# A measurement of the transfer of the longitudinal polarization of the beam in elastic positron-proton scattering


### Abstract

Hard two-photon exchange, the only sub-leading radiative effect that is not included in standard radiative corrections prescriptions, may be responsible for the discrepancy between polarized and unpolarized measurements of the proton's form factors. Since calculations of hard TPE are necessarily model-dependent, measurements of observables with direct sensitivity to hard TPE are needed. Much experimental attention has been focused on the unpolarized $e^+p/e^-p$ cross section ratio, but polarization transfer in polarized elastic scattering can also reveal evidence of hard TPE. Furthermore, it has a different sensitivity to the generalized TPE form factors, meaning that measurements provide new information that cannot be gleaned from unpolarized scattering alone. Both $\epsilon$-dependence of polarization transfer at fixed $Q^2$, and deviations between electron- and positron-scattering are key signatures of hard TPE. A polarized positron beam at Jefferson Lab would present a unique opportunity to make the first measurement of positron polarization transfer, and comparison with electron-scattering data would place valuable constraints on hard TPE. In this letter, we propose a measurement program in Hall A that combines the Super BigBite Spectrometer for measuring recoil proton polarization, with a non-magnetic calorimetric detector for triggering on elastically scattered positrons. Though the reduced beam current of the positron beam will restrict the kinematic reach, this measurement will have very small systematic uncertainties, making it a clean probe of TPE.



*Spokesperons: A. Schmidt (schmidta@mit.edu), J. Bernauer, A. Puckett*

The discrepancy between the ratio $\mu_p G_E/G_M$ of the the proton's electromagnetic form factor extracted from polarization asymmetry measurements, and the ratio extracted from unpolarized cross section measurements, leaves the field of form factor physics in an uncomfortable state (see [Afa17] for a recent review). On the one hand, there is a consistent and viable hypothesis that the discrepancy is caused by non-negligible hard two-photon exchange (TPE) [Gui03, Blu03], the one radiative correction omitted from the standard radiative correction prescriptions [Mo69, Max00]. On the other hand, three recent measurements of hard TPE (at VEPP-3, at CLAS, and with OLYMPUS) found that the effect of TPE is small in the region of $Q^2 < 2$ GeV$^2/c^2$ [Rac15, Adi15, Rim17, Hen17]. The TPE hypothesis is still viable; it is possible that hard TPE contributes more substantially at higher momentum transfers, and can fully resolve the form factor discrepancy. But the lack of a definitive conclusion from this recent set of measurements is an indication that alternative approaches are needed to illuminate the situation, and it may be prudent to concentrate experimental effort on constraining and validating model-dependent theoretical calculations of TPE. There are multiple theoretical approaches, with different assumptions and different regimes of validity [Che04, Afa05, Tom15, Blu17, Kur08]. If new experimental data could validate and solidify confidence in one or more theoretical approaches, then hard TPE could be treated in the future like any of the other standard radiative corrections, i.e., a correction that is calculated, applied, and trusted.

VEPP-3, CLAS, and OLYMPUS all looked for hard TPE through measurements of the $e^+p$ to $e^-p$ elastic scattering cross section ratio. After applying radiative corrections, any deviation in this ratio from unity indicates a contribution from hard TPE. However, this is not the only experimental signature one could use. Hard TPE can also appear in a number of polarization asymmetries. Having constraints from many orthogonal directions, i.e., from both cross section ratios and various polarization asymmetries would be valuable for testing and validating theories of hard TPE. As with unpolarized cross sections, seeing an opposite effect for electrons and positrons is a clear signature of TPE.

In this letter, we propose one such polarization measurement, that could both be feasibly accomplished with a positron beam at Jefferson Lab, and contribute new information about two photon exchange that could be used to constrain theoretical models. We propose to measure the polarization transfer (PT) from a polarized proton beam scattering elastically from a proton target, for which no data currently exist. The proposed experiments uses a combination of the future Hall A Super Big-Bite Spectrometer (SBS) to measure the polarization of recoiling protons, along with a calorimetric detector for detecting scattered positrons in coincidence. In the following sections, we review polarization transfer, sketch the proposed measurement, and discuss possible systematic uncertainties.

In the Born approximation (i.e. one-photon exchange), the polarization transferred from a polarized lepton to the recoiling proton is

$$P_t = -hP_e\sqrt{\frac{2\epsilon(1-\epsilon)}{\tau}}\frac{G_E G_M}{G_M^2 + \frac{\epsilon}{\tau}G_E^2}, \tag{19}$$

$$P_l = hP_e\sqrt{1-\epsilon^2}\frac{G_M^2}{G_M^2 + \frac{\epsilon}{\tau}G_E^2}, \tag{20}$$

where $P_t$ is the polarization transverse to the momentum transfer 3-vector (in the reaction plane), $P_l$ is the longitudinal polarization, $P_e$ is the initial lepton polarization, $h$ is the lepton helicity, $\tau$ is the dimensionless 4-momentum transfer squared (Sec: 2.1), $\epsilon$ is the virtual photon polarization parameter (Eq. 3), and $G_E$ and $G_M$ are the proton's electromagnetic form factors. The strength of the polarization transfer technique is to measure $P_t/P_l$, thereby cancelling some systematics associated with polarimetry, and isolating the ratio of the proton's form factors:

$$\frac{P_t}{P_l} = -\sqrt{\frac{2\epsilon}{\tau(1+\epsilon)}}\frac{G_E}{G_M}. \tag{21}$$

This technique has several advantages over the traditional Rosenbluth separation technique for determining form factors. This polarization ratio can be measured at a single kinematic setting, avoiding the systematics associated with comparing data taken from different spectrometer settings. This technique allows the sign of the form factors to be determined, rather than simply their magnitudes. And furthermore, whereas the sensitivity in Rosenbluth separation to $G_E^2$ diminishes at large momentum transfer, polarization transfer retains sensitivity to $G_E$ even when $Q^2$ becomes large. When used in combination at high $Q^2$, Rosenbluth separation can determine $G_M^2$, while polarization transfer can determine $G_E/G_M$, allowing the form factors to be separately determined.

Polarization transfer using electron scattering has been used extensively to map out the proton's form factor ratio over a wide-range of $Q^2$, with experiments conducted at MIT Bates [Mil98], Mainz [Pos01], and Jefferson Lab [Gay01, Mac06, Ron11, Pao10, Zha11], including three experiments, GEp-I [Jon00, Pun05], GEp-II [Gay02], and GEp-III [Puc10] that pushed to high momentum transfer. Another experiment, GEp-2$\gamma$, looked for hints of TPE in the $\epsilon$-dependence in polarization transfer [Mez11, Puc17]. Two other experiments made equivalent measurements by polarizing the proton target instead of measuring recoil polarization [Jon06, Cra07].

While polarization transfer is less sensitive to the effects of hard TPE, it is not immune. Following the formalism of Ref. [Car07], one finds that

$$\frac{P_t}{P_l} = \sqrt{\frac{2\epsilon}{\tau(1+\epsilon)}}\frac{G_E}{G_M} \times \left[1 + \mathrm{Re}\left(\frac{\delta\widetilde{G}_M}{G_M}\right) + \frac{1}{G_E}\mathrm{Re}\left(\delta\widetilde{G}_E + \frac{\nu}{M^2}\widetilde{F}_3\right) - \frac{2}{G_M}\mathrm{Re}\left(\delta\widetilde{G}_M + \frac{\epsilon\nu}{(1+\epsilon)M^2}\widetilde{F}_3\right) + \mathcal{O}(\alpha^4)\right], \quad (22)$$

with $\nu \equiv (p_e + p_{e'})_\mu (p_p + p_{p'})^\mu$, and where $\delta\widetilde{G}_E$, $\delta\widetilde{G}_M$, and $\delta\widetilde{F}_3$ are additional form factors that become non-zero when moving beyond the one-photon exchange approximation. This particular dependence on new form factors is slightly different than one what finds when taking a positron to electron cross section ratio:

$$\frac{\sigma_{e^+p}}{\sigma_{e^-p}} = 1+4G_M\mathrm{Re}\left(\delta\widetilde{G}_M + \frac{\epsilon\nu}{M^2}\widetilde{F}_3\right) - \frac{4\epsilon}{\tau}G_E\mathrm{Re}\left(\delta\widetilde{G}_E + \frac{\nu}{M^2}\widetilde{F}_3\right) + \mathcal{O}(\alpha^4). \quad (23)$$

A measurement of the difference in polarization transfer between electron and positron scattering therefore adds information about TPE in addition to what can be learned from cross section ratios alone.

The GEp-2$\gamma$ experiment looked for the effects of TPE in polarization transfer by making measurements at three kinematic points with varying values of $\epsilon$, but with $Q^2$ fixed at 2.5 GeV$^2/c^2$ [Mez11]. Since in the absence of hard TPE the ratio $G_E/G_M$ has no $\epsilon$-dependence, any variation with $\epsilon$ is a sign of hard TPE. The GEp-2$\gamma$ measurement was statistically consistent with no $\epsilon$-dependence, though their measurement of purely the longitudinal component showed deviations from the one-photon exchange expectation.

A measurement with positron scattering will be useful for constraining TPE effects because deviations from the Born-approximation should have the opposite sign from those in electron scattering. This helps determine if deviations are truly caused by TPE, or if they arise from systematic effects. As the largest systematic uncertainties in polarization transfer are associated with proton polarimetry, a measurement with positrons would have largely the same systematics as an experiment with electrons.

### *5.3 Proposed Measurement*

The proposed experiment copies the basic approach of earlier GEp measurements at JLab. However, since these prior experiments were able to make use of the high-current polarized electron beam, and since the proposed positron source at Jefferson Lab will be limited to currents of approximately 100 nA, several improvements have to be made relative to the GEp program for a positron experiment to be feasible.

The first major improvement will be the Super Big-bite Spectrometer (SBS) [Jag10], which is currently being designed and built for the next generation

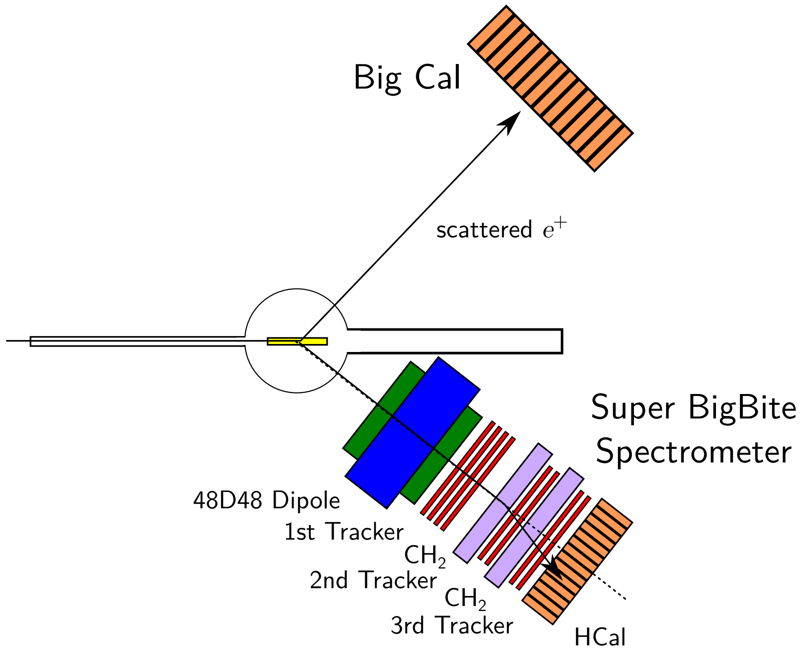


Figure 12. A schematic of the proposed PT measurement.

of form factor measurements in Hall A [Jag10-1]. Whereas previous measurements used the current HRS and HMS spectrometers limited to less than 10 msr of acceptance, SBS is designed with 70 msr of solid-angle acceptance and much larger momentum acceptance. This will allow flexibility in choosing a momentum setting that produces an optimal bend angle for elastically recoiling protons. Furthermore, the proposed single-dipole field configuration for the SBS will greatly simplify the spin-transport properties of the spectrometer, reducing systematics. The larger angular acceptance of the SBS affords another advantage: using a longer target. Where as the GEp-III and GEp-2$\gamma$ experiments used 15 cm and 20 cm liquid hydrogen targets, the SBS can accommodate a 40 cm target at the angles relevant for a positron PT measurement. With the limited positron current, there is much reduced concern with target heating and target boiling. The third advantage is the high beam energy made possible by the 12 GeV upgrade, which will allow measurements to reach the relevant high momentum transfers at angles substantially more forward, where the cross section is comparatively higher.

We propose a measurement set-up along the lines of the GEp-III and GEp-2$\gamma$ experiments, in which elastically scattered positrons are detected in the non-magnetic BigCal detector in coincidence with recoiling protons being detected in the SBS, and their polarization measured by the SBS focal plane polarimeter. A schematic of the experiment is shown in Fig. 12. We have attempted to make reasonable estimates of uncertainty by scaling the achieved statistical uncertainties of the GEp-2$\gamma$ experiment. The statistical uncertainty will largely depend on the product of the magnitude of the asymmetry being measured and the achievable count-rate. That is, we assume:

$$\delta R \propto \left[ P_e P_p A \sqrt{\frac{d\sigma}{d\Omega} \Omega \mathcal{L} T \varepsilon} \right]^{-1}, \tag{24}$$

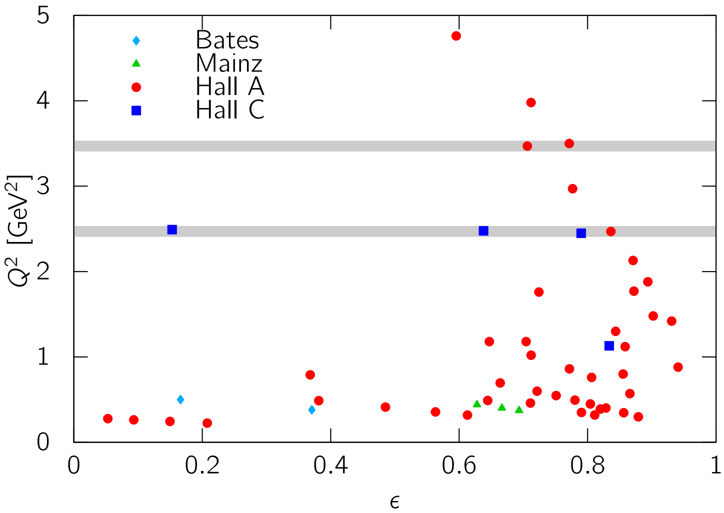


Figure 13. The kinematics of previous polarization transfer measurements with electron beams are shown. A measurement with positrons at either $Q^2 = 2.5$ GeV$^2$ or 3.5 GeV$^2$ would be able to compare with previous electron experiments.

where $P_p$ is the magnitude of the polarization transfered to the recoiling proton, $A$ is the polarimeter analyzing power, $d\sigma/d\Omega$ is the elastic cross section, $\Omega$ is the spectrometer angular acceptance, $\mathcal{L}$ is the luminosity, $T$ is the run-time, and $\varepsilon$ is the running efficiency, i.e. the live-time to wall-time ratio. Applying this assumption to the achieved uncertainties in the GEp-2$\gamma$ experiment, we find that:

$$\delta R_{\text{GEp-2}\gamma} \approx \frac{1.2 \times 10^{-19}[\text{cm sr}^{-1/2}\text{days}^{1/2}]}{P_p\sqrt{\frac{d\sigma}{d\Omega}T}}. \tag{25}$$

Projecting to our proposed positron measurement, we assume equivalent analyzing power, and equivalent running efficiency. The luminosity will be reduced by a factor of 400 (80 $\mu$A current, 20 cm target in GEp-2$\gamma$ to 100 nA current, 40 cm target in our proposed experiment and the beam polarization reduced from $\approx 80\%$ to 60%. However, the spectrometer acceptance will increase from 6.74 msr (Hall C HMS) to 70 msr (SBS). All of these factors combine to yield an uncertainty projection of:

$$\delta R_{\text{proposal}} \approx \frac{9.9 \times 10^{-19}[\text{cm sr}^{-1/2}\text{days}^{1/2}]}{P_p\sqrt{\frac{d\sigma}{d\Omega}T}}. \tag{26}$$

The effects of TPE will have opposite sign in electron scattering experiments relative to positron scattering experiments, and so it would be prudent for the first PT measurement with a positron beam to measure at a $Q^2$ that has already been measured with electrons. The kinematics of previous PT measurements, all with electron beams, are shown in Fig. 13. We highlight $Q^2 = 2.5$ GeV$^2$ and 3.5 GeV$^2$ for our proposed measurement. At these momentum transfers, the proton form factor discrepancy is significant, and both hadronic and partonic calculations of TPE are feasible.

For a competitive first measurement, we believe 2% statistical uncertainty is a reasonable goal. Tables 3 and 4 show the kinematics for these values of momentum transfer as well as the number of measurement days that would be necessary to achieve the 2% statistical uncertainty goal. For example, a 55 day measurement period could cover $Q^2 = 2.5$ GeV$^2$ at 2$^{\text{nd}}$ pass, 3$^{\text{rd}}$ pass and 5$^{\text{th}}$ pass, as well as $Q^2 = 3.5$ GeV$^2$ at 5$^{\text{th}}$ pass, with 48 hours available for pass and configuration changes. The accessible kinematic data points at $Q^2 = 2.5$ GeV$^2$ and 3.5 GeV$^2$ are shown in Fig. 14 along with previous PT data taken with electrons.

| Pass | $E_{e^+}$ | $\epsilon$ | $\theta_{e^+}$ [°] | $p_{e^+}$ | $\theta_p$ [°] | $p_p$ | Days to 2% |
|---|---|---|---|---|---|---|---|
| 2$^{\text{nd}}$ | 4.4 | 0.858 | 24.9 | 3.07 | 38.6 | 2.07 | 12.3 |
| 3$^{\text{rd}}$ | 6.6 | 0.941 | 15.4 | 5.27 | 42.6 | 2.07 | 9.0 |
| 4$^{\text{th}}$ | 8.8 | 0.968 | 11.2 | 7.47 | 44.5 | 2.07 | 7.9 |
| 5$^{\text{th}}$ | 11.0 | 0.980 | 8.8 | 9.67 | 45.6 | 2.07 | 7.3 |

Table 3. Kinematics for measurements at $Q^2 = 2.5$ GeV$^2$, all energies and momenta in units of GeV ($c = 1$).

| Pass | $E_{e^+}$ | $\epsilon$ | $\theta_{e^+}$ [°] | $p_{e^+}$ | $\theta_p$ [°] | $p_p$ | Days to 2% |
|---|---|---|---|---|---|---|---|
| 2$^{\text{nd}}$ | 4.4 | 0.747 | 32.5 | 2.53 | 31.1 | 2.64 | 56.7 |
| 3$^{\text{rd}}$ | 6.6 | 0.897 | 19.3 | 4.73 | 36.3 | 2.64 | 33.8 |
| 4$^{\text{th}}$ | 8.8 | 0.945 | 13.8 | 6.93 | 38.6 | 2.64 | 27.3 |
| 5$^{\text{th}}$ | 11.0 | 0.966 | 10.7 | 9.13 | 40.0 | 2.64 | 24.4 |

Table 4. Kinematics for measurements at $Q^2 = 3.5$ GeV$^2$, all energies and momenta in units of GeV ($c = 1$).

### *5.4 Systematic Uncertainties*

The dominant sources of systematic uncertainty in the GEp campaign are associated with the proton polarimetry, meaning that measurements with electrons and positrons will have systematic offsets in the same direction. Combining electron and positron measurements therefore will not lead to more accurate determination of the proton's Born-level form factors. However, these systematic effects will cancel in determinations of TPE, making polarization transfer an extremely clean technique.

It would therefore be sensible to include, for any positron scattering measurement, a complementary electron scattering measurement. Such an electron measurement could be performed at higher beam currents (so long as target boiling are kept under control) to reduce run times. The SBS magnetic field setting could be kept at the exact same value. If fast-switching between electron and positron modes were possible, the electron and positron running should be inter-leaved further reducing time-dependent systematic effects.

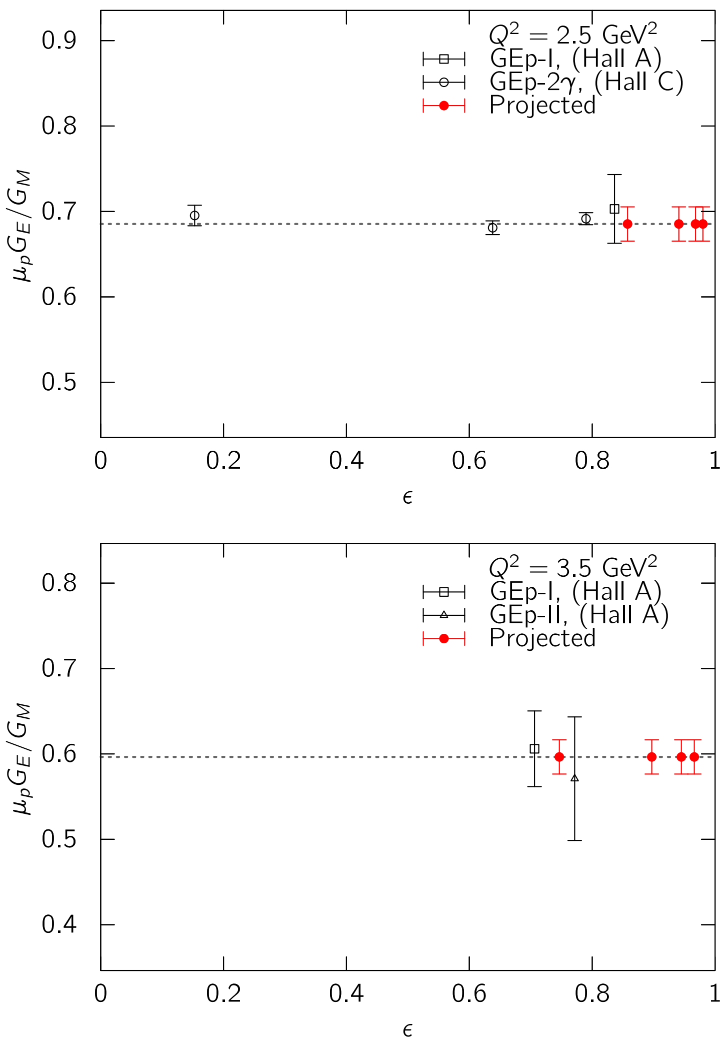


Figure 14. Previous polarization transfer data taken with electrons (black) is shown as a function of $\epsilon$ in comparison to the kinematics of the projected positron measurement (red) with the target 2% statistical uncertainties.

Even without accompanying measurements with electrons, polarization transfer is already a systematically clean technique, and the design of the SBS may lead to further reduction in systematics. One of the leading systematic effects in the GEp-III and GEp-2$\gamma$ experiments was the knowledge of the spectrometer magnetic field, which must be known to fully understand the proton spin precession through the spectrometer. The SBS's single-dipole design will greatly simplify the proton spin-precession. Furthermore, tracking in the HMS polarimeter was complicated due to left-right ambiguities in the design of the drift chambers. The SBS polarimeter, which uses large-area GEM detectors for tracking are being designed to avoid such ambiguities.

Because of the small systematic uncertainties involved, the uncertainties in a polarization-transfer measurement with the proposed positron source at Jefferson Lab will almost certainly be statistically dominated.

### *5.5 Summary*

In this letter, we lay out a feasible approach to measuring polarization transfer in elastic positron-proton scattering with the proposed positron source at Jefferson Lab. Such a measurement would add valuable information that could constrain calculations of two-photon exchange and would be complementary to that from measurements of the unpolarized $e^+p/e^-p$ cross section ratio. Our proposed experiment would take advantage of the upcoming Super BigBite Spectrometer to overcome the limitations in luminosity that would be inevitable with a positron beam.

Several important steps must still be taken, most crucially, the successful completion and commissioning of the SBS spectrometer. The estimates laid out in this letter are based on scaling the uncertainties from previous measurements. Sophisticated simulations of a fully-realized detector will make this estimates much more concrete and trustworthy. Lastly, the proposed measurement focuses on the high-$\epsilon$ region, accessible in realistic experiment time-frames. The current best theoretical calculations of hard TPE are needed for PT at these kinematics to understand how much value such an experiment will add.

## 6 p-DVCS @ CLAS12

# A polarized positron beam for DVCS on the proton with CLAS12 at Jefferson Lab

**Abstract**

The measurement of Deeply Virtual Compton Scattering on the proton with a polarized positron beam in CLAS12 can give access to a complete set of observables for the extraction of Generalized Parton Distributions with the upgraded 11 GeV CEBAF. This provides a clean separation of the real and imaginary parts of the amplitudes, greatly simplifies the analysis, and provides a crucial handle on the model dependences and associated systematic uncertainties. The real part of the amplitude is in particular sensitive to the $D$-term which parameterizes the Gravitational Form Factors of the nucleon. Azimuthal dependences and $t$-dependences of the azimuthal moments for Beam Charge Asymmetries on unpolarized Hydrogen are estimated using a 1000 hours run with a luminosity of $2 \times 10^{34}$ cm$^{-2}\cdot$s$^{-1}$ and 80% beam polarization.

*Spokespersons: V. Burkert (burkert@jlab.org), L. Elouadrhiri, F.-X. Girod*

### *6.1 Introduction*

The challenge of understanding nucleon electromagnetic structure still continues after six decades of experimental scrutiny. From the initial measurements of elastic form factors to the accurate determination of parton distributions through deep inelastic scattering, the experiments have increased in statistical and systematic precision. During the past two decades it was realized that the parton distribution functions represent special cases of a more general, much more powerful, way to characterize the structure of the nucleon, the generalized parton distributions (GPDs) (see [Mul94] for the original work and [Die03, Bel05] for reviews). The GPDs are the Wigner quantum phase space distribution of quarks in the nucleon describing the simultaneous distribution of particles with respect to both position and momentum in a quantum-mechanical system. In addition to the information about the spatial density and momentum density, these functions reveal the correlation of the spatial and momentum distributions, *i.e.* how the spatial shape of the nucleon changes when probing quarks of different momentum fraction of he nucleon.

The concept of GPDs has led to completely new methods of "spatial imaging" of the nucleon in the form of (2+1)-dimensional tomographic images, with 2 spatial dimensions and 1 dimension in momentum [Bur02, Ji03, Bel04]. The second moments of GPDs are related to form factors that allow us to quantify how the orbital motion of quarks in the nucleon contributes to the nucleon spin, and how the quark masses and the forces on quarks are distributed in transverse space, a question of crucial importance for our understanding of the dynamics underlying nucleon structure and the forces leading to color confinement.

The four leading twist GPDs $H$, $\widetilde{H}$, $E$, and $\widetilde{E}$, depend on the 3 variable $x$, $\xi$, and $t$, where $x$ is the longitudinal momentum fraction of the struck quark, $\xi$ is the longitudinal momentum transfer to the quark ($\xi \approx x_B/(2 - x_B)$), and $t$ is the invariant 4-momentum transfer to the proton. The mapping of the nucleon GPDs, and a detailed understanding of the spatial quark and gluon structure of the nucleon, have been widely recognized as key objectives of nuclear physics of the next decades. This requires a comprehensive program, combining results of measurements of a variety of processes in $eN$ scattering with structural information obtained from theoretical studies, as well as with expected results from future lattice QCD simulations. The `CLAS12` detector (Fig. 15) has recently been completed and has begun the experimental science program in the 12 GeV era Jefferson Lab.

### *6.2 Accessing GPDs in DVCS*

The most direct way of accessing GPDs at lower energies is through the measurement of DVCS in a kinematical domain where the so-called handbag diagram (Fig. 16) makes the dominant contributions. However, in DVCS as in other deeply virtual reactions, the GPDs do not appear directly in the cross section, but in convolution integrals called Compton Form Factors (CFFs),

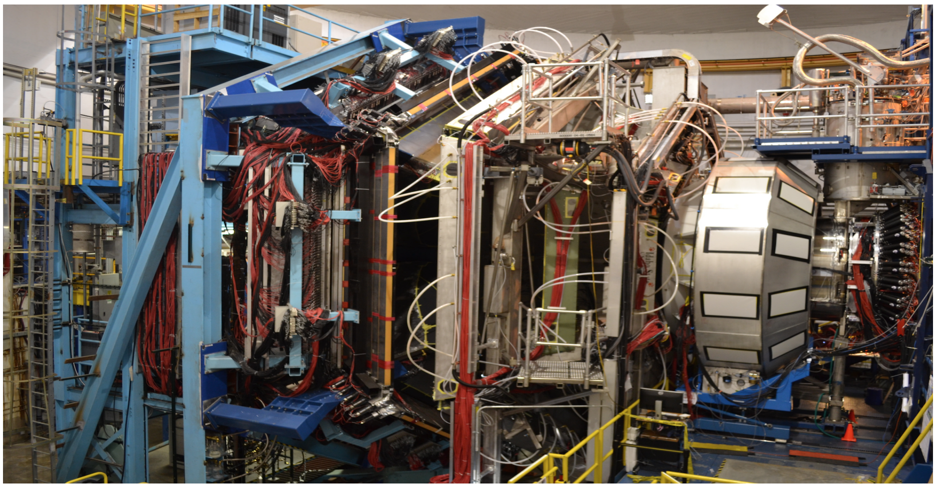

Figure 15. The CLAS12 detector in Hall B. The beam line is running from the right to the left. The liquid hydrogen target is centered in the solenoid magnet with 5 T central magnetic field, and is surrounded by tracking and particle identification detectors covering the polar angle range from $40°$ to $125°$. The forward detector consists of the $2\pi$ gas Čerenkov counter (large silvery box to the right), the tracking chambers around the superconducting torus magnet, 2 layers of time-of-flight systems and two layers of electromagnetic calorimeters for electron triggering and photon detection to the far left.

which are complex quantities defined as, e.g. for the GPD $H^q$:

$$\mathcal{H}^{\rm II}(\xi,t) \equiv \int_{-1}^{+1} \frac{H^q(x,\xi,t)dx}{x-\xi+i\epsilon} = \int_{-1}^{+1} \frac{H^q(x,\xi,t)dx}{x-\xi} + i\pi H^q(\xi,\xi,t) \ , \tag{27}$$

where the first term on the r.h.s. corresponds to the real part and the second term to the imaginary part of the scattering amplitude. The superscript $q$ indicates that GPDs depend on the quark flavor. From the above expression it is obvious that GPDs, in general, can not be accessed directly in measurements. However, in some kinematical regions the BH process where high energy photons are emitted from the incoming and scattered electrons, can be important. Since the BH amplitude is purely real, the interference with the DVCS amplitude isolates the imaginary part of the DVCS amplitude. The interference of the two processes offers the unique possibility to determine GPDs directly at the singular kinematics $x = \xi$. At other kinematical regions a deconvolution of the cross section is required to determine the kinematic dependencies of the GPDs. It is therefore important to obtain all possible independent information that will aid in extracting information on GPDs. The interference terms for polarized beam $I_{LU}$, longitudinally polarized target $I_{UL}$, transversely (in scattering plane) polarized target $I_{UT}$, and perpendicularly (to scattering plane) polarized target $I_{UP}$ are given by the expressions:

$$I_{LU} \sim \sqrt{\tau'}[F_1 H + \xi(F_1+F_2)\widetilde{H} + \tau F_2 E] \tag{28}$$
$$I_{UL} \sim \sqrt{\tau'}[F_1 \widetilde{H} + \xi(F_1+F_2)H + (\tau F_2 - \xi F_1)\xi\widetilde{E}] \tag{29}$$
$$I_{UP} \sim \tau[F_2 H - F_1 E + \xi(F_1+F_2)\xi\widetilde{E} \tag{30}$$
$$I_{UT} \sim \tau[F_2 \widetilde{H} + \xi(F_1+F_2)E - (F_1+\xi F_2)\xi\widetilde{E}] \tag{31}$$
$$\tag{32}$$

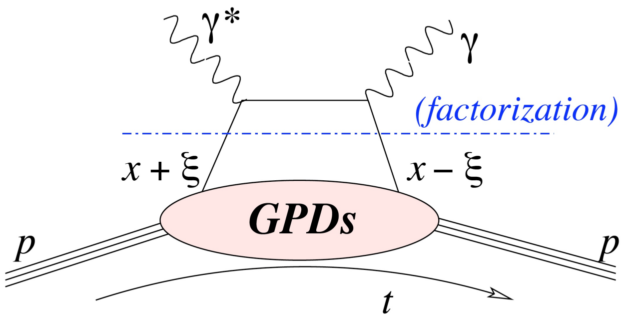


Figure 16. Leading order contributions to the production of high energy single photons from protons. The DVCS handbag diagram contains the information on the unknown GPDs.

where $\tau = -t/4M^2$ and $\tau' = (t_0 - t)/4M^2$. By measuring all 4 combinations of interference terms one can separate all 4 leading twist GPDs at the specific kinematics $x = \xi$. Experiments at JLab using 4 to 6 GeV electron beams have been carried out with polarized beams [Ste01, Mun06, Gir07, Gav09, Jo15] and with longitudinal target [Che06, Sed14, Pis15], showing the feasibility of such measurements at relatively low beam energies, and their sensitivity to the GPDs. Techniques of how to extract GPDs from existing DVCS data and what has been learned about GPDs can be found in [Kum12, Gui13].

The structure of the differential cross section for polarized beam with unpolarized target, and polarized beam with polarized target is reported in Eq. 8 and Eq. 13. In these expressions, $\sigma_i$ and $\Delta\widetilde{\sigma}_i$ are even in the azimuthal angle $\phi$ and beam-polarization independent, while $\widetilde{\sigma}_i$ and $\Delta\sigma_i$ are odd in $\phi$ and beam-polarization dependent. The interference terms

$$\sigma_{INT} \sim \mathcal{R}\mathrm{e}\left[A(\gamma^* N \to \gamma N)\right] \tag{33}$$

$$\widetilde{\sigma}_{INT} \sim \mathcal{I}\mathrm{m}\left[A(\gamma^* N \to \gamma N)\right] \tag{34}$$

$$\Delta\sigma_{INT} \sim \mathcal{R}\mathrm{e}\left[A(\gamma^* \vec{N} \to \gamma N)\right] \tag{35}$$

$$\Delta\widetilde{\sigma}_{INT} \sim \mathcal{I}\mathrm{m}\left[A(\gamma^* \vec{N} \to \gamma N)\right] \tag{36}$$

are the real and imaginary parts of the Compton amplitude. The unpolarized and polarized beam $e^+ - e^-$ charge difference for unpolarized and polarized targets determines uniquely the interference contributions (Eq. 11-12-16-17). If only a polarized electron beam is available, the beam helicity asymmetry and average determine a combination of the inteference and pure DVCS amplitudes (Eq. 9-10-14-15). One can separate these contributions using the Rosenbluth technique [Ros50]. This requires measurements at two significantly different beam energies, which reduces the kinematical coverage that can be achieved with this method. The combination of polarized electron and polarized positron beams does not suffer this limitation, and it offers a separation over the full kinematic range available at the maximum beam energy.

*The CLAS12 Detector*

The experimental program will use the CLAS12 detector (Fig. 15) for the detection of the hadronic final states. CLAS12 consists of a Forward Detector (FD) and a Central Detector (CD). The Forward Detector is comprised of six symmetrically arranged sectors defined by the six coils of the superconducting torus magnet. Charged particle tracking is provided by a set of 18 drift chambers with a total of 36 layers in each sector. Additional tracking at 5°-35° is achieved by a set of 6 layers of micromesh gas detectors (micromegas) immediately downstream of the target area and in front of the High Threshold Čerenkov Counter (HTCC). Particle identification is provided by time-of-flight information from two layers of scintillation counter detectors (FTOF). Electron, photon, and neutron detection are provided by the triple layer electromagnetic calorimeter, PCAL, EC(inner), and EC(outer). The heavy-gas Čerenkov Counter (LTCC) provides separation of high momentum pions from kaons and protons. The Central Detector consists of 6 to 8 layers (depending on the configuration) of silicon strip detectors with stereo readout and 6 layers of micromegas arranged as a barrel around the target, a barrel of scintillation counters to measure the particle flight time from the target (CTOF), and a scintillation-counter based Central Neutron Detector (CND).

*Beam charge asymmetries on protons*

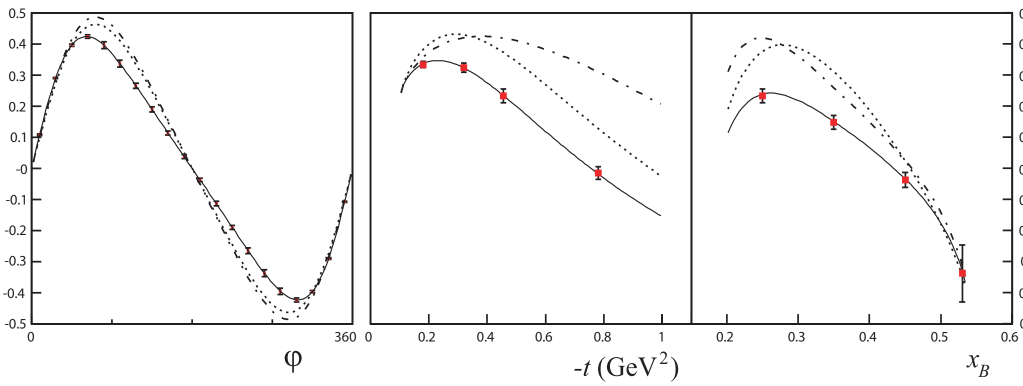


Figure 17. The beam spin asymmetry showing the DVCS-BH interference for 11 GeV beam energy [Sab11]: (left panel) $x = 0.2$, $Q^2 = 3.3$ GeV$^2$, $-t = 0.45$ GeV$^2$; (middle and right panels) $\phi = 90°$, other parameters same as in left panel. Many other bins will be measured simultaneously. The curves represent various parameterizations within the VGG model [Van99]. Projected uncertainties are statistical.

Beam spin asymmetries of polarized electrons for the DVCS process have been measured at lower energies and are known to be large, up to 0.3-0.4. Figure 17 shows projections of the Beam Spin Asymmetry (BSA) for some specific kinematics at an electron beam energy of 11 GeV. The uncertainties are estimated assuming an experiment of 1000 hours at an instantaneous luminosity of $\mathcal{L} = 10^{35}\text{cm}^{-2}\cdot\text{s}^{-1}$. The asymmetry is the results of the interference term $\tilde{\sigma}_{INT}$ in Eq. 8). Note that the magnitude of the interference amplitude is

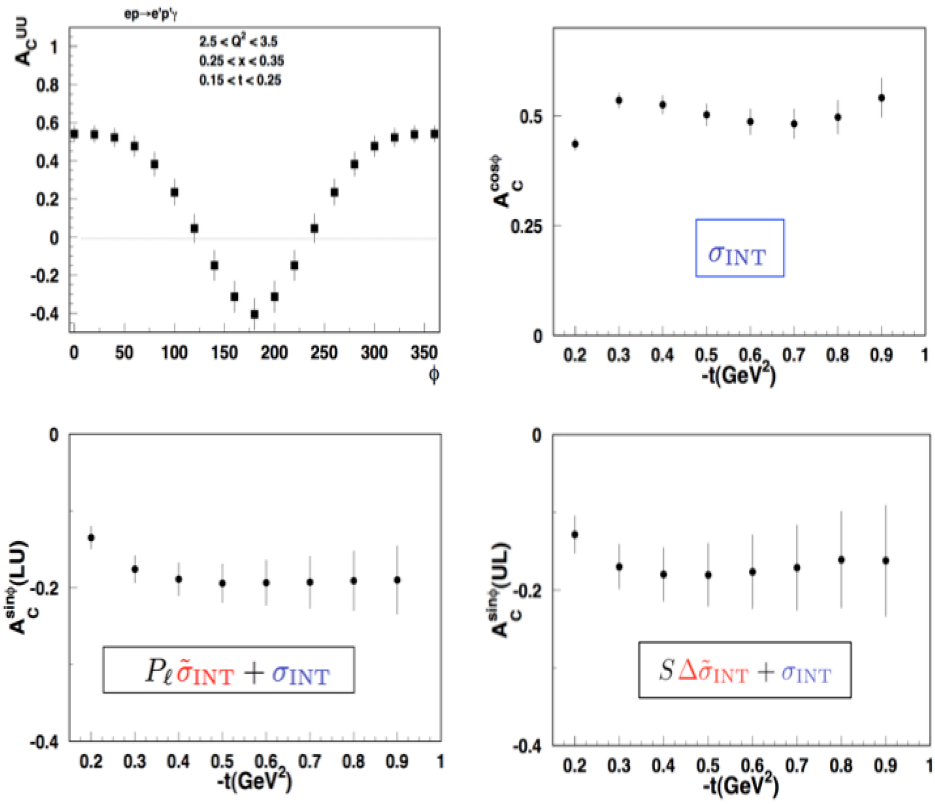


Figure 18. Electron-positron DVCS charge asymmetries: (top-left) azimuthal dependence of the charge asymmetry for positron and electron beam at 11 GeV beam; (top-right) moment in $\cos(\phi)$ of the charge asymmetry versus momentum transfer $t$ to the proton; (bottom-left) charge asymmetries for polarized electron and positron beams at fixed polarization (LU); (bottom right) charge asymmetry for longitudinally polarized protons at fixed polarization (UL). The error bars are estimated for a 1000 hours run with positron beam and luminosity $\mathcal{L} = 2 \times 10^{34}$ cm$^{-2}$·sec$^{-1}$ at a beam polarization $P = 0.6$, and a 1000 hours electron beam run with luminosity $\mathcal{L} = 10 \times 10^{34}$ cm$^{-2}$·sec$^{-1}$ and beam polarization $P = 0.8$. The error bars are statistical for a single bin in $Q^2$, $x$, and $t$ as shown in the top-left panel. Other bins are measured simultaneously.

independent of the electric charge, but the BSA sign is opposite for electrons and positrons.

Eq. 11 also shows that the term $\sigma_{INT}$ can be isolated in the difference of unpolarized electron and positron cross sections. Examples of the charge difference and the charge asymmetry are shown in Fig. 18. The unpolarized charge asymmetry $A_c^{UU}$ and its $\cos\phi$ moment $A^{\cos\phi}$ can both be large for the dual model assumed in our estimate. For quantitative estimates of the charge differences in the cross sections we use the acceptance and luminosity achievable with `CLAS12` as basis for measuring the process $ep \to ep\gamma$ at different beam and target conditions. A 5 cm long liquid hydrogen is assumed with an electron current of 75 nA, corresponding to an operating luminosity of $10^{35}$cm$^{-2}$·sec$^{-1}$. For the positron beam a 5 times lower beam current of 15 nA is assumed. In either case 1000 hours of beam time is used for the rate projections. For quantitative estimates of the cross sections the dual model [Guz06, Guz09] is used.

It incorporates parameterizations of the GPDs $H$ and $E$. As shown in Fig. 18, effects coming from the charge asymmetry can be large. In case of unpolarized beam and unpolarized target the cross section for electron scattering has only a small dependence on azimuthal angle $\phi$, while the corresponding positron cross section has a large $\phi$ modulation. The difference is directly related to the term $\sigma_{INT}$ in Eq. 11.

### *6.4 The science case for DVCS with polarized positrons*

The science program for DVCS with electrons beams has been well established, and several approved experiments for 12 GeV operation have already been carried out or are currently in the process and planned for the next few years. What do polarized positron beams add which makes a most compelling case for experiments with CLAS12? In this section we discuss one example of the impact of DVCS measurements with polarized positron beams, and corresponding to the unraveling of the force distribution on quarks in the proton. Here We refer to the recent publication in the journal Nature of the results of an analysis on the pressure distribution in the proton [Bur18].

This analysis is based on the results of BSA and unpolarized DVCS cross section DVCS measured with CLAS in Hall B. The determination of the pressure distribution proceeds in several steps:

- *i)* We begin with the sum rules that relate the second Mellin moments of the GPDs to the Gravitational Form Factors (GFFs) [Ji97];
- *ii)* We then define the complex CFF $\mathcal{H}$ directly related to the experimental observables describing the DVCS process, i.e., the BSA and the differential cross section;
- *iii)* The real and imaginary parts of $\mathcal{H}$ can be related through a dispersion relation [Die07, Ani08, Pas14] at fixed $t$, where the $D(t)$-term appears as a subtraction constant [Pol99];
- *iv)* We recover $d_1(t)$ from the expansion of the $D(t)$-term in the Gegenbauer polynomials of $\xi$, the momentum transfer to the struck quark;
- *v)* We finally proceed with the fits to the data and extract $D(t)$ and determine $d_1(t)$;
- *vi)* The pressure distribution is then determined from the relation of $d_1(t)$ and $p(r)$ through a Bessel integral.

The sum rules that relate the second Mellin moments of the chiral-even GPDs to the GFFs are [Ji97]:

$$\int \mathrm{d}x\, x\, [H(x,\xi,t) + E(x,\xi,t)] = 2J(t) \tag{37}$$

$$\int \mathrm{d}x\, xH(x,\xi,t) = M_2(t) + \frac{4}{5}\xi^2 d_1(t)\,, \tag{38}$$

where $M_2(t)$ and $J(t)$ respectively correspond to the time-time and time-space components of the Energy Momentum Tensor (EMT), and give access to the mass and total angular momentum distributions carried by the quarks in the proton. The quantity $d_1(t)$ corresponds to the space-space components of the EMT, and encodes the shear forces and pressure acting on the quarks. We have some constraints on $M_2(t)$ and $J(t)$, notably at $t = 0$ they are fixed to the proton's mass and spin. By contrast, almost nothing is known on the equally fundamental quantity $d_1(t)$. For instance, considering the physics content of $d_1(t)$, we can expect the existence of a zero sum rule ensuring the total pressure and forces to vanish, thus preserving the stability of the dynamics of the proton. The observables are parameterized by the CFFs, which for the GPD $H$ are the real quantities $\mathcal{R}\mathrm{e}\,[\mathcal{H}]$ and $\mathcal{I}\mathrm{m}\,[\mathcal{H}]$ defined by:

$$\begin{aligned} &\mathcal{R}\mathrm{e}\,[\mathcal{H}(\xi,t)] + i\,\mathcal{I}\mathrm{m}\,[\mathcal{H}(\xi,t)] \\ &\qquad = \int_{-1}^{1} dx \left[\frac{1}{\xi - x - i\epsilon} - \frac{1}{\xi + x - i\epsilon}\right] H(x,\xi,t)\,. \end{aligned} \tag{39}$$

The average quark momentum fraction $x$ is not observable in the process; it is integrated over with the quark propagators. Analytical properties of the amplitude in the Leading Order (LO) approximation lead to the dispersion relation:

$$\mathcal{R}\mathrm{e}\,[\mathcal{H}(\xi,t)] \stackrel{\mathrm{LO}}{=} D(t) + \frac{1}{\pi}\mathcal{P}\int_{0}^{1} dx \left(\frac{1}{\xi - x} - \frac{1}{\xi + x}\right) \mathrm{Im}\mathcal{H}(x,t) \tag{40}$$

where the subtraction constant is the so-called $D$-term. The dispersion relation allows us trading-off the two CFFs as unknowns with one CFF and the $D$-term [Rad13, Rad13-1]. For our purpose we recover the $d_1(t)$ as the first coefficient in the Gegenbauer expansion of the $D$-term. Here, we truncate this expansion to $d_1(t)$ only:

$$D(t) = \frac{1}{2}\int_{-1}^{1} \mathrm{dz}\,\frac{D(z,t)}{1-\mathrm{z}} \tag{41}$$

with

$$D(z,t) = (1 - z^2)\left[d_1(t) C_1^{3/2}(z) + \cdots\right] \tag{42}$$

and

$$-1 < z = \frac{x}{\xi} < 1\,. \tag{43}$$

Our starting points in the analysis are the global fits presented in [Kum10, Mul13], referred to as KM parameterization. The imaginary part of the amplitude is calculated from a parameterization of the GPDs along the diagonal $x = \xi$. The real part of the amplitude is then reconstructed assuming LO dominance and applying the dispersion relation. The $\xi$-dependence of the $D$-term is completely generated by the Gegenbauer expansion, restricted to the $d_1(t)$ term only. Finally, the momentum transfer dependence of the $d_1(t)$ term is given as a functional form, with three parameters $d_1(0)$, $M$, and $\alpha$:

$$d_1(t) = d_1(0)\left(1 - \frac{t}{M^2}\right)^{-\alpha} \tag{44}$$

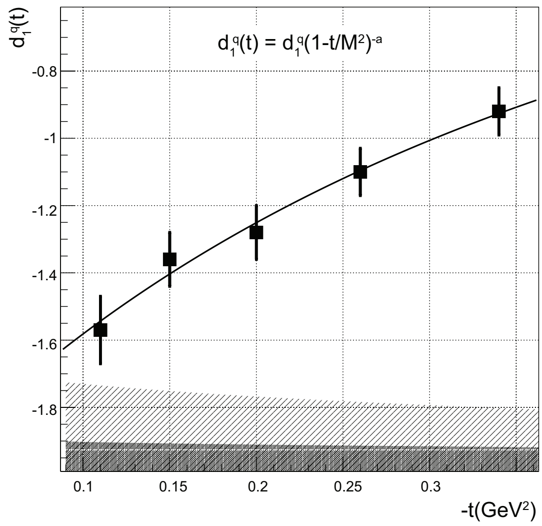


Figure 19. Example of a fit to $d_1(t)$. The error bars are from the fit to the cross sections at fixed value of $-t$. The single-shaded area at the bottom corresponds to the uncertainties from the extension of the fit into regions without data and is reflected in the green shaded are in Fig. 20. The double-shaded area corresponds with the projected uncertainties from future experiment [Elo16], as shown in Fig. 20 with the red shaded area. Uncertainties represent 1 standard gaussian deviation.

where the chosen form of $d_1(t)$ with $\alpha$=3 is consistent with the asymptotic behavior required by the dimensional counting rules in QCD [Lep80]. We adjust and fix the central values of the model parameters to the data at 6 GeV [Gir07, Jo15]. They include unpolarized and polarized beam cross-sections over a wide phase-space in the valence region, and support the model indicating that the GPD $H$ largely dominates these observables. An illustration of a fit to the $d_1(t)$ dependence is provided in Fig. 46. The data points correspond to the values extracted from the fit to the unpolarized cross section data. The experimental analysis shows that $d_1(0)$ has a negative sign. This is consistent with several theoretical studies [Goe07, Kim12, Pas14]. The fit results in a $d_1(0)$ value of

$$d_1(0) = -2.04 \pm 0.14(\text{stat.}) \pm 0.33(\text{syst.})\,. \tag{45}$$

The negative sign of $d_1(0)$ found in this analysis seems deeply rooted in the spontaneous breakdown of chiral symmetry [Kiv01], which is a consequence of the transition of the microsecond old universe from its state of de-confined quarks and gluons to the state of confined quarks in stable protons. It is thus intimately connected to the stability of the proton [Goe07] and of the visible universe. We finally can relate the GFF $d_1(t)$ to the pressure distribution *via* the spherical Bessel integral:

$$d_1(t) \propto \int \mathrm{d}^3\mathbf{r}\, \frac{\mathrm{j_0(r\sqrt{-t})}}{2t}\, \mathrm{p(r)}\,. \tag{46}$$

Our results on the quark pressure distribution in the proton are illustrated in Fig. 20. The black central line corresponds to pressure distribution $r^2p(r)$ extracted from the $D$-term parameters fitted to the published 6 GeV data [Jo15].

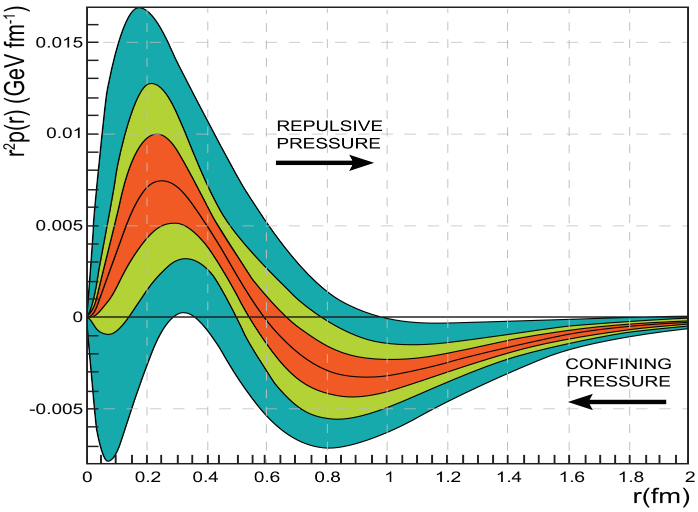


Figure 20. The radial pressure distribution in the proton. The graph shows the pressure distribution $r^2p(r)$ resulting from the interactions of the quarks in the proton versus the radial distance from the center in femtometer. The black central line corresponds to the pressure extracted from the $D$-term parameters fitted to the published data at 6 GeV [Jo15]. The corresponding estimated uncertainties are displayed as the shaded area shown in light green. Uncertainties represent 1 standard deviation.

The corresponding estimated uncertainties are displayed as the shaded area shown in light green. There is a positive core and a negative tail of the $r^2p(r)$ distribution as a function of the radial distance from the proton's center with a zero-crossing near 0.6 fm from that center. We also note that the regions where repulsive and binding pressures dominate are separated in radial space, with the repulsive distribution peaking near $r$=0.25 fm, and the maximum of the negative pressure responsible for the binding occurring near $r$=0.8 fm. The outer shaded area shown in dark green in Fig. 20 corresponds with the $D$-term uncertainties obtained in the global fit results from previous research [Kum10, Mul13]. They exhibit a shape similar to the light green area and confirm the robustness of the analysis procedure to extract the $D$-term. Here we remark that the pressure $p(r)$ must satisfy the stability condition

$$\int_0^\infty r^2 p(r) dr = 0 \,, \tag{47}$$

which is realized within the uncertainties of our analysis. The shape of the radial pressure distribution mimics closely the results obtained within the chiral quark soliton model [Goe07]. In this model, the proton is modeled as a chiral soliton in which constituent quarks are bound by a self-consistent pion field. The comparison with our results suggests that the pion field is significantly relevant for the description of the proton as a bound state of quarks.

*What positrons will add to this program?*

There are a couple of limiting factors in the analyses presented above. These are related to the limited experimental information that can be obtained from having just polarized electron beam available:

*i)* The use of the dispersion relation in Eq. 40 to determine $\mathcal{R}\mathrm{e}\,[\mathcal{H}(\xi,t)]$;
*ii)* The need to extrapolate the $t$-dependence of the formula in Eq. 46.

While the extrapolation is unavoidable when extracting the pressure distribution over the entire radial distance, applying the dispersion relation in Eq. 40 at large -$t$ values, where issues with convergence may occur, is problematic. It is therefore highly desirable to determine the subtraction term $D(t)$ directly from the DVCS data without the need for applying the dispersion relation. Such a procedure requires to determine both the real and imaginary parts of the CFF $\mathcal{H}(\xi,t)$ in Eq. (40) directly from experiment. The term $D(t)$ can then be directly extracted. By isolating the terms $\sigma_{INT}$ and $\widetilde{\sigma}_{INT}$, the real and imaginary parts of the Compton amplitude can be separated. This is achieved by measuring the difference in the unpolarized cross sections and the helicity-dependent cross sections for (polarized) electrons and (polarized) positrons. From Fig. 18, we can infer that both of these observables can result in large cross section differences and polarization asymmetries, and can be well measured already with modest positron currents, by making use of the large acceptance capabilities of CLAS12.

While our focus for this letter is the determination of the pressure distribution and the shear forces in the proton, using a transversely spin polarized target and polarized electron and positron beams, the term $\Delta\sigma_{INT}$ in Eq. 13 can be isolated. It is related to the GPD $E$ thorugh the CFF $\mathcal{E}(\xi,t)$, and thus to the angular momentum distribution in the proton. Measurement of $\mathcal{E}(\xi,t)$ will allow for the extraction of the radial dependence of the angular momentum density in protons and can be determined in a fashion similar to the one described for the pressure distribution.

### *6.5 Experimental setup for DVCS experiments*

Figure 21 shows generically how the electron-proton and the positron-proton DVCS experiments would be configured. Electrons and positrons will be detected in the forward detection system of CLAS12. However, for the positron run the torus magnet would have the reversed polarity so that positron trajectories would look identical to the electron trajectories in the electron-proton experiment, and limit systematic effects in acceptances. The recoil proton in both cases would be detected in the Central Detector at the same solenoid magnet polarity, also eliminating most systematic effects in the acceptances. However, there is a remaining systematic difference in the two configuration, as the forward scattered electron/positron would experience different transverse field components in the solenoid, which will cause the opposite azimuthal motion in $\phi$ in the forward detector. A good understanding of the acceptances in both cases is therefore important. The high-energy photon is, of course, not affected by the magnetic field configuration.

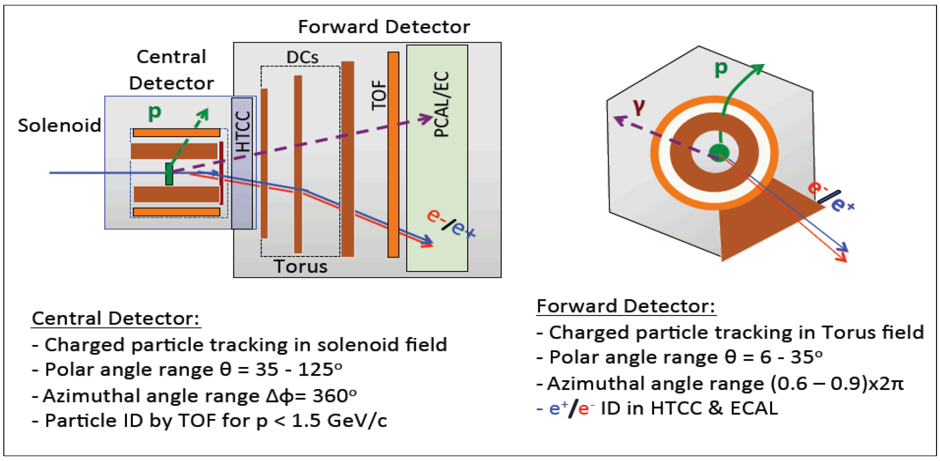


Figure 21. Generic CLAS12 configuration for the electron-proton and the positron-proton experiments. The central detector will detect the protons, and the bending in the magnetic solenoid field will be identical for the same kinematics. The electron and the positron, as well as the high-energy DVCS photon will be detected in the forward detector part. The electron and positron will be deflected in the torus magnetic field in the same way as the torus field direction will be opposite in the two experiments. The deflection in $\phi$ due to the solenoid fringe field will be of same magnitude $\Delta\phi$ but opposite in direction. The systematic of this shift can be controlled by doing the same experiment with opposite solenoid field directions that would result in the sign change of the $\Delta\phi$.

### *6.6 Summary*

In this letter, we described the use of a new polarized positron beam in conjunction with the already available polarized electron beam to significantly enhance the program to study the generalized parton distribution and to extract physical quantities that are related to the mechanical properties of the proton, such as the distribution of shear forces, the pressure distribution, the mechanical radius of the proton, and the angular momentum distribution. These quantities have never been measured before as they couple directly only to the gravitational field. The development of the generalized parton distributions and their relationship to the gravitational form factors through the second Mellin moments made this feasible in an indirect way. First results have been obtained recently [Bur18]. An experiment has been approved by PAC44 using a polarized electron beam to improved the precision of the pressure distribution. The use of the CLAS12 detector to broaden this program is natural as the expected polarized positron current is much lower than what can be achieved with polarized electron beams, and fits naturally with the capabilities of the CLAS12. Simulations have been made with realistic beam currents and beam polarization that show that the relevant observables can be measured with good accuracy and will have a very significant scientific impact.

## 7 n-DVCS @ CLAS12

# Beam Charge Asymmetries for Deeply Virtual Compton Scattering on the Neutron with CLAS12 at 11 GeV


**Abstract**

Measuring DVCS on a neutron target is a necessary step to deepen our understanding of the structure of the nucleon in terms of GPDs. The combination of neutron and proton targets allows to perform a flavor decomposition of the GPDs. Moreover, DVCS on a neutron target plays a complementary role to DVCS on a transversely polarized proton target in the determination of the GPD $E$, the least known and constrained GPD that enters Ji's angular momentum sum rule. We propose to measure, for the first time, the beam charge asymmetry (BCA) in the $e^{\pm}d \to e^{\pm}n\gamma(p)$ reactions, with the upgraded 11 GeV CEBAF positron/electron beams and the CLAS12 detector. The exclusivity of the final state will be ensured by detecting in CLAS12 the scattered lepton, the photon (including the Forward Tagger at low polar angles), and the neutron. Running 80 days on a deuterium target at the maximum CLAS12 luminosity ($10^{35}$ cm$^{-2}$·s$^{-1}$) will yield a rich BCA data set in the 4-dimensional ($Q^2$, $x_B$, $-t$, $\phi$) phase space. This observable will significantly impact the experimental determination of the real parts of the $\mathcal{E}_n$ and, to a lesser extent, $\widetilde{\mathcal{H}_n}$ Compton form factors.



*Spokespersons: S. Niccolai (niccolai@ipno.in2p3.fr), E. Voutier*

It is well known that the fundamental particles which form hadronic matter are the quarks and the gluons, whose interactions are described by the QCD Lagrangian. However, exact QCD-based calculations cannot yet be performed to explain all the properties of hadrons in terms of their constituents. Phenomenological functions need to be used to connect experimental observables with the inner dynamics of the constituents of the nucleon, the partons. Typical examples of such functions include form factors, parton densities, and distribution amplitudes. The GPDs are nowadays the object of intense research effort in the perspective of unraveling nucleon structure. They describe the correlations between the longitudinal momentum and transverse spatial position of the partons inside the nucleon, they give access to the contribution of the orbital momentum of the quarks to the nucleon, and they are sensitive to the correlated $q\bar{q}$ components of the nucleon wave function [Mul94, Die03, Bel05].

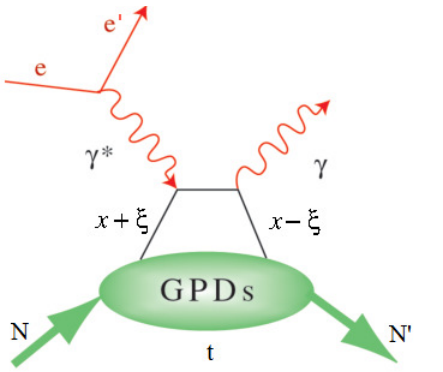


Figure 22. The handbag diagram for the DVCS process on the nucleon $eN \to e'N'\gamma'$; here $x+\xi$ and $x-\xi$ are the longitudinal momentum fractions of the struck quark before and after scattering, respectively, and $t = (N - N')^2$ is the squared four-momentum transfer between the initial and final nucleons. $\xi \simeq x_B/(2 - x_B)$ is proportional to the Bjorken scaling variable $x_B = Q^2/2M\nu$, where $M$ is the nucleon mass and $\nu$ is the energy transferred to the quark.

The nucleon GPDs are the structure functions which are accessed in the measurement of the exclusive leptoproduction of a photon (i.e. DVCS) or of a meson on the nucleon, at sufficiently large photon virtuality ($Q^2$) for the reaction to happen at the parton level. Figure 22 illustrates the leading process for DVCS, also called "handbag diagram". At leading-order QCD and at leading twist, considering only quark-helicity conserving quantities and the quark sector, the process is described by four GPDs: $H^q, \widetilde{H^q}, E^q, \widetilde{E^q}$, one for each quark flavor $q$, that account for the possible combinations of relative orientations of the nucleon spin and quark helicities between the initial and final states. $H^q$ and $E^q$ do not depend on the quark helicity and are therefore called unpolarized GPDs while $\widetilde{H^q}$ and $\widetilde{E^q}$ depend on the quark helicity and are called polarized GPDs. $H^q$ and $\widetilde{H^q}$ conserve the spin of the nucleon, whereas $E^q$ and $\widetilde{E^q}$ correspond to a nucleon-spin flip.
The GPDs depend upon three variables, $x$, $\xi$ and $t$: $x + \xi$ and $x - \xi$ are the longitudinal momentum fractions of the struck quark before and after scattering, respectively, and $t$ is the squared four-momentum transfer between the

initial and final nucleon (see caption of Fig. 22 for definitions). The transverse component of $t$ is the Fourier-conjugate of the transverse position of the struck parton in the nucleon. Among these three variables, only $\xi$ and $t$ are experimentally accessible with DVCS.

The DVCS amplitude is proportional to combinations of integrals over $x$ of the form

$$\int_{-1}^{1} dx\, F(\mp x, \xi, t) \left[ \frac{1}{x - \xi + i\epsilon} \pm \frac{1}{x + \xi - i\epsilon} \right], \tag{48}$$

where $F$ represents one of the four GPDs. The top combination of the plus and minus signs applies to unpolarized GPDs ($H^q, E^q$), and the bottom combination of signs applies to the polarized GPDs ($\widetilde{H^q}, \widetilde{E^q}$). Each of these 4 integrals or Compton Form Factors (CFFs) can be decomposed into their real and imaginary parts, as following:

$$\Re\mathrm{e}\,[\mathcal{F}(\xi, t)] = \mathcal{P} \int_{-1}^{1} dx \left[ \frac{1}{x - \xi} \mp \frac{1}{x + \xi} \right] F(x, \xi, t) \tag{49}$$

$$\Im\mathrm{m}\,[\mathcal{F}(\xi, t)] = -\pi [F(\xi, \xi, t) \mp F(-\xi, \xi, t)], \tag{50}$$

where $\mathcal{P}$ is Cauchy's principal value integral and the sign convention is the same as in Eq. 48. The information that can be extracted from the experimental data at a given $(\xi, t)$ point depends on the measured observable. $\Re\mathrm{e}[\mathcal{F}]$ is accessed primarily measuring observables which are sensitive to the real part of the DVCS amplitude, such as double-spin asymmetries, beam charge asymmetries or unpolarized cross sections. $\Im\mathrm{m}[\mathcal{F}]$ can be obtained measuring observables sensitive to the imaginary part of the DVCS amplitude, such as single-spin asymmetries or the difference of polarized cross-sections. However, knowing the CFFs does not define the GPDs uniquely. A model input is necessary to deconvolute their $x$-dependence.
The DVCS process is accompanied by the BH process (Fig. 2), in which the final-state real photon is radiated by the incoming or scattered electron and not by the nucleon itself. The BH process, which is not sensitive to GPDs, is experimentally indistinguishable from DVCS and interferes with it at the amplitude level (Sec. 2.2). However, considering that the nucleon form factors are well known at small $t$, the BH process is precisely calculable.

### *7.2 Neutron GPDs and flavor separation*

The importance of neutron targets in the DVCS phenomenology was clearly established in the pioneering Hall A experiment, where the polarized-beam cross section difference off a neutron, from a deuterium target, was measured [Maz07]. Measuring neutron GPDs in complement to proton GPDs allows for their quark-flavor separation. For instance, the $\mathcal{E}$-CFF of the proton and of the neutron can be expressed as

$$\mathcal{E}_p(\xi,t) = \frac{4}{9}\mathcal{E}^u(\xi,t) + \frac{1}{9}\mathcal{E}^d(\xi,t) \tag{51}$$

$$\mathcal{E}_n(\xi,t) = \frac{1}{9}\mathcal{E}^u(\xi,t) + \frac{4}{9}\mathcal{E}^d(\xi,t) \tag{52}$$

(and similarly for $\mathcal{H}$, $\widetilde{\mathcal{H}}$ and $\widetilde{\mathcal{E}}$). The $u$- and $d$-quark CFFs can be determined as:

$$\mathcal{E}^u(\xi,t) = \frac{9}{15}\left[4\mathcal{E}_p(\xi,t) - \mathcal{E}_n(\xi,t)\right] \tag{53}$$

$$\mathcal{E}^d(\xi,t) = \frac{9}{15}\left[4\mathcal{E}_n(\xi,t) - \mathcal{E}_p(\xi,t)\right] . \tag{54}$$

An extensive experimental program dedicated to the measurement of the DVCS reaction on a proton target has been approved at Jefferson Lab, in particular with CLAS12. Single-spin asymmetries with polarized beam and/or linearly or transversely polarized proton targets, as well as unpolarized and polarized cross sections, will be measured with high precision over a vast kinematic coverage. A similar experimental program on the neutron will allow the quark flavor separation of the various GPDs. The beam spin asymmetry for n-DVCS, particularly sensitive to the GPD $E_n$ will be soon measured at CLAS12, involving direct detection of the active neutron [Nic11], unlike the pioneer Hall A measurement [Maz07]. Additionally, the measurement of single- and double-spin asymmetries with a longitudinally polarized neutron target is also foreseen for the nearby future at CLAS12 [Nic15]. The present letter focuses on the extraction of one more observable, the beam charge asymmetry. The next sections outline the benefits of this observable for the determination of the CFFs.

### *7.3 Beam charge asymmetry*

Considering unpolarized electron and positron beams, the sensitivity of the $eN \to eN\gamma$ cross section to the lepton-beam charge (Sec. 2.2) can be expressed with the beam-charge asymmetry observable [Hos16]

$$A_{\mathrm{C}}(\phi) = \frac{d^4\sigma^+ - d^4\sigma^-}{d^4\sigma^+ + d^4\sigma^-} = \frac{d^4\sigma^{\mathrm{I}}_{UU}}{d^4\sigma^{\mathrm{BH}}_{UU} + d^4\sigma^{\mathrm{DVCS}}_{UU}} , \tag{55}$$

which isolates the BH-DVCS interference contribution at the numerator and the DVCS amplitude at the denominator. Following the harmonic decomposition of observables proposed in Ref. [Bel02],

$$d^4\sigma^{\mathrm{BH}}_{UU} = \frac{K_1}{\mathcal{P}_1(\phi)\,\mathcal{P}_2(\phi)} \sum_{n=1}^{2} c^{\mathrm{BH}}_{n,\mathrm{unp}} \cos(n\phi) \tag{56}$$

$$d^4\sigma^{\mathrm{DVCS}}_{UU} = \frac{K_3}{Q^2} \sum_{n=0}^{2} c^{\mathrm{DVCS}}_{n,\mathrm{unp}} \cos(n\phi) , \tag{57}$$

and

$$d^4\sigma^{\mathrm{I}}_{UU} = \frac{K_2}{\mathcal{P}_1(\phi)\,\mathcal{P}_2(\phi)} \sum_{n=0}^{3} c^{\mathrm{I}}_{n,\mathrm{unp}} \cos(n\phi) \tag{58}$$

where $K_i$'s are kinematical factors, and $P_i(\phi)$'s are the BH propagators. Because of the $1/Q^2$ kinematical suppression of the DVCS amplitude, the dominant contribution to the denominator of Eq. 55 originates from the BH amplitude. At leading twist, the dominant coefficients to the numerator are $c^{\mathrm{I}}_{0,\mathrm{unp}}$ and $c^{\mathrm{I}}_{1,\mathrm{unp}}$

$$c^{\mathrm{I}}_{0,\mathrm{unp}} \propto -\frac{\sqrt{-t}}{Q}\, c^{\mathrm{I}}_{1,\mathrm{unp}} \tag{59}$$

$$c^{\mathrm{I}}_{1,\mathrm{unp}} \propto \Re\mathrm{e}\left[F_1\mathcal{H} + \xi(F_1+F_2)\widetilde{\mathcal{H}} - \frac{t}{4M^2}F_2\mathcal{E}\right]. \tag{60}$$

Given the relative strength of $F_1$ and $F_2$ at small $t$ for a neutron target, the beam charge asymmetry becomes

$$A_{\mathrm{C}}(\phi) \propto \frac{1}{F_2}\, \Re\mathrm{e}\left[\xi\widetilde{\mathcal{H}_n} - \frac{t}{4M^2}\mathcal{E}_n\right]. \tag{61}$$

Therefore, the BCA is mainly sensitive to the real part of the GPD $E_n$ and, for selected kinematics, to the real part of the GPD $\widetilde{H_n}$.

Considering polarized electron and positron beams, two additional observables can be constructed: the charge difference ($\Delta^{LU}_{\mathrm{C}}$) and the charge average ($\Sigma^{LU}_{\mathrm{C}}$) beam helicity asymmetries [Hos16]:

$$\Delta^{LU}_{\mathrm{C}}(\phi) = \frac{(d^4\sigma^+_+ - d^4\sigma^+_-) - (d^4\sigma^-_+ - d^4\sigma^-_-)}{d^4\sigma^+_+ + d^4\sigma^+_- + d^4\sigma^-_+ + d^4\sigma^-_-} = \frac{d^4\sigma^{\mathrm{I}}_{LU}}{d^4\sigma^{\mathrm{BH}}_{UU} + d^4\sigma^{\mathrm{DVCS}}_{UU}} \tag{62}$$

$$\Sigma^{LU}_{\mathrm{C}}(\phi) = \frac{(d^4\sigma^+_+ - d^4\sigma^+_-) + (d^4\sigma^-_+ - d^4\sigma^-_-)}{d^4\sigma^+_+ + d^4\sigma^+_- + d^4\sigma^-_+ + d^4\sigma^-_-} = \frac{d^4\sigma^{\mathrm{DVCS}}_{LU}}{d^4\sigma^{\mathrm{BH}}_{UU} + d^4\sigma^{\mathrm{DVCS}}_{UU}} \tag{63}$$

which single out the sensitivity to the beam polarization of the interference and DVCS amplitudes. Following Ref. [Bel02], these can be written as:

$$d^4\sigma^{\mathrm{I}}_{LU} = \frac{K_2}{\mathcal{P}_1(\phi)\,\mathcal{P}_2(\phi)} \sum_{n=1}^{2} s^{\mathrm{I}}_{n,\mathrm{unp}} \sin(n\phi) \tag{64}$$

$$d^4\sigma^{\mathrm{DVCS}}_{LU} = \frac{K_3}{Q^2}\, s^{\mathrm{DVCS}}_{1,\mathrm{unp}} \sin(\phi)\,, \tag{65}$$

where $s^{\mathrm{I}}_{1,\mathrm{unp}}$ is the dominant twist-2 contribution, proportional to the imaginary part of $c^{\mathrm{I}}_{1,\mathrm{unp}}$ (Eq. 60), and $s^{\mathrm{I}}_{2,\mathrm{unp}}$ and $s^{\mathrm{DVCS}}_{1,\mathrm{unp}}$ are twist-3 contributions with distinct GPD dependence and different harmonic behaviour. Eq. 62 should be compared to the beam-spin asymmetry (BSA) observable

$$A_{LU}(\phi) = \frac{d^4\sigma_+^- - d^4\sigma_-^-}{d^4\sigma_+^- + d^4\sigma_-^-} = \frac{d^4\sigma_{LU}^{\rm DVCS} - d^4\sigma_{LU}^{\rm I}}{d^4\sigma_{UU}^{\rm BH} - d^4\sigma_{UU}^{\rm I} + d^4\sigma_{UU}^{\rm DVCS}} , \tag{66}$$

to be measured at CLAS12 with a polarized electron beam. Eq. 66 can be expressed as

$$A_{LU} = \frac{\Sigma_{\rm C}^{LU}}{1 - A_{\rm C}} - \frac{\Delta_{\rm C}^{LU}}{1 - A_{\rm C}} . \tag{67}$$

At leading twist $\Sigma_{\rm C}^{LU}$=0, and $A_{LU}$ differs from $\Delta_{\rm C}^{LU}$ due to the contribution of the polarization-independent part of the interference amplitude in the denominator. In that sense, $\Delta_{\rm C}^{LU}$ offers a complementary observable for the extraction of the CFFs. On the other hand, $\Sigma_{\rm C}^{LU}$ represents a new observable measuring the effects of higher twist in the $eN\gamma$ reaction. However, corresponding asymmetries are assumed to be small and then difficult to assess with precision. While the present letter concerns the BCA measurement, it should be stress that polarization observables will come from free if, as expected, the proposed positron beam at JLab operates similarly to the actual electron beam.

### *7.4 Experimental set-up*

We are proposing to measure the beam charge asymmetry for the electroproduction of photons on the neutron using a liquid deuterium target, the 11 GeV CEBAF electron beam, and the proposed 11 GeV positron beam. The scattered electrons/positrons and photons will be detected with the CLAS12 detector in its baseline configuration, completed at small angles with the Forward Tagger (FT) [Bat11]. The detection of the active neutrons will be accomplished with the CND (Central Neutron Detector) and the CTOF (Central Time-of-Flight) at backwards angles, and the FEC (Forward Electromagnetic Calorimeter), the PCAL (Preshower Calorimeter), and the FTOF (Forward Time-of-Flight) at forward angles. In order to match the detector acceptance for the different lepton beam charges, the positron data taking will be performed with opposite polarities for the CLAS12 torus and solenoid, with respect to the electron data taking.

An event generator (GENEPI) for the DVCS, the BH and exclusive $\pi^0$ electroproduction processes on the neutron inside a deuterium target was developed [Ala09]. The DVCS amplitude is calculated according to the BKM formalism [Bel02], while the GPDs are taken from the standard CLAS DVCS generator [Van99, Goe01]. The initial Fermi-motion distribution of the neutron is determined from the Paris potential [Lac80]. The output of the event generator was fed through CLAS12 FASTMC, to simulate acceptance and resolution effects in CLAS12. Kinematic cuts to ensure the applicability of the GPD formalism ($Q^2 > 1$ GeV$^2/c^2$, $t > -1.2$ GeV$^2/c^2$, $W > 2$ GeV) have been applied. Figure 23(left) shows the coverage in $Q^2$, $x_B$ and $t$ obtained for the D$(e, en\gamma)p$ reaction with an electron or positron beam energy of 11 GeV and the appropriate magnet polarities. The three plots in Fig. 23(right) shows the energy/momentum distributions of final state particles: as expected,the

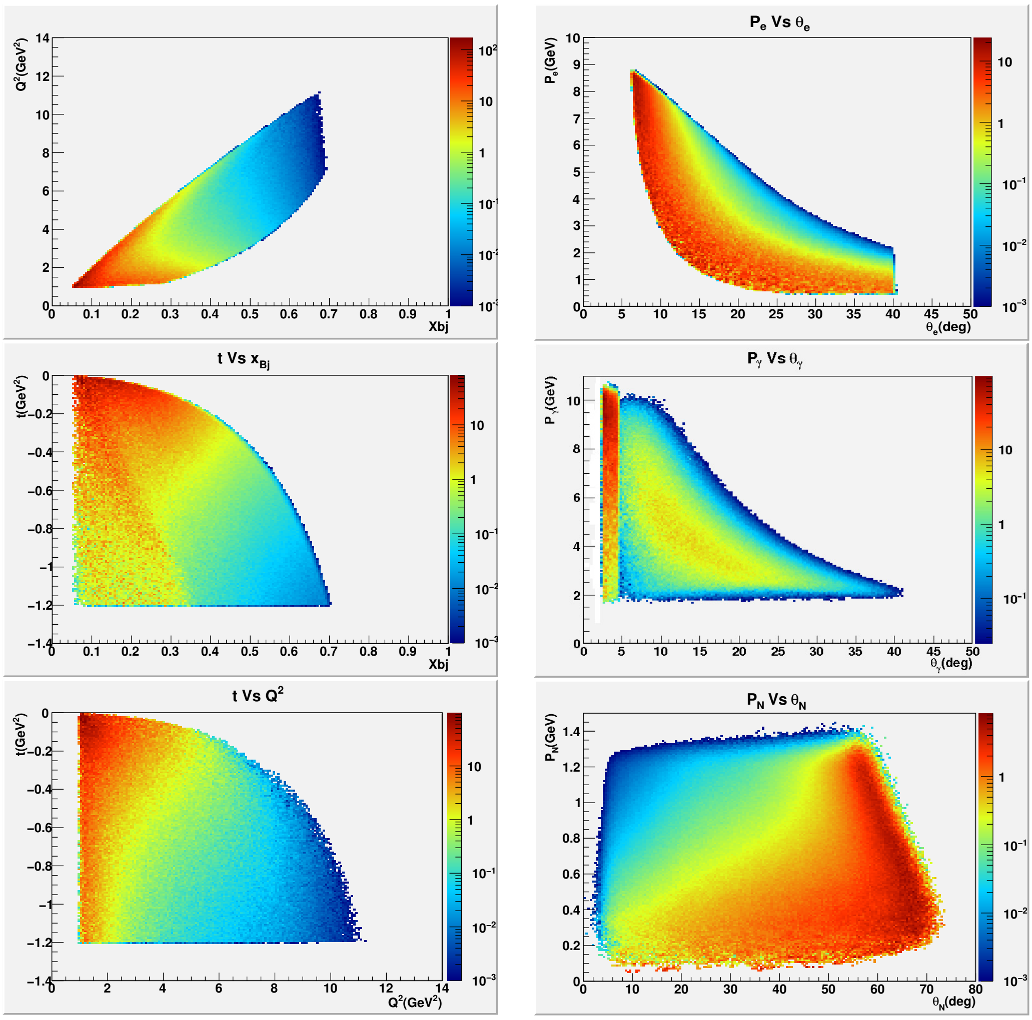


Figure 23. (left) Distributions of the kinematic variables for n-DVCS events, including acceptance and physics cuts: $(Q^2, x_B)$ phase space (top), $(t, x_B)$ phase space (middle), and $(t, Q^2)$ phase space (bottom). (right) Momentum distribution as function of polar angle for the $en\gamma(p)$ final state: electron/positron (top), photon (middle), and neutron momentum (bottom).

scattered leptons and the photons are mostly emitted at forward angles, while the recoil neutrons populate dominantly the backward angles region.

### *7.5 Projections for the beam-charge asymmetry*

The expected number of reconstructed $en\gamma(p)$ events was determined as a function of the kinematics. An overall 10% neutron-detection efficiency for neutrons with $\theta > 40^o$ was assumed (CND+CTOF). The detection efficiencies for electrons/positrons and photons are assumed to be 100%, within the fiducial cuts. Considering the always-improving performance of the CLAS12 data-acquisition system, the operation of CLAS12 at its design luminosity $\mathcal{L} = 10^{35}$ cm$^{-2}\cdot$s$^{-1}$ per nucleon, corresponding to 60 nA electron and positron beam currents, is assumed for the present data projections. An overall data

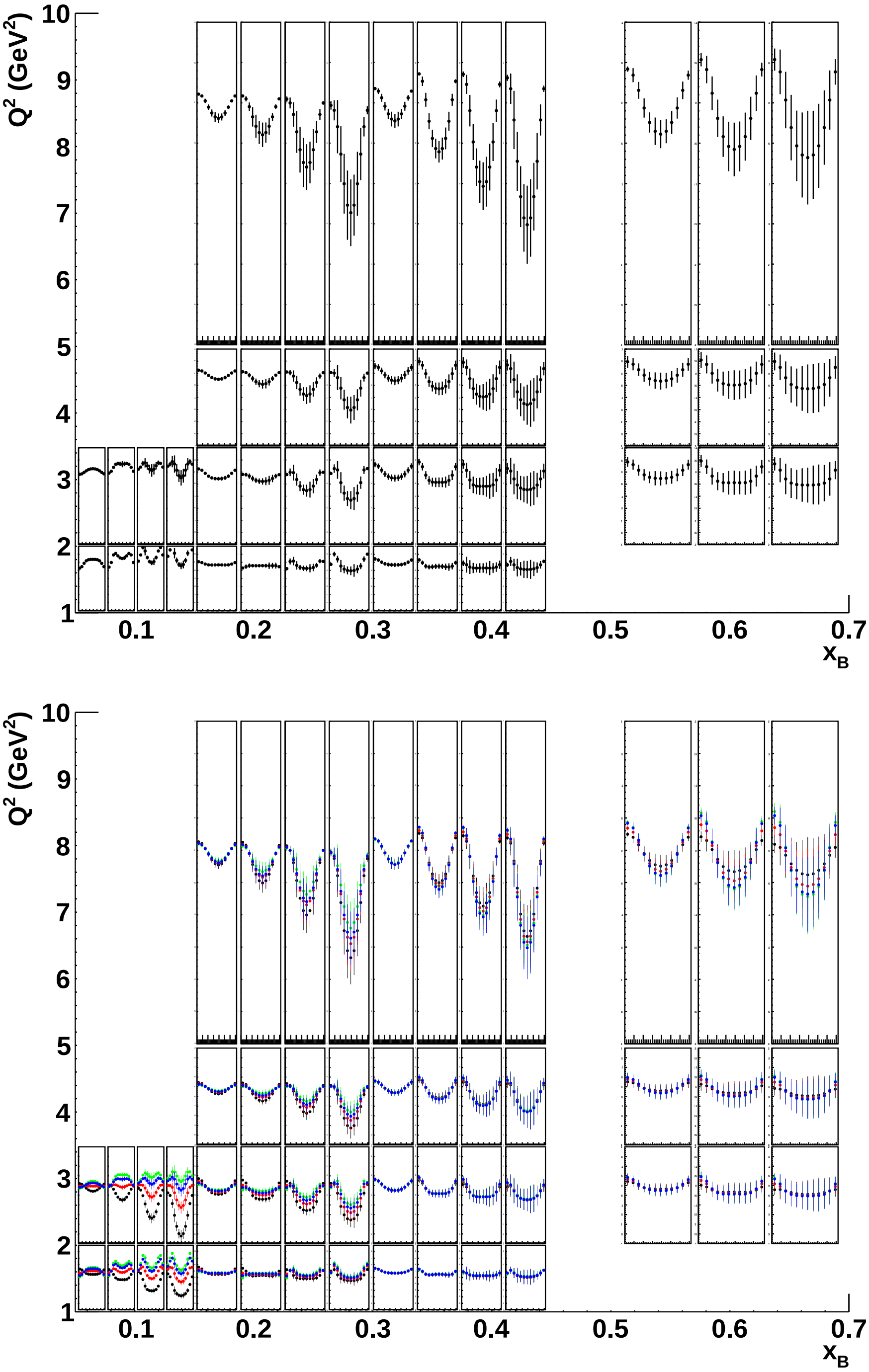


Figure 24. Projected BCA data for the D$(e, en\gamma)p$ reaction as predicted by the VGG model for $(J_u, J_d) = (0.3, 0.1)$ (top) and alternative combinations (bottom). The bottom plot compares $(J_u, J_d)$: $(0.3, 0.1)$ (black), $(0.2, 0.0)$ (red), $(0.1,$-$0.1)$ (green), and $(0.3,$-$0.1)$ (blue). The vertical axis scale ranges from -0.3 to 0.1 for the top plot and from -0.3 to 0.2 for the bottom plot. The error bars reflect the expected statistical uncertainties for 80 days of beam time at a luminosity of $10^{35}$ cm$^{-2}$·s$^{-1}$ per nucleon.

taking time of 80 days, equally shared between electrons and positrons, is also considered. The following 4-dimensional grid of bins has been adopted:

- 4 bins in $Q^2$ $[1, 2, 3.5, 5, 10\ \mathrm{GeV}^2/c^2]$;
- 4 bins in $-t$ $[0, 0.2, 0.5, 0.8, 1.2\ \mathrm{GeV}^2/c^2]$;
- 4 bins in $x_B$ $[0.05, 0.15, 0.3, 0.45, 0.7]$;
- 12 bins in $\phi$, each $30^o$ wide.

For each bin, the beam charge asymmetry (BCA) is experimentally reconstructed as

$$A_{\mathrm{C}} = \frac{(N^+/Q^+) - (N^-/Q^-)}{(N^+/Q^+) - (N^-/Q^-)} \tag{68}$$

where $Q^\pm$ is the integrated charge for lepton beam of each polarity ($Q^+$=$Q^-$ in the present evaluation), and $N^\pm$ is the corresponding number of $en\gamma(p)$ events. For each bin $N^\pm$ is computed as:

$$N^\pm = \mathcal{L}^\pm \cdot T \cdot \frac{d\sigma}{dQ^2 dx_B dt d\phi} \cdot \Delta t \cdot \Delta Q^2 \cdot \Delta x_B \cdot \Delta\phi \cdot \mathcal{A} \cdot \epsilon_n \,, \tag{69}$$

where $\mathcal{L}^\pm$ is the beam luminosity, $T$ is the running time, $d^4\sigma/dQ^2 dx_B dt d\phi$ is the 4-fold differential cross section, $\Delta Q^2 \Delta x_B \Delta t \Delta\phi$ is the full bin width, $\mathcal{A}$ is the bin by bin acceptance, and $\epsilon_n$ is the neutron-detection efficiency. The statistical errors on the BCA depend on the BCA magnitude via the formula:

$$\sigma\left(A_{\mathrm{C}}\right) = \sqrt{\frac{1 - A_{\mathrm{C}}^2}{N}} \tag{70}$$

where $N$=$N^+ + N^-$ is the total number of events in each bin. Figure 24(top) shows the expected statistical accuracy of the proposed BCA measurement. The magnitude of the BCA is obtained for each bin with the VGG model assuming $J_u = 0.3$ and $J_d = 0.1$. Figure 24(bottom) shows the BCA for different $(J_u, J_d)$ values. It should be noted that the BCA is particularly sensitive to $(J_u, J_d)$ at small $x_B$, in comparison to the beam-spin asymmetry which depends linearly on $(J_u, J_d)$. This is most likely an effect of the $x$-dependence of GPDs.
Summing $N^\pm$ over for the full grid of bins, about $25{\times}10^6$ $en\gamma(p)$ events are expected to be collected over the full kinematic range for 80 days of running.

### *7.6 Extraction of Compton form factors*

In order to establish the impact of proposed experiment on the CLAS12 n-DVCS program, the four sets of projected asymmetries BSA [Nic11]), TSA and DSA [Nic15], and BCA (Fig. 24(top)), for all kinematic bins, were processed using a fitting procedure [Gui08, Gui13] to extract the neutron CFFs. This approach is based on a local-fitting method at each given experimental $(Q^2, x_B, -t)$ kinematic point. In this framework, there are eight real CFF-related quantities

$$F_{Re}(\xi,t) = \Re\mathrm{e}\left[\mathcal{F}(\xi,t)\right] \tag{71}$$

$$F_{Im}(\xi,t) = -\frac{1}{\pi}\Im\mathrm{m}\left[\mathcal{F}(\xi,t)\right] = \left[F(\xi,\xi,t) \mp F(-\xi,\xi,t)\right], \tag{72}$$

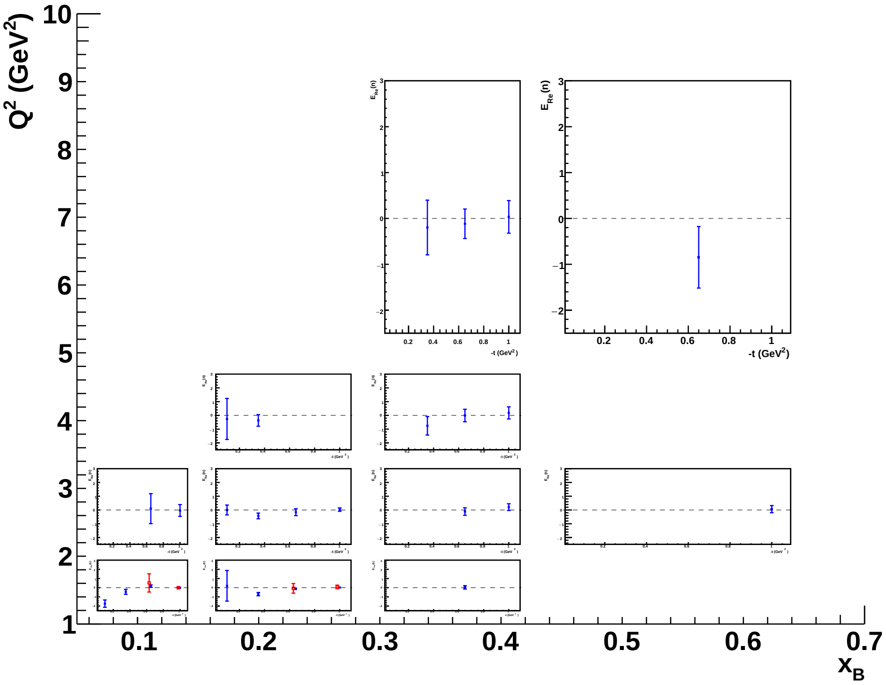

Figure 25. $E_{Re}(n)$ as a function of $-t$, for all bins in $Q^2$ and $x_B$. The blue points are the results of the fits including the proposed BCA while the red ones include only already approved experiments.

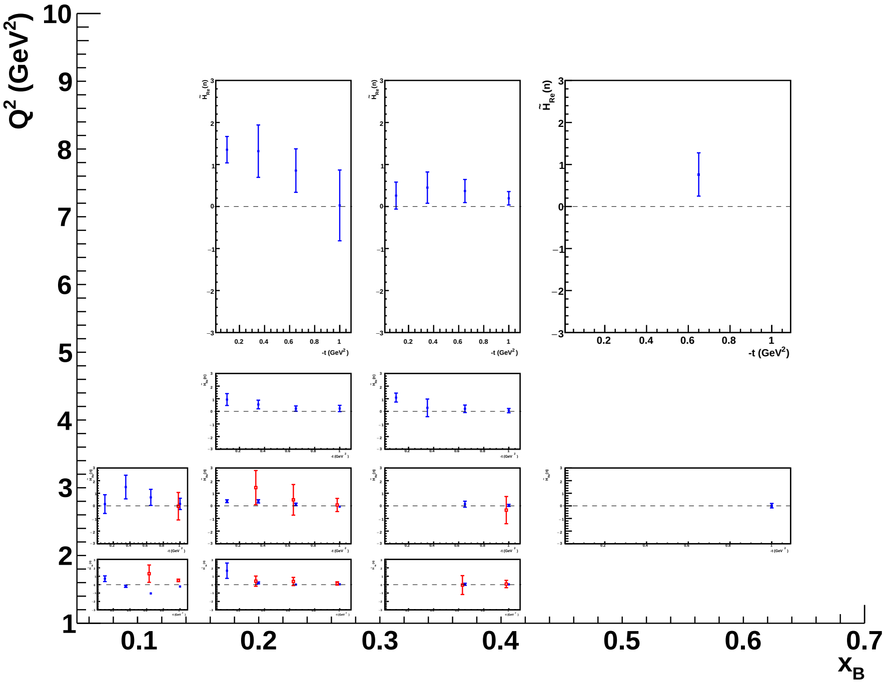

Figure 26. $\widetilde{H}_{Re}(n)$ as a function of $-t$, for all bins in $Q^2$ and $x_B$. The blue points are the results of the fits including the proposed BCA while the red ones include only already approved experiments.

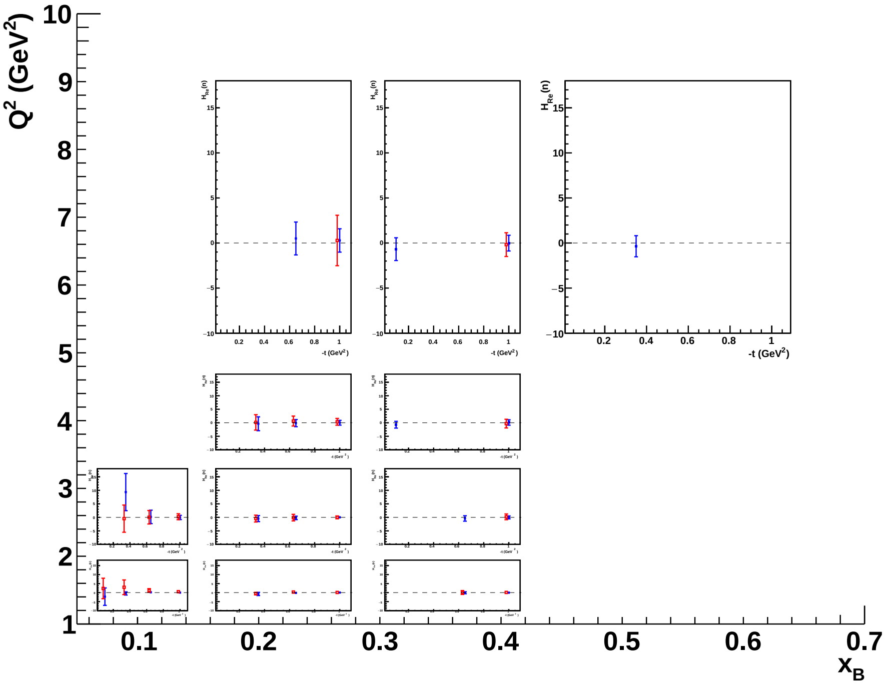


Figure 27. $H_{Re}(n)$ as a function of $-t$, for all bins in $Q^2$ and $x_B$. The blue points are the results of the fits including the proposed BCA while the red ones include only already approved experiments.

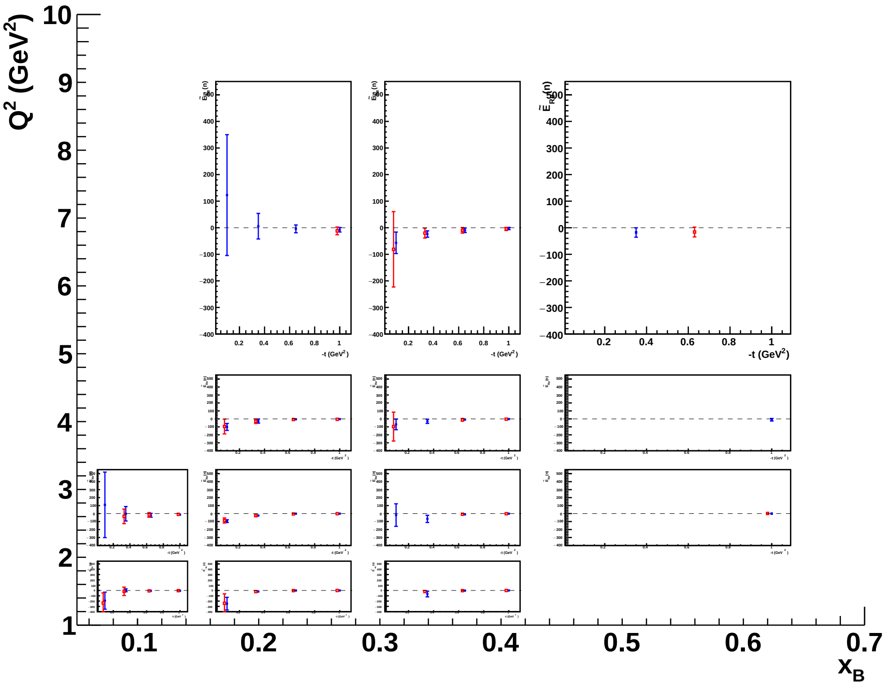


Figure 28. $\widetilde{E_{Re}}(n)$ as a function of $-t$, for all bins in $Q^2$ and $x_B$. The blue points are the results of the fits including the proposed BCA while the red ones include only already approved experiments.

where the sign convention is the same as for Eq. 48. These CFFs are the

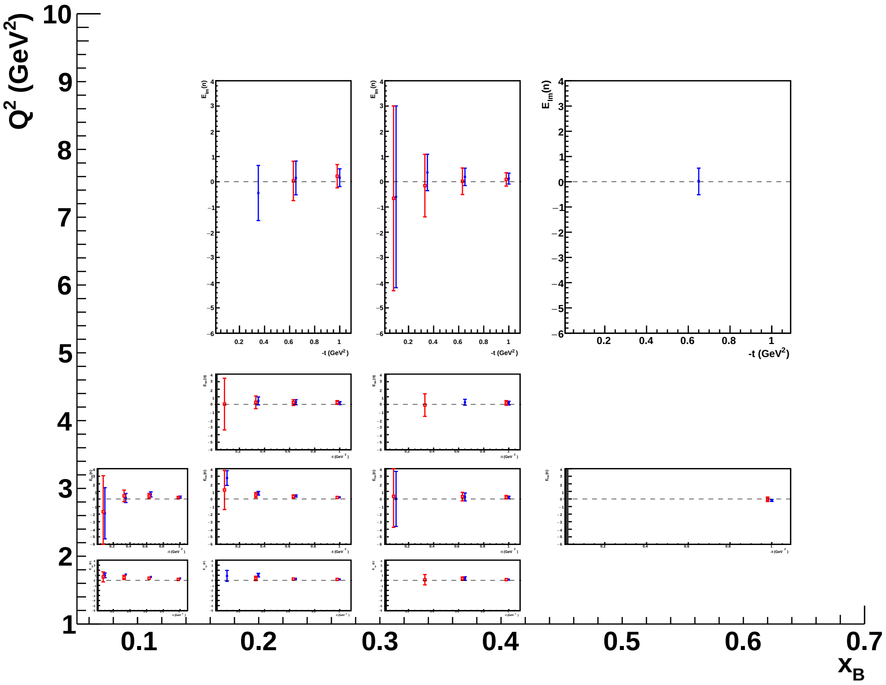


Figure 29. $E_{Im}(n)$ as a function of $-t$, for all bins in $Q^2$ and $x_B$. The blue points are the results of the fits including the proposed BCA while the red ones include only already approved experiments.

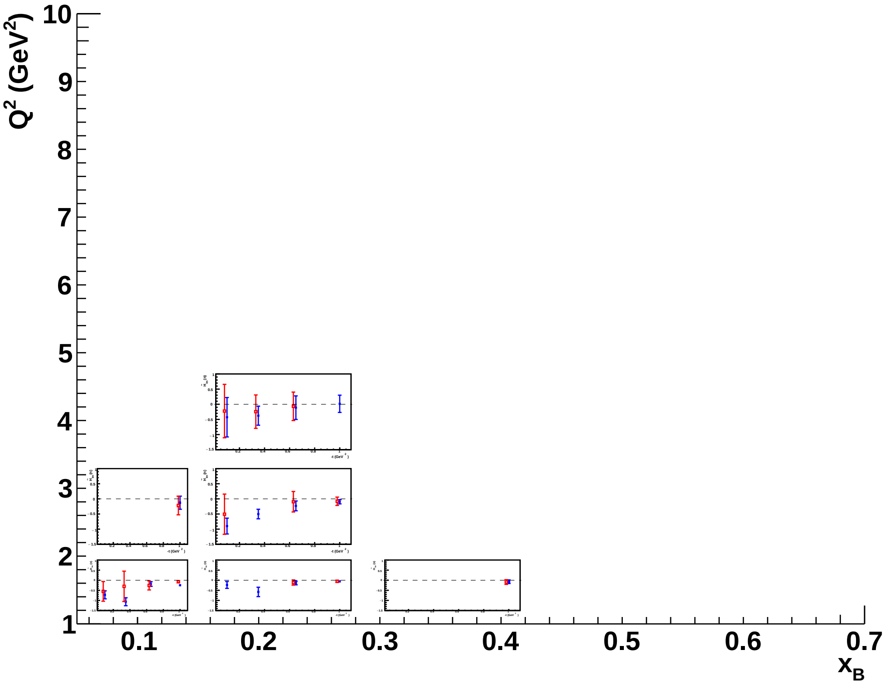


Figure 30. $\widetilde{H_{Im}}(n)$ as a function of $-t$, for all bins in $Q^2$ and $x_B$. The blue points are the results of the fits including the proposed BCA while the red ones include only already approved experiments.

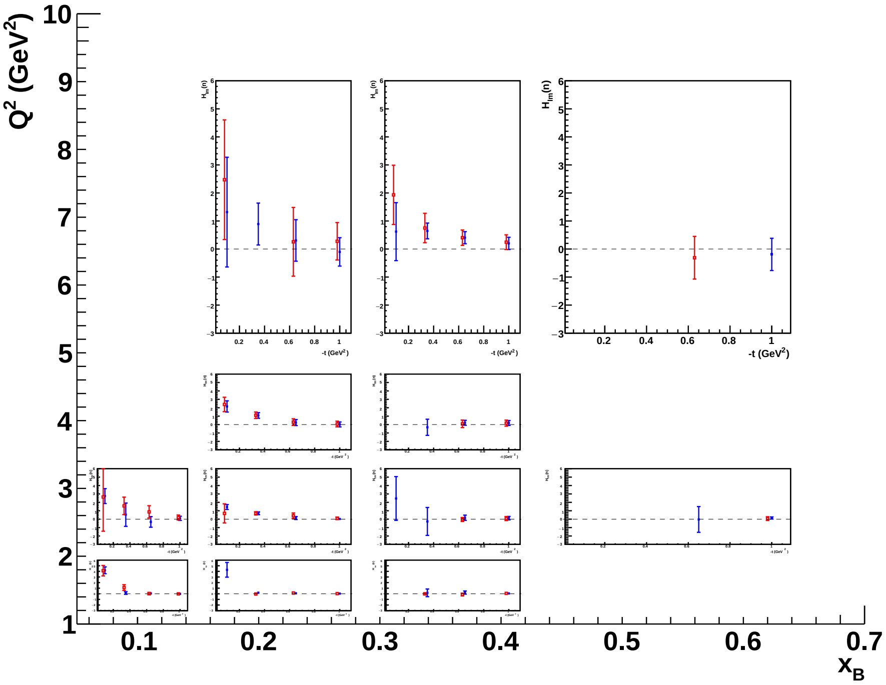


Figure 31. $H_{Im}(n)$ as a function of $-t$, for all bins in $Q^2$ and $x_B$. The blue points are the results of the fits including the proposed BCA while the red ones include only already approved experiments.

almost-free [1] parameters to be extracted from DVCS observables using the well-established theoretical description of the process based on the DVCS and BH mechanisms. The BH amplitude is calculated exactly while the DVCS one is determined at the QCD leading twist [Van99].

As there are eight CFF-related free parameters, including more observables measured at the same kinematic points will result in tighter constraint on the fit and will increase the number of CFFs and their accuracy. In the adopted version of the fitter code, $\widetilde{E_{Im}}(n)$ is set to zero, as $\widetilde{E}_n$ is assumed to be purely real. Thus, seven out of the eight real and imaginary parts of the CFFs are left as free parameters in the fit. The results for the 7 neutron CFFs are shown in Figs. 25-30, as a function of $-t$, and for each bin in $Q^2$ and $x_B$. The blue points are the CFFs resulting from the fits of the four observables, while the red ones are the CFFs obtained fitting only the projections of the currently approved n-DVCS experiments. The error bars reflect both the statistical precision of the fitted observables and their sensitivity to that particular CFF. Only results for which the error bars are non zero, and therefore the fits properly converged, are included in the figures.
The major impact of the proposed experiment is, as expected, on $E_{Re}(n)$, for which the already approved projections have hardly any sensitivity. Thanks to the proposed BCA measurement, $E_{Re}(n)$ will be extracted over basically the whole phase space. A considerable extension in the coverage will be obtained also for $\widetilde{H_{Re}}(n)$. An overall improvement to the precision on the other CFFs,

[1] The values of the CFFs are allowed to vary within $\pm5$ times the values predicted by the VGG model [Van99, Gui05].

as well as an extension in their kinematic coverage will also be induced by the proposed n-DVCS BCA dataset.

### *7.7 Systematic uncertainties*

The goal of this experiment is to measure beam charge asymmetries which are ratios of absolute cross sections. In this ratio, several charge-independent

| Source of error | $\sigma(A_{\mathrm{C}})^{Sys.}$ |
|---|---|
| Beam charge measurement | 3% |
| $\pi^0$ contamination | 5% |
| Acceptance | 3% |
| Radiative corrections | 3% |
| n-$\gamma$ misidentification | 5% |
| Total | 9% |

Table 5. Expected systematic uncertainties of the proposed measurement.

terms, such as acceptances, efficiencies, and radiative corrections, cancel out at first order. The BCA systematics comprises several contributions (Tab. 5) of comparable magnitude. The $\pi^0$-background evaluation, which depends on the accuracy of the description of the detector acceptance and efficiency, will contribute 5% to the overall systematic uncertainties. A similar contribution is expected from n-$\gamma$ misidentification. Due to its strong variation as a function of $\phi$, the acceptance will bring an additional 3% systematic error. A summary of the uncertainties induced by the various sources is reported in Tab. 5. The total systematic uncertainty is expected to be of the order of 9%.

### *7.8 Summary*

The strong sensitivity to the real part of the GPD $E^q$ of the beam charge asymmetry for DVCS on a neutron target makes the measurement of this observable particularly important for the experimental GPD program of Jefferson Lab.
GEANT4-based simulations show that a total of 80 days of beam time at full luminosity with CLAS12 will allow to collect good statistics for the n-DVCS BCA over a large phase space. The addition of this observable to already planned measurements with CLAS12, will permit the model-independent extraction of the real parts of the $\mathcal{E}_n$ and $\widetilde{\mathcal{H}_n}$ CFF of the neutron over the whole available phase space. Combining all the neutron and the proton CFFs obtained from the fit of n-DVCS and p-DVCS observables to be measured at CLAS12, will ultimately allow the quark-flavor separation of all GPDs.

## 8 p-DVCS @ Hall C

# Deeply Virtual Compton Scattering using a positron beam in Hall C

**Abstract**

We propose to use the High Momentum Spectrometer of Hall C combined with the Neutral Particle Spectrometer (NPS) to perform high precision measurements of the Deeply Virtual Compton Scattering (DVCS) cross section using a beam of positrons. The combination of measurements with opposite charge incident beams provide the only unambiguous way to disentangle the contribution of the $\mathrm{DVCS}^2$ term in the photon electroproduction cross section from its interference with the Bethe-Heitler amplitude. A wide range of kinematics accessible with an 11 GeV beam off an unpolarized proton target will be covered. The $Q^2$-dependence of each contribution will be measured independently.

*Spokesperon: C. Muñoz Camacho (munoz@ipno.in2p3.fr)*

Deeply Virtual Compton Scattering refers to the reaction $\gamma^* p \to p\gamma$ in the Bjorken limit of Deep Inelastic Scattering (DIS). Experimentally, we can access DVCS through electroproduction of real photons $ep \to ep\gamma$, where the DVCS amplitude interferes with the so-called Bethe-Heitler process. The BH contribution is calculable in QED since it corresponds to the emission of the photon by the incoming or the outgoing electron.

DVCS is the simplest probe of a new class of light-cone (quark) matrix elements, called Generalized Parton Distributions. The GPDs offer the exciting possibility of the first ever spatial images of the quark waves inside the proton, as a function of their wavelength [Mul94, Ji97, Ji97-1, Ji97-2, Rad96, Rad97]. The correlation of transverse spatial and longitudinal momentum information contained in the GPDs provides a new tool to evaluate the contribution of quark orbital angular momentum to the proton spin.

GPDs enter the DVCS cross section through integrals, called Compton Form Factors. CFFs are defined in terms of the vector GPDs $H$ and $E$, and the axial vector GPDs $\widetilde{H}$ and $\widetilde{E}$. For example ($q \in \{u, d, s\}$) [Bel02]:

$$\mathcal{H}(\xi, t) = \sum_q \left[\frac{e_q}{e}\right]^2 \Bigg\{ i\pi \left[H^q(\xi, \xi, t) - H^q(-\xi, \xi, t)\right] + \mathcal{P} \int_{-1}^{+1} dx \left[\frac{1}{\xi - x} - \frac{1}{\xi + x}\right] H^q(x, \xi, t) \Bigg\}. \tag{73}$$

Thus, the imaginary part accesses GPDs along the line $x = \pm\xi$, whereas the real part probes GPD integrals over $x$. The *diagonal* GPD, $H(\xi, \xi, t = \Delta^2)$ is not a positive-definite probability density, however it is a transition density with the momentum transfer $\Delta_\perp$ Fourier-conjugate to the transverse distance $r$ between the active parton and the center-of-momentum of the spectator partons in the target [Bur07]. Furthermore, the real part of the Compton form factor is determined by a dispersion integral over the diagonal $x = \pm\xi$ plus the $D$-term [Ter05, Die07, Ani07, Ani08]:

$$\Re\mathrm{e}\left[\mathcal{H}(\xi, t)\right] = \int_{-1}^{1} dx \left\{ \left[H(x, x, t) + H(-x, x, t)\right] \left[\frac{1}{\xi - x} - \frac{1}{\xi + x}\right] + 2\,\frac{D(x, t)}{1 - x} \right\} \tag{74}$$

The $D$-term [Pol99] only has support in the ERBL region $|x| < \xi$ in which the GPD is determined by $q\overline{q}$ exchange in the $t$-channel.

In this letter, we propose to exploit the charge dependence provided by the use of a positron beam in order to cleanly separate the DVCS$^2$ term from the DVCS-BH interference in the photon electroproduction cross section.

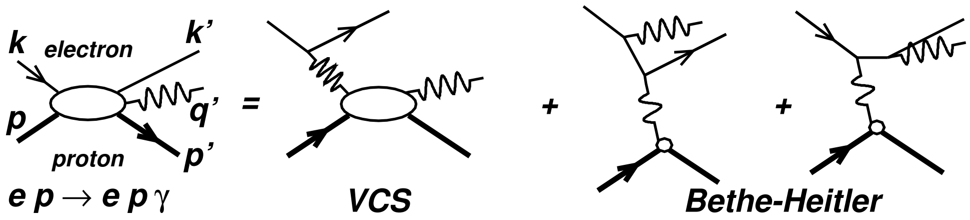


Figure 32. Lowest order QED amplitude for the $ep \to ep\gamma$ reaction. The momentum four-vectors of all external particles are labeled at left. The net four-momentum transfer to the proton is $\Delta_\mu = (q - q')_\mu = (p' - p)_\mu$. In the virtual Compton scattering (VCS) amplitude, the (spacelike) virtuality of the incident photon is $Q^2 = -q^2 = -(k - k')^2$. In the Bethe-Heitler (BH) amplitude, the virtuality of the incident photon is $-\Delta^2 = -t$. Standard $(e, e')$ invariants are $s_e = (k + p)^2$, $x_\mathrm{B} = Q^2/(2q \cdot p)$ and $W^2 = (q + p)^2$.

The photon electroproduction cross section of a polarized lepton beam of energy $k$ off an unpolarized target of mass $M$ is sensitive to the coherent interference of the DVCS amplitude with the Bethe-Heitler amplitude (see Fig. 32). It can be written as:

$$\begin{aligned}\frac{d^5\sigma(\lambda, \pm e)}{d^5\Phi} &= \frac{d\sigma_0}{dQ^2 dx_B} \left|\mathcal{T}^{BH}(\lambda) \pm \mathcal{T}^{DVCS}(\lambda)\right|^2 / |e|^6 \\ &= \frac{d\sigma_0}{dQ^2 dx_B} \left[\left|\mathcal{T}^{BH}(\lambda)\right|^2 + \left|\mathcal{T}^{DVCS}(\lambda)\right|^2 \mp \mathcal{I}(\lambda)\right] \frac{1}{e^6} \end{aligned} \tag{75}$$

with

$$\frac{d\sigma_0}{dQ^2 dx_B} = \frac{\alpha^3_{\mathrm{QED}}}{16\pi^2} \frac{1}{(s_e - M^2)^2 x_B} \frac{1}{\sqrt{1 + \epsilon^2}}\,, \tag{76}$$

and

$$\epsilon^2 = 4M^2 x_B^2 / Q^2\,, \tag{77}$$

$$s_e = 2Mk + M^2\,, \tag{78}$$

$$d^5\Phi = dQ^2 dx_B d\phi_e dt d\phi_{\gamma\gamma}\,. \tag{79}$$

Here, $\lambda$ is the electron helicity and the $+(-)$ stands for the sign of the charge of the lepton beam. The BH contribution is calculable in QED, given our $\approx 1\%$ knowledge of the proton elastic form factors at small momentum transfer. The other two contributions to the cross section, the interference and the DVCS$^2$ terms, provide complementary information on GPDs. It is possible to exploit the structure of the cross section as a function of the angle $\phi_{\gamma\gamma}$ between the leptonic and hadronic plane to separate up to a certain degree the different contributions to the total cross section [Die97]. The angular separation can be supplemented with a beam energy separation. The energy separation has been successfully used in previous experiments [Def17] at 6 GeV and is the goal of already approved experiments at 12 GeV [Mun13]. The $|\mathcal{T}^{BH}|^2$ term is given in [Bel02], and only its general form is reproduced here:

$$|\mathcal{T}^{BH}|^2 = \frac{e^6}{x_B^2 t y^2 (1+\epsilon^2)^2 \mathcal{P}_1(\phi_{\gamma\gamma})\mathcal{P}_2(\phi_{\gamma\gamma})} \sum_{n=0}^{2} c_n^{BH} \cos(n\phi_{\gamma\gamma}) \,. \tag{80}$$

The harmonic coefficients $c_n^{BH}$ depend upon bilinear combinations of the ordinary elastic form factors $F_1(t)$ and $F_2(t)$ of the proton. The factors $\mathcal{P}_i$ are the electron propagators in the BH amplitude [Bel02]. The interference term in Eq. 75 is a linear combination of GPDs, whereas the DVCS$^2$ term is a bilinear combination of GPDs. These terms have the following harmonic structure:

$$\begin{aligned}\mathcal{I} = \frac{e^6}{x_B y^3 \mathcal{P}_1(\phi_{\gamma\gamma})\mathcal{P}_2(\phi_{\gamma\gamma}) t} \Bigg\{ & c_0^{\mathcal{I}} \qquad (81)\\ & + \sum_{n=1}^{3} \left[ c_n^{\mathcal{I}}(\lambda) \cos(n\phi_{\gamma\gamma}) + \lambda s_n^{\mathcal{I}} \sin(n\phi_{\gamma\gamma}) \right] \Bigg\} ,\end{aligned}$$

and

$$\begin{aligned}\left|\mathcal{T}^{DVCS}(\lambda)\right|^2 = \frac{e^6}{y^2 Q^2} \Bigg\{ & c_0^{DVCS} \qquad (82)\\ & + \sum_{n=1}^{2} \left[ c_n^{DVCS} \cos(n\phi_{\gamma\gamma}) + \lambda s_n^{DVCS} \sin(n\phi_{\gamma\gamma}) \right] \Bigg\} .\end{aligned}$$

The $c_0^{DVCS,\mathcal{I}}$, and $(c,s)_1^{\mathcal{I}}$ harmonics are dominated by twist-two GPD terms, although they do have twist-three admixtures that must be quantified by the $Q^2$-dependence of each harmonic. The $(c,s)_1^{DVCS}$ and $(c,s)_2^{\mathcal{I}}$ harmonics are dominated by twist-three matrix elements, although the same twist-two GPD terms also contribute (but with smaller kinematic coefficients than in the lower Fourier terms). The $(c,s)_2^{DVCS}$ and $(c,s)_3^{\mathcal{I}}$ harmonics stem from twist-two double helicity-flip gluonic GPDs alone. They are formally suppressed by $\alpha_s$ and will be neglected here. They do not mix, however, with the twist-two quark amplitudes. The exact expressions of these harmonics in terms of the quark CFFs of the nucleon are given in [Bel10].

Eq. 75 shows how a positron beam, together with measurements with electrons, provides a way to separate without any assumptions the DVCS$^2$ and BH-DVCS interference contributions to the cross section. With electrons alone, the only approach to this separation is to use the different beam energy dependence of the DVCS$^2$ and BH-DVCS interference. This is the strategy that will be used in approved experiment E12-13-010. However, as recent results have shown [Def17] this technique has limitations due to higher order contributions (next-to-leading order in $\alpha_s$ or higher twists) and some assumptions needed. A positron beam, on the other hand, will be able to pin down each individual term. The $Q^2$ dependence of each of them can later be used to study the nature of the higher order contributions by comparing it to the predictions of the leading twist diagram.

### *8.3 Experimental setup*

We propose to make a precision coincidence setup measuring charged particles (scattered positrons) with the existing HMS and photons using the Neutral Particle Spectrometer (NPS), currently under construction. The NPS facility consists of a $PbWO_4$ crystal calorimeter and a sweeping magnet in order to reduce electromagnetic backgrounds. A high luminosity spectrometer+calorimeter (HMS+$PbWO_4$) combination is ideally suited for such measurements. The sweeping magnet will allow to achieve low-angle photon detection. Detailed background simulations show that this setup allows for $\geq 10\mu A$ beam current on a 10 cm long cryogenic $LH_2$ target at the very smallest NPS angles, and much higher luminosities at larger $\gamma, \pi^0$ angles [Mun13].

#### *High Momentum Spectrometer*

The magnetic spectrometers benefit from relatively small point-to-point uncertainties, which are crucial for absolute cross section measurements. In particular, the optics properties and the acceptance of the HMS have been studied extensively and are well understood in the kinematic range between 0.5 and 5 GeV, as evidenced by more than 200 L/T separations (∼1000 kinematics) [Lia04]. The position of the elastic peak has been shown to be stable to better than 1 MeV, and the precision rail system and rigid pivot connection have provided reproducible spectrometer pointing for more than a decade.

#### *Neutral Particle Spectrometer*

We will use the general-purpose and remotely rotatable NPS system for Hall C. A floor layout of the HMS and NPS is shown in Fig. 33(a). The NPS system consists of the following elements:

- A sweeping magnet providing 0.3 Tm field strength;
- A neutral particle detector consisting of 1080 $PbWO_4$ blocks (similar to the PRIMEX [Gas02] experimental setup, see Fig. 33(b)) in a temperature controlled frame, comprising a 25 msr device at a distance of 4 m;
- Essentially deadtime-less digitizing electronics to independently sample the entire pulse form for each crystal, allowing for background subtraction and identification of pile-up in each signal;
- A new set of high-voltage distribution bases with built-in amplifiers for operation in high-rate environments.
- Cantilevered platforms on the SHMS carriage, to allow for precise and remote rotation around the Hall C pivot of the full neutral-pion detection system, over an angle range between 6° and 30°;
- A dedicated beam pipe with as large critical angle as possible to reduce backgrounds beyond the sweeping magnet.

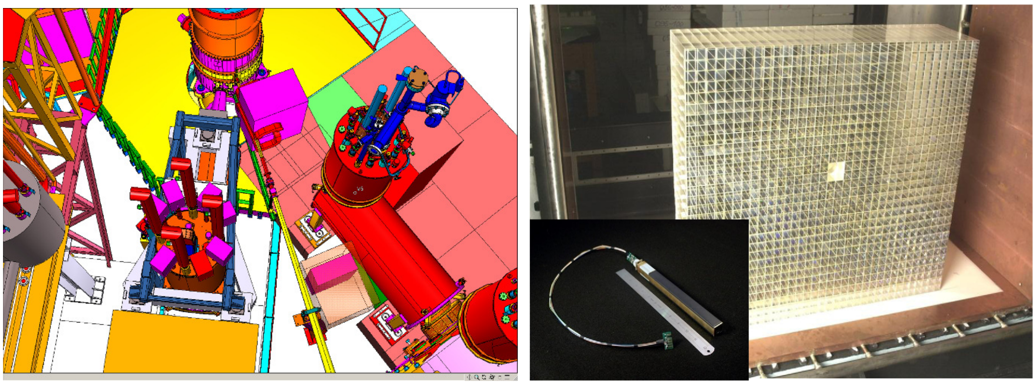

(a) (b)

Figure 33. (a) The DVCS/$\pi^0$ detector in Hall C. The cylinder at the top center is the (1 m diameter) vacuum chamber containing the 10 cm long liquid-hydrogen target. The long yellow tube emanating from the scattering chamber on the lower right is the downstream beam pipe. To the left of the beam pipe is the HMS. Only the liquid He and liquid $N_2$ lines for the large superconducting quadrupoles at the entrance of the spectrometer are clearly visible. To the right of the beam line, the first quadrupole of the SHMS and its cryogenic feed lines are shown. This spectrometer will be used as a carriage to support the $PbWO_4$ calorimeter (shown in its light-tight and temperature control box next to the beam line) and the associated sweep magnet. (b) The high resolution $PbWO_4$ part of the HYCAL [Kub06] on which the present NPS design is based.

*The $PbWO_4$ electromagnetic calorimeter*

The energy resolution of the photon detection is the limiting factor of the experiment. To ensure exclusivity of the reaction by the missing mass technique, we plan to use a $PbWO_4$ calorimeter 56 cm wide and 68 cm high. This corresponds to 30 by 36 $PbWO_4$ crystals of 2.05 by 2.05 cm$^2$ (each 20.0 cm long). We managed one crystal on each side to properly capture showers, and thus designed the $PbWO_4$ calorimeter to consist of 30 by 36 $PbWO_4$ crystals, or 60 by 72 cm$^2$. This amounts to a requirement of 1080 $PbWO_4$ crystals. To reject very low-energy background, a thin absorber could be installed in front of the $PbWO_4$ detector. The space between the sweeper magnet and the proximity of the $PbWO_4$ detector will be enclosed within a vacuum channel (with a thin exit window, further reducing low-energy background) to minimize the decay photon conversion in air. Given the temperature sensitivity of the scintillation light output of the $PbWO_4$ crystals, the entire calorimeter must be kept at a constant temperature, to within 0.1° to guarantee 0.5% energy stability for absolute calibration and resolution. The high-voltage dividers on the PMTs may dissipate up to several hundred Watts, and this power similarly must not create temperature gradients or instabilities in the calorimeter. The calorimeter will thus be thermally isolated and be surrounded on all four sides by water-cooled copper plates.

At the anticipated background rates, pile-up and the associated baseline shifts can adversely affect the calorimeter resolution, thereby constituting the limiting factor for the beam current. The solution is to read out a sampled signal, and perform offline shape analysis using a flash ADC (fADC) system. New HV distribution bases with built-in pre-amplifiers will allow for operating the PMTs at lower voltage and lower anode currents, and thus protect the photocathodes or dynodes from damage. To take full advantage of the high-resolution crystals while operating in a high-background environment, modern flash ADCs will be used to digitize the signal. They continuously sample the signal every 4 ns, storing the information in an internal FPGA memory. When a trigger is received, the samples in a programmable window around the threshold crossing are read out for each crystal that fired. Since the readout of the FPGA does not interfere with the digitizations, the process is essentially deadtime free.

The $PbWO_4$ crystals are 2.05 x 2.05 cm$^2$. The typical position resolution is 2-3 mm. Each crystal covers 5 mrad, and the expected angular resolution is 0.5-0.75 mrad, which is comparable with the resolutions of the HMS and SOS, routinely used for Rosenbluth separations in Hall C.

### *8.4 Exclusivity of the DVCS reaction*

The exclusivity of the DVCS reaction will be based on the missing mass technique, successfully used during Hall A experiments E00-110 and E07-007. Fig. 34 presents the missing mass squared obtained in E00-110 for $\mathrm{H}(e, e'\gamma)X$ events, with coincident electron-photon detection. After subtraction of an accidental coincidence sample, our data is essentially background free: there is negligible contamination of non-electromagnetic events in the HRS and $PbF_2$ spectra. In addition to $\mathrm{H}(e, e'\gamma)p$, however, we do have the following competing channels: $\mathrm{H}(e, e'\gamma)p\gamma$ from $ep \to e\pi^0 p$, $ep \to e\pi^0 N\pi$, $ep \to e\gamma N\pi$, $ep \to e\gamma N\pi\pi \ldots$. From symmetric (lab-frame) $\pi^0$-decay, we obtain a high statistics sample of $\mathrm{H}(e, e'\pi^0)X'$ events, with two photon clusters in the $PbF_2$ calorimeter. From these events, we determine the statistical sample of [asymmetric] $\mathrm{H}(e, e'\gamma)\gamma X'$ events that must be present in our $\mathrm{H}(e, e'\gamma)X$ data. The $M_X^2$ spectrum displayed in black in Fig. 34 was obtained after subtracting this $\pi^0$ yield from the total (green) distribution. This is a 14% average subtraction in the exclusive window defined by $M_X^2$ *cut* in Fig. 34. Depending on the bin in $\phi_{\gamma\gamma}$ and $t$, this subtraction varies from 6% to 29%. After $\pi^0$ subtraction, the only remaining channels, of type $\mathrm{H}(e, e'\gamma)N\pi$, $N\pi\pi$, *etc.* are kinematically constrained to $M_X^2 > (M + m_\pi)^2$. This is the chosen value for truncating the missing mass signal integration.
Resolution effects can cause the inclusive channels to contribute below this cut. To evaluate this possible contamination, during E00-110 we used an additional proton array (PA) of 100 plastic scintillators. The PA subtended a solid angle (relative to the nominal direction of the $\mathbf{q}$-vector) of $18^\circ < \theta_{\gamma p} < 38^\circ$ and $45^\circ < \phi_{\gamma p} = 180^\circ - \phi_{\gamma\gamma} < 315^\circ$, arranged in 5 rings of 20 detectors. For $\mathrm{H}(e, e'\gamma)X$ events near the exclusive region, we can predict which block in the PA should have a signal from a proton from an exclusive $\mathrm{H}(e, e'\gamma p)$ event. The red histogram is the $X = (p + y)$ missing mass squared distribution for $\mathrm{H}(e, e'\gamma p)y$ events in the predicted PA block, with a signal above an effective threshold 30 MeV (electron equivalent). The blue curve shows our inclusive yield, obtained by subtracting the normalized triple coincidence yield from the $\mathrm{H}(e, e'\gamma)X$ yield. The (smooth) violet curve shows our simulated $\mathrm{H}(e, e'\gamma)p$ spectrum, including radiative and resolution effects, normalized to

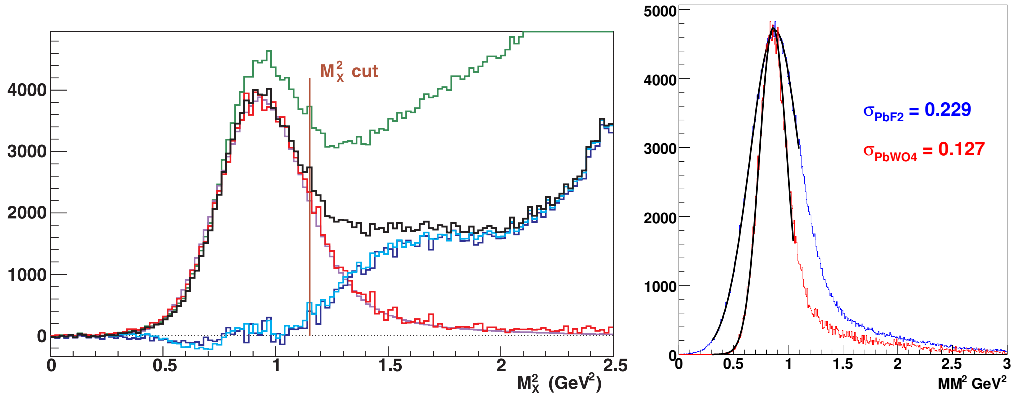


Figure 34. (Left) Missing mass squared in E00-110 for H$(e, e'\gamma)X$ events (green curve) at $Q^2 = 2.3$ GeV$^2$ and $-t \in [0.12, 0.4]$ GeV$^2$, integrated over the azimuthal angle of the photon $\phi_{\gamma\gamma}$. The black curve shows the data once the H$(e, e'\gamma)\gamma X'$ events have been subtracted. The other curves are described in the text. (Right) Projected missing mass resolution for a similar kinematic setting ($E_b = 6.6$ GeV, $Q^2 = 3$ GeV$^2$, $x_B = 0.36$). By using $PbWO_4$ instead of $PbF_2$, the missing mass resolution will be considerably improved. Values are given in Tab. 6 and are to be compared to the value $\sigma(M_X^2) = 0.2$ GeV$^2$ obtained in previous experiments in Hall A.

fit the data for $M_X^2 \leq M^2$. The cyan curve is the estimated inclusive yield obtained by subtracting the simulation from the data. The blue and cyan curves are in good agreement, and show that our exclusive yield has less than 2% contamination from inclusive processes.

In the presently proposed experiment we plan to use a $PbWO_4$ calorimeter with a resolution more than twice better than the $PbF_2$ calorimeter (Fig. 34 (Right) and Tab. 6) used in E00-110. While the missing mass resolution will be slightly worse at some high beam energy, low $x_B$ kinematics, the better energy resolution of the crystals will largely compensate for it, and the missing mass resolution in this experiment will be significantly better than ever before.

### *8.5 Proposed kinematics and projections*

Tab. 6 details the kinematics and beam time requested. $Q^2$ scans at 4 different values of $x_B$ were chosen in kinematics with already approved electron data [Mun13]. The positron beam current assumed is 5 $\mu$A (unpolarized beam). Beam time is calculated in order to match the statistical precision of the electron data, which in turn corresponds to the typical values of the expected systematic uncertainties.

The different kinematics settings are represented in Fig. 8.5 in the $Q^2$–$x_B$ plane. The area below the straight line $Q^2 = (2M_pE_b)x_B$ corresponds to the physical region for a maximum beam energy $E_b$=11 GeV. Also plotted is the resonance region $W < 2$ GeV. We have performed detailed Monte Carlo simulation of the experimental setup and evaluated counting rates for each of the settings. For this purpose, we have used a recent global fit of world data with LO sea evolution [Mul16]. This fit reproduces the magnitude of the

| $x_{\mathrm{Bj}}$ | 0.2 | | 0.36 | | | 0.5 | | 0.6 | |
|---|---|---|---|---|---|---|---|---|---|
| $Q^2$ (GeV)$^2$ | 2.0 | 3.0 | 3.0 | 4.0 | 5.5 | 3.4 | 4.8 | 5.1 | 6.0 |
| $k$ (GeV) | 11 | | 8.8 | | 11 | 11 | | 8.8 | 11 |
| $k'$ (GeV) | 5.7 | 3.0 | 4.4 | 2.9 | 2.9 | 7.4 | 5.9 | 4.3 | 5.7 |
| $\theta_{\mathrm{Calo}}$ (deg) | 10.6 | 6.3 | 14.7 | 10.3 | 7.9 | 21.7 | 16.6 | 17.8 | 17.2 |
| $D_{\mathrm{Calo}}$ (m) | 4 | 6 | 3 | 4 | 4 | 3 | 3 | 3 | 3 |
| $\sigma_{M_X^2}$ (GeV$^2$) | 0.17 | 0.22 | 0.13 | 0.15 | 0.19 | 0.09 | 0.11 | 0.09 | 0.09 |
| Days | 2 | 2 | 4 | 2 | 10 | 4 | 10 | 2 | 20 |

Table 6. DVCS kinematics with positrons in Hall C. The incident and scattered beam energies are $k$ and $k'$, respectively. The calorimeter is centered at the angle $\theta_{\mathrm{Calo}}$, which is set equal to the nominal virtual-photon direction. The front face of the calorimeter is at a distance $D_{\mathrm{Calo}}$ from the center of the target, and is adjusted to optimize multiple parameters: first to maximize acceptance, second to ensure sufficient separation of the two clusters from symmetric $\pi^0 \to \gamma\gamma$ decays, and third to ensure that the edge of the calorimeter is never at an angle less than $3.2°$ from the beam line.

DVCS cross section measured in Hall A at $x_B = 0.36$ and is available up to values of $x_B \leq 0.5$. For the high $x_B$ settings we used the GPD parametrization of Ref. [Kro13] fitted to deeply virtual meson production data, together with a code to compute DVCS cross sections [Mou13, Gui08-1]. Notice that for DVCS, counting rates and statistical uncertainties will be driven at first order by the well-known BH cross section.

The HMS is a very well understood magnetic spectrometer which will be used

| Source | pt-to-pt (%) | scale (%) |
|---|---|---|
| Acceptance | 0.4 | 1.0 |
| Electron/positron PID | <0.1 | <0.1 |
| Efficiency | 0.5 | 1.0 |
| Electron/positron tracking efficiency | 0.1 | 0.5 |
| Charge | 0.5 | 2.0 |
| Target thickness | 0.2 | 0.5 |
| Kinematics | 0.4 | <0.1 |
| Exclusivity | 1.0 | 2.0 |
| $\pi^0$ subtraction | 0.5 | 1.0 |
| Radiative corrections | 1.2 | 2.0 |
| Total | 1.8–1.9 | 3.8–3.9 |

Table 7. Estimated systematic uncertainties for the proposed experiment based on previous Hall C experiments.

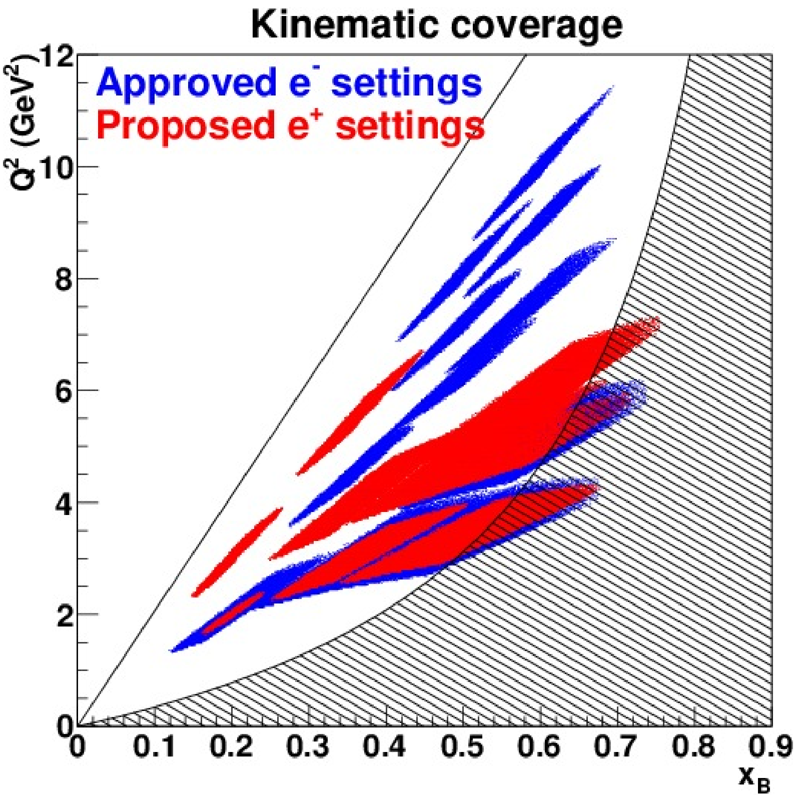


Figure 35. Display of the different kinematic settings proposed. Blue corresponds to the settings already approved in Hall A and Hall C using an electron beam. Red shows the proposed kinematics with positrons. Shaded areas show the resonance region $W < 2$ GeV and the line $Q^2 = (2M_pE_b)x_B$ limits the physical region for a maximum beam energy $E_b$=11 GeV.

here with modest requirements (beyond the momentum), defining well the $(x_B, Q^2)$ kinematics. Tab. 7 shows the estimated systematic uncertainties for the proposed experiment based on previous experience from Hall C equipment and Hall A experiments.

Fig. 36 shows the projected results for 3 selected settings at different values of $x_B$=0.2, 0.36, 0.5. Statistical uncertainties are shown by error bars and systematic uncertainties are represented by the cyan bands. The DVCS$^2$ term (which is $\phi$ independent at leading twist) can be very cleanly separated from the BH-DVCS interference contribution, without any assumption regarding the leading-twist dominance. The $Q^2$ dependence of each term will be measured (cf. Tab. 6) and compared to the asymptotic prediction of QCD. The extremely high statistical and systematic precision of the results illustrated in Fig. 36 will be crucial to disentangle higher order effects (higher twist or next-to-leading order contributions) as shown by recent results [Def17].

### *8.6 Summary*

We propose to measure the cross section of the DVCS reaction accurately using positrons in the wide range of kinematics allowed by a set of beam energies up

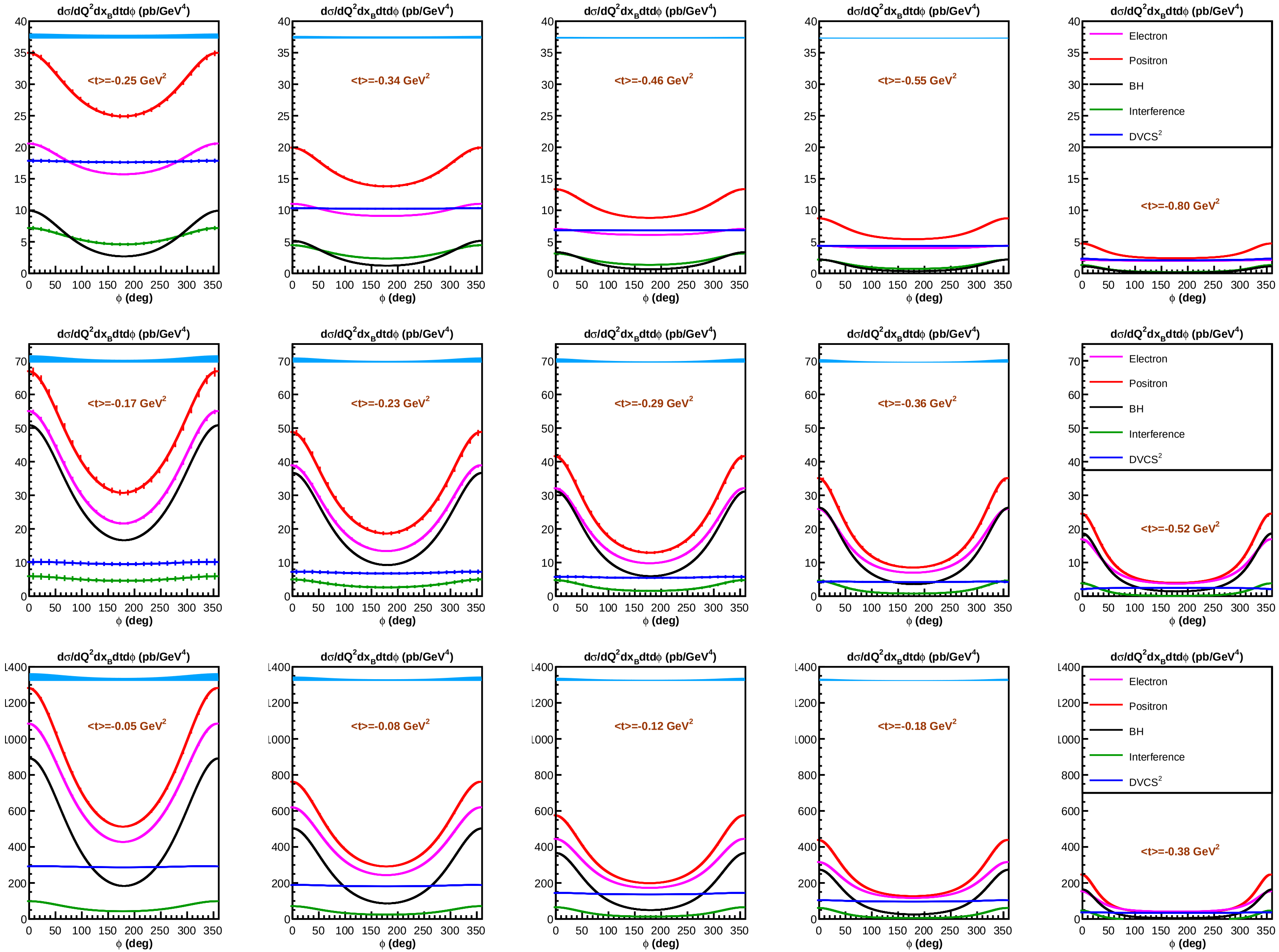


Figure 36. Experimental projections for 3 of the proposed settings: $x_B = 0.2$, $Q^2 = 2.0$ GeV$^2$ (top), $x_B = 0.36$, $Q^2 = 4.0$ GeV$^2$ (middle) and $x_B = 0.5$, $Q^2 = 3.4$ GeV$^2$ (bottom). Red points show the projected positron cross sections with statistical uncertainties. Electron cross sections that will be measured in experiment E12-13-010 are shown in magenta. The combination of $e^-$ and $e^+$ cross sections allow the separation of the DVCS$^2$ contribution (blue) and the DVCS-BH interference (green). For reference, the BH cross section is displayed in black. Systematic uncertainties are shown by the cyan band.

to 11 GeV. We will exploit the beam charge dependence of the cross section to separate the contribution of the BH-DVCS interference and the DVCS$^2$ terms. The $Q^2$ dependence of each individual term will be measured and compared to the predictions of the handbag mechanism. This will provide a quantitative estimate of higher-twist effects to the GPD formalism at JLab kinematics.

We plan to use Hall C High-Momentum Spectrometer, combined with a high resolution $PbWO_4$ electromagnetic calorimeter. In order to complete this full mapping of the DVCS cross section with positrons over a wide range of kinematics, we request 56 days of (unpolarized) positron beam ($I > 5\mu$A).

## 9 Dark photon search

# Searching for Dark Photon with Positrons at Jefferson Lab


### Abstract

The interest in the Dark Photon ($A'$) has recently grown, since it could act as a light mediator to a new sector of Dark Matter particles. In this paradigm, the electron-positron annihilation can rarely produce a $\gamma A'$ pair. Various experiments have been proposed to detect this process using positron beams impinging on fixed targets. In such experiments, the energy of the photon from the $e^+e^- \to \gamma A'$ process is measured with an electromagnetic calorimeter and the missing mass is computed. However, the $A'$ mass range that can be explored is limited by the accessible energy in the center of mass frame, scaling as the square root of the beam energy. The realization of a high energy positron beam at Jefferson Lab would allow to search for $A'$ masses up to $\sim$ 100 MeV, reaching unexplored regions of the $A'$ parameter space. We propose in this letter a PADME-like experiment at Jefferson Lab, assuming a 11 GeV positron beam with a $\sim$100 nA current. The achievable sensitivity of this experiment was estimated, studying the main sources of background using CALCHEP and GEANT4 simulations.



*Spokesperons: M. Battaglieri, A. Celentano, L. Marsicano (lmarsicano@ge.infn.it)*

The Standard Model (SM) of elementary particles and interactions is able to describe with an extraordinary precision ordinary matter in a variety of different environments and energy scales. However, some phenomena such as Dark Matter (DM), neutrino masses and matter-antimatter asymmetry do not fit in the scheme, calling for new physics beyond the SM. DM existence is highly motivated by various astrophisical observations but its fundamental properties remain to date unknown. Experimental efforts have been mainly focused, until today, in the WIMPs search (Weakly Interacting Massive Particles): in this paradigm, DM is made of particles with mass of order of $\sim 100 - 1000$ GeV interacting with the Standard Model via Weak force. Despite attaining the highest energy ever reached at accelerators, LHC has not yet been able to provide evidence for WIMPs-like particles. The same null results in direct detection of halo DM strongly constrains this class of models.

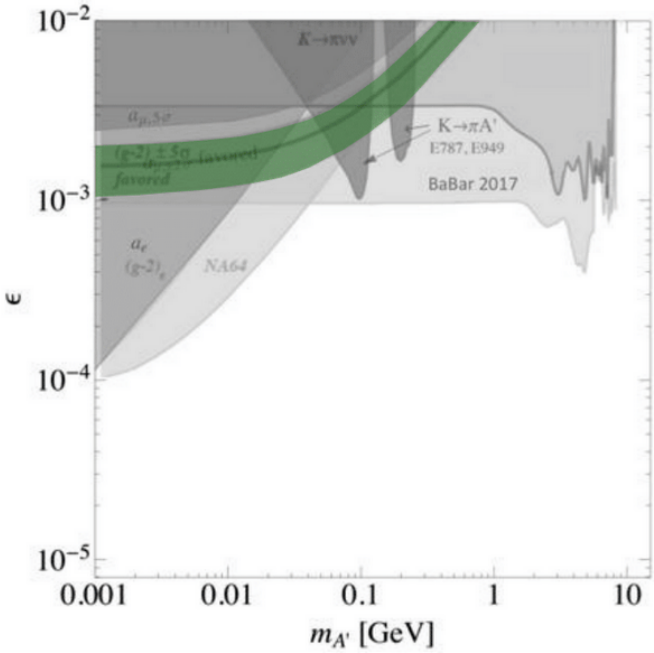


Figure 37. Current exclusion limits for $A'$ invisible decay.

Recently, the interest in new scenarios predicting DM candidates with lower masses has grown. Various models postulate the existence of a hidden sector interacting with the visible world through new *portal* interactions that are constrained by the symmetries of the SM. In particular, DM with mass below 1 GeV/$c^2$ interacting with the Standard model particles via a light boson (a heavy photon or $A'$, also called dark photon) represents a well motivated scenario that generated many theoretical and phenomenological studies. In this specific scenario the DM, charged under a new gauge symmetry $U(1)_D$ [Hol86], interacts with electromagnetic charged SM particles through the exchange of a dark photon. The interaction between the $A'$ and SM particles is generated effectively by a *kinetic mixing* operator. The low energy effective Lagrangian extending the SM to include dark photons can thus be written as

$$\mathcal{L}_{eff} = \mathcal{L}_{SM} - \frac{\epsilon}{2} F^{\mu\nu} F'_{\mu\nu} - \frac{1}{4} F'^{\mu\nu} F'_{\mu\nu} + \frac{1}{2} m^2_{A'} A'_\mu A'^\mu \tag{83}$$

where $F_{\mu\nu}$ is the usual electromagnetic tensor, $F'_{\mu\nu}$ is the $A'$ field strength, $m_{A'}$ is the mass of the heavy photon, and $\epsilon$ is the mixing coupling constant. In this scenario, SM particles acquire a dark *millicharge* proportional to $\epsilon^2$. The value of $\epsilon$ can be so small as to preclude the discovery of the $A'$ in the experiments carried out so far.

The decay of the $A'$ depends on the ratio between its mass and the mass of the dark sector particles: if the dark photon mass is smaller than twice the muon mass and no dark sector particle lighter than the $A'$ exists, it can only decay to $e^+e^-$ pairs (*Visible Decay*). Instead, if new $\chi$ particles with $2m_\chi < m_{A'}$ exist in the dark sector, the dominant dark photon decay mode is $A' \to \chi\bar{\chi}$ (*Invisible Decay*). In this letter, we only address the second scenario (see Fig. 37 for the current state of the $A'$ research in the *Invisible Decay* scenario).

### *9.2 Annihilation induced $A'$ production*

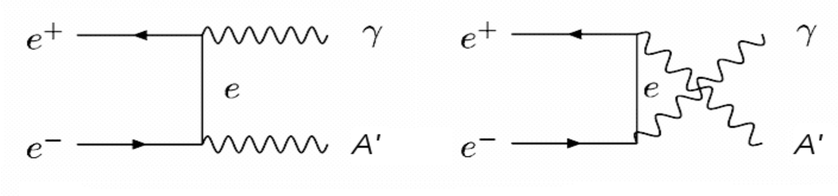


Figure 38. $A'$ production via $e^+e^-$ annihilation.

The $A'$ can be produced in $e^+e^-$ annihilation, via the $e^+e^- \to \gamma A'$ reaction (Fig. 38). Several experiments have been proposed to search for the production of $A'$ in this process (e.g. PADME@LNF [Rag14], and VEPP-3 [Woj17]). The first $e^+$ on target experiment searching for $A'$ is PADME (Positron Annihilation into Dark Matter Experiment) which uses the 550 MeV positron beam provided by the DAΦNE linac at LNF (Laboratori Nazionali di Frascati) impinging on a thin diamond target.

The experiment involves the detection of the photons from the annihilation process with a BGO electromagnetic calorimeter placed $\sim$ 2 m downstream of the interaction target. The $A'$ leaves the detector area without interacting. A magnetic field of $\sim$1 T bends away from the calorimenter the positron beam and all the charged particles produced in the target. A single kinematic variable, the missing mass, is computed for each event

$$M^2_{miss} = (P_{e^-} + P_{beam} - P_\gamma)^2 \,. \tag{84}$$

The corresponding distribution peaks at $M^2_{A'}$ in case of production of the $A'$. All processes resulting in a single $\gamma$ hitting the calorimeter constitute the experimental background. Among these, the most relevant are: bremsstrahlung, annihilation into $2\gamma$ ($e^+e^- \to \gamma\gamma$), annihilation into $3\gamma$ ($e^+e^- \to \gamma\gamma\gamma$). In order to reduce the bremsstrahlung background, the PADME detector features an active veto system composed of plastic scintillators: positrons losing energy via bremmstrahlung in the target are detected in the vetos, allowing to reject the event. However, the pile-up of the bremsstrahlung events is an issue for this class of experiments, limiting the maximum viable beam current of the beam. For this reason, a beam with a continuous structure would be the best option for a PADME-like experiment.

The sensitivity of PADME-like experiments in the $A'$ parameter space is constrained by the available energy in the center of mass frame: with a beam energy of ~500 MeV, PADME can search for masses up to 22.5 MeV. Higher energy positron beams are required to exceed these limits. In this letter, the achievable sensitivity of a Dark Photon experiment using the proposed 11 GeV continuous positron beam at JLab is discussed.

### *9.3 Searching for $A'$ with positrons at Jefferson Lab*

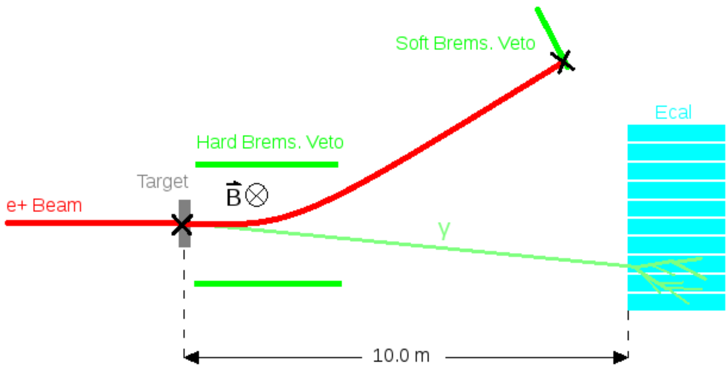


Figure 39. Schematic of the proposed experiment at Jefferson Lab.

The perspective of a high energy continuous positron beam at Jlab is particularly attractive to enlarge the reach of the $A'$ search in the annihilation channel. For a 11 GeV positron beam, the mass region up to ~106 MeV can be investigated. The experimental setup foreseen for such an experiment at JLab is presented in Fig. 39. It features:

*i)* A 100 $\mu$m thick carbon target, as a good compromise between density and a low $Z/A$ ratio to minimize bremsstrahlung production;
*ii)* A 50 cm radius highly segmented ($1\times1\times20$ cm$^3$ crystals) electromagnetic calorimeter placed 10 m downstream of the target, and with the energy resolution $\sigma(E)/E{=}0.02/\sqrt{E(GeV)}$;
*iii)* An active veto system with a detection efficiency higher than 99.5% for charged particles;
*iv)* A magnet supporting a field of 1 T over a 2 m region downstream of the target, and bend the positron beam.

Experimental projections are evaluated assuming an adjustable beam current betwen 10-100 nA, a momentum dispersion beeter than 1%, and an angular dispersion better than 0.1 mrad. It should be noticed that momentum and angular dispersion are critical parameters for such an experiment, since a good knowledge of the beam particles initial state is fundamental for the missing mass calculation. Given the low current involved, a natural location for this experimental setup could be JLab Hall B; in this case the electromagnetic calorimeter could be placed in the downstream alcove.

### *9.4 Experimental projections*

The study of the reconstructed missing mass distribution for the background events serves as a basic criteria to evaluate the sensitivity of the proposed experimental setup. As discussed previously, the main background processes of this experiment are bremsstrahlung and electron-positron annihilation into 2 or 3 photons, which can result in a single hit in the calorimeter. Different strategies were adopted to study the impact of these backgrounds.

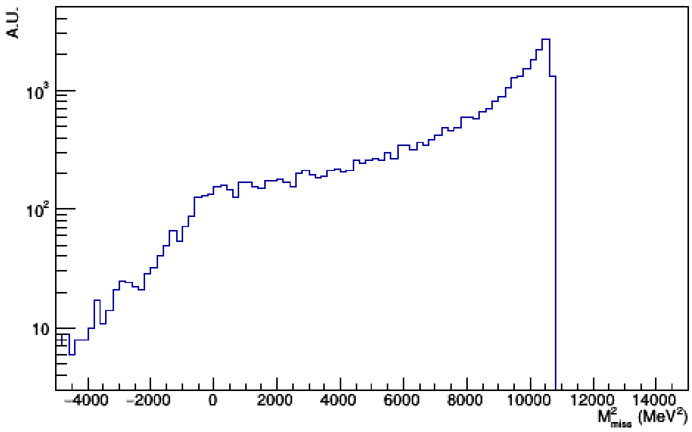


Figure 40. Calculated missing mass spectrum of bremsstrahlung events.

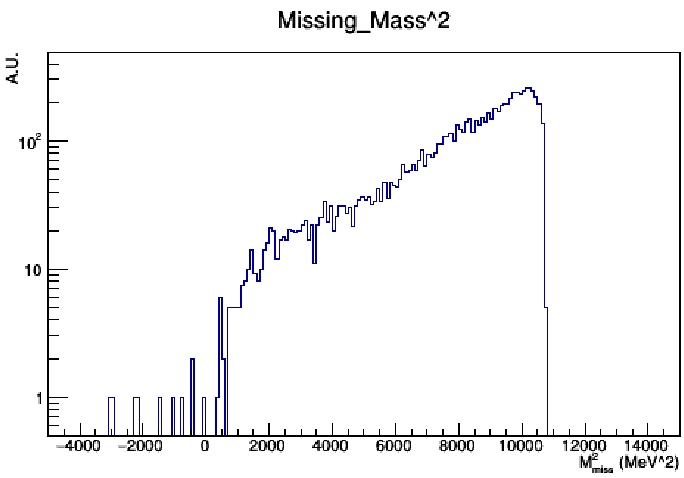


Figure 41. Calculated missing mass spectrum of 3 photons events.

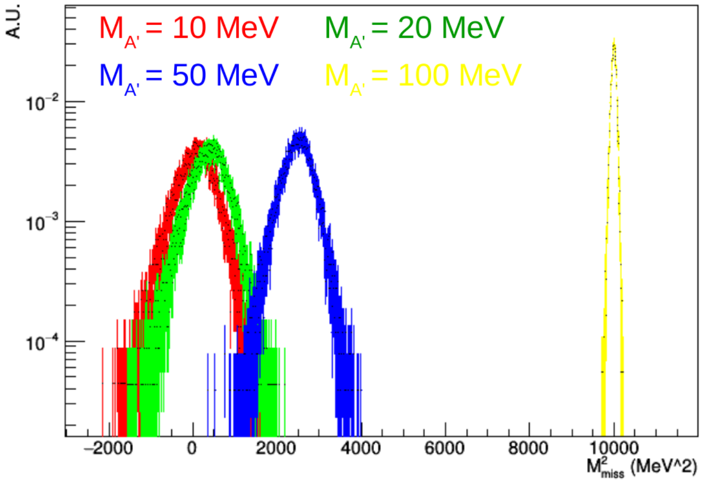


Figure 42. Calculated missing mass spectrum of signal events at 4 different $m_{A'}$ values.

Considering the bremsstrahlung background, a full GEANT4 [Ago03] simulation of the positron beam interacting with the target was performed. The missing mass was computed for all bremsstrahlung photons reaching the calorimeter volume, accounting for the detector angular and momentum resolution. Figure 40 shows the obtained spectrum. The total rate of expected bremsstrahlung events for positron on target was scaled accounting for the effect of the veto system.

The annihiliation into 2 or 3 photons is much less frequent than bremsstrahlung and was therefore studied differently: events were generated directly using CALCHEP [Puk04] which provided also the total cross sections for the processes. Photons generated in the annihilation were propagated to the calorimeter volume using a custom code and, as in the case of bremsstrahlung, missing mass spectrum was computed for events with a single $\gamma$-hit in the calorimeter. This study proved that, if an energy cut of 600 MeV is applied, the $2\gamma$-background becomes negligible. This is due to the closed kinematics of the $e^+e^- \to \gamma\gamma$ process: asking for only one photon to hit the detector translates in a strong constraint on its energy. This argument is not valid for the $3\gamma$-events: the number of background events from this process is in fact not negligible (see Fig. 41 for the missing mass spectrum).

Signal events were simulated using CALCHEP. The widths $\sigma(m_{A'})$ of the missing mass distributions of the measured recoil photon from the $e^+e^- \to \gamma A'$ process were computed for six different values of the $A'$ mass in the 1-103 MeV range. Figure 42 shows the corresponding spectra: the missing mass resoluton of the signal is maximum for at high $A'$ masses and degrades at low masses ($m_{A'} < 50$ MeV). As for the annihilation background, CALCHEP provides the total cross section of the process for a full coupling strength ($\varepsilon = 1$). It is then necessary to multiply it with $\epsilon^2$ to obtain the cross section for different coupling values.

The reach of the proposed experiment is obtained from the comparison of the signal and background spectra. A period of 180 days at 10(100) nA positron

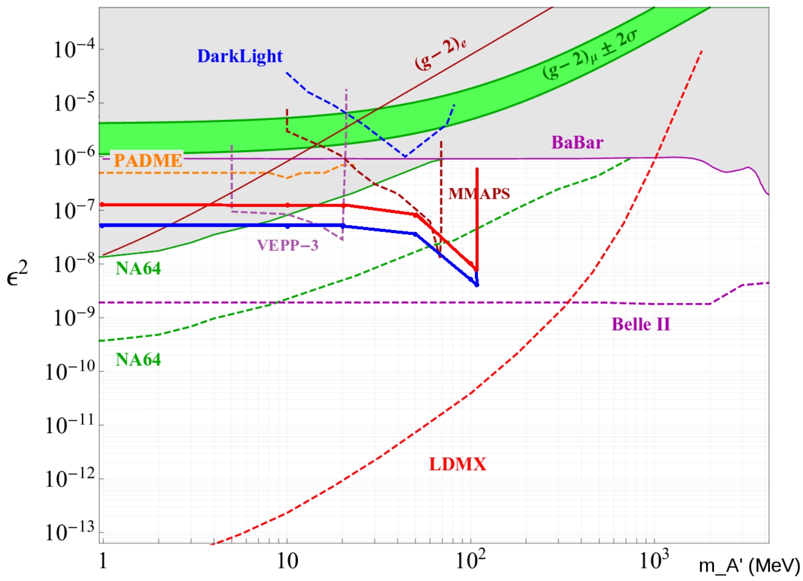


Figure 43. Projected exclusion limits in the $A'$ invisible decay parameter space for a 180 days experiment with a 10 nA (red curve) and 100 nA (blue curve) 11 GeV positron beam at Jefferson Lab.

beam current is considered. $N_s(m_{A'})$ representing the number of expected signal events for a given mass $m_{A'}$ at full coupling, $N_B(m_{A'})$ representing the number of expected total background events within the missing mass in the interval $[m^2_{A'} - 2\sigma(m^2_{A'}); m^2_{A'} + 2\sigma(m^2_{A'})]$, the minimum measurable $\epsilon^2$ coupling writes

$$\epsilon^2_{min}(m_{A'}) = 2\frac{\sqrt{N_B(m_{A'})}}{N_S(m_{A'})} \, . \tag{85}$$

Corresponding in the $(m_{A'}, \epsilon^2)$ phase space are shown in Fig. 43. Even at low positron beam current (10 nA), an $A'$-search experiment at Jefferson Lab will exceed the sensitivity of other current experiments, probing a significant region of the unexplored parameter space. It should be noticed that the sensitivity is maximum for $m_{A'}$ values approaching the total energy in the center of mass frame $\sqrt{s} \simeq \sqrt{2m_e E_{beam}} \simeq 100\,MeV$, due to the $A'$ production enhancement near the resonant regime. We considered here a setup with at a fixed energy beam, but this observation suggests that such an experiment would benefit from a postron beam with variable energy, since the value of $\sqrt{s}$ could be optimized to search for given $m_{A'}$ values.

### *9.5 Summary*

Making use of the future JLab high energy positron beam with a current in the range of tens of nAs, a PADME-like experiment at JLab running over 180 days will extend the $A'$ mass reach up to 100 MeV and will lower the exclusion limit for invisible $A'$ decay by up to a factor of 10 in $\epsilon^2$.

## 10 Conclusions

| | I (nA) | | Beam | Time |
|---|---|---|---|---|
| | $e^-$ | $e^+$ | Polarization | (d) |
| *Two-photon exchange* | | | | |
| TPE @ CLAS12 | 60 | 60 | No | 53 |
| TPE @ Hall A/C | 1000 | 1000 | No | 24 |
| TPE @ SupRos | - | 1000 | No | 18 |
| TPE @ SBS | 10000 | 100 | Yes | |
| *Generalized Parton Distributions* | | | | |
| p-DVCS @ CLAS12 | 75 | 15 | Yes | 83 |
| n-DVCS @ CLAS12 | 60 | 60 | Yes | 80 |
| p-DVCS @ Hall C | - | 5000 | No | 56 |
| *Test of the Standard Model* | | | | |
| Dark photon search | - | 10-100 | No | 180 |
| | | | **Total Data Taking Time** | |

Table 8. Characteristics of a positron experimental program at Jlab.

## References


[Abb16] (PEPPo Collaboration) D. Abbott *et al.* Phys. Rev. Lett. **116** (2016) 214801.

[Add10] P. Adderley *et al.* Phys. Rev. Acc. Beams **13** (2010) 010101.

[Adi15] (CLAS Collaboration) D. Adikaram *et al.* Phys. Rev. Lett. **114** (2015) 062003.

[Afa05] A.V. Afanasev *et al.* Phys. Rev. D **72** (2005) 013008.

[Afa17] A.V. Afanasev *et al.* Prog. Part. Nucl. Phys. **95** (2017) 245.

[Ago03] S. Agostinelli *et al.* Nucl. Inst. Meth. A **506** (2003) 250.

[Akh74] A.I. Akhiezer, M.P. Rekalo, Sov. J. Part. Nucl. **4** (1974) 277.

[Ala09] A. El Alaoui, E. Voutier, CLAS Note **2009-024** (2009).

[Ale08] G. Alexander *et al.* Phys. Rev. Lett. **108** (2008) 210801.

[And94] L. Andivahis *et al.* Phys. Rev. D **50** (1994) 5491.

[And13] ($Q_{weak}$ Collaboration) D. Androić *et al.* Phys. Rev. Lett. **111** (2013) 141803; D. Androić *et al.* Nature **557** (2018) 207.

[Ani06] (HAPPEX Collaboration) K.A. Aniol *et al.* Phys. Rev. Lett. **96** (2006) 022003; K.A. Aniol *et al.* Phys. Lett. B **635** (2006) 275; A. Acha *et al.* Phys. Rev. Lett. **98** (2007) 032301.

[Ani07] I.V. Anikin, O.V. Teryaev, Phys. Rev. D **76** (2007) 056007.

[Ani08] I.V. Anikin, O.V. Teryaev, Fizika B **17** (2008) 151.

[Arn81] R. Arnold, C. Carlson, F. Gross, Phys. Rev. C **23** (1981) 363.

[Arm05] (G0 Collaboration) D.S Amstrong *et al.* Phys. Rev. Lett. **95** (2005) 092001; D. Androić *et al.* Phys. Rev. Lett. **104** (2010) 012001; D. Androić *et al.* Phys. Rev. Lett. **107** (2011) 022501; D. Androić *et al.* Phys. Rev. Lett. **108** (2012) 122002.

[Arr07] J. Arrington, W. Melnitchouk, J.A. Tjon, Phys. Rev. C **76** (2007) 035205.

[Arr11] J. Arrington, P.G. Blunden, W. Melnitchouk, Prog. Part. Nucl. Phys. **66** (2011) 782.

[Bar73] W. Bartel *et al.* Nucl. Phys. B **58** (1973) 429.

[Bat11] M. Battaglieri, R. De Vita, C. Salgado, S. Stepanyan, D. Watts, D. Weygand *et al.* JLab Experiment **E12-11-005** (2011).

[Bel02] A.V. Belitsky, D. Müller, A. Kirchner, Nucl. Phys. B **629** (2002) 323.

[Bel04] A.V. Belitsky, X. Ji, F. Yuan, Phys. Rev. D **69** (2004) 074014.

[Bel05] A.V. Belitsky, A.V. Radyushkin, Phys. Rep. **418** (2005) 1.

[Bel10] A.V. Belitsky, D. Müller, Phys. Rev. D **82** (2010) 074010.

[Ber14] J. C. Bernauer *et al.* Phys. Rev. C **90** (2014) 015206.

[Bet34] H.A. Bethe, W. Heitler, Proc. Roy. Soc. London A **146** (1934) 83.

[Blu03] P.G. Blunden, W. Melnitchouk, J.A. Tjon, Phys. Rev. Lett. **91** (2003) 142304.

[Blu17] P.G. Blunden, W. Melnitchouk, Phys. Rev. C **95** (2017) 065209.

[Bro81] S.J. Brodsky, G.P. Lepage, Phys. Rev. D **22** (1981) 2157.

[Bur02] M. Burkardt, Int. J. Mod. Phys. A **18** (2003) 173.

[Bur07] M. Burkardt, (2007) arXiv:0711.1881.

[Bur18] V. Burkert, L. Elouadrhiri, F.-X. Girod, Nature **557** (2018) 396.

[Car07] C.E. Carlson, M. Vanderhaeghen, Ann. Rev. Nucl. Part. Sci. **57** (2007) 171.

[Che04] Y.C. Chen *et al.* Phys. Rev. Lett. **93** (2004) 122301.

[Che06] (CLAS Collaboration) S. Chen *et al.* Phys. Rev. Lett. **97** (2006)

072002.
[Chr04] M.E. Christy *et al.* Phys. Rev. C **70** (2004) 015206.
[Cra07] C.B. Crawford *et al.* Phys. Rev. Lett. **98** (2007) 052301.
[Def17] (Hall A Collaboration) M. Defurne *et al.* Nature Comm. **8** (2017) 1408.
[Die97] M. Diehl, T. Gousset, B. Pire, J.P. Ralston, Phys. Lett. B **411** (1997) 193.
[Die03] M. Diehl, Phys. Rep. **388** (2003) 41.
[Die05] M. Diehl, S. Sapeta, Eur. Phys. J. C **41** (2005) 515.
[Die07] M. Diehl, D.Y. Ivanov, Eur. Phys. J. C **52** (2007) 919.
[Die09] M. Diehl, *Cont. to the CLAS12 European Workshop* (Genova (Italy), 2009).
[Elo16] L. Elouadrhiri, M. Defurne, F.-X. Girod, F. Sabatié *et al.* JLab Experiment **E12-16-010B** (2016).
[Gas02] A. Gasparian, S. Danagoulian *et al.* JLab Experiment**E02-103** (2002).
[Gav09] (CLAS Collaboration) G. Gavalian, Phys. Rev. C **80** (2009) 035206.
[Gay01] O. Gayou *et al.* Phys. Rev. C **64** (2001) 038202.
[Gay02] (Hall A Collaboration) O. Gayou *et al.* Phys. Rev. Lett. **88** (2002) 092301.
[Gir07] (CLAS Collaboration) F.-X. Girod, Phys. Rev. Lett. **100** (2008) 162002.
[Goe01] K. Goeke, M.V. Polyakov, M.Vanderhaeghen, Prog. Part. Nucl. Phys. **47** (2001) 401.
[Goe07] K. Goeke, J. Grabis, J. Ossmann, M.V. Polyakov, P. Schweitzer, A. Silva, D. Urbano, Phys. Rev. D **75** (2007) 094021.
[Gui03] P.A.M. Guichon, M. Vanderhaeghen, Phys. Rev. Lett. **91** (2003) 142303.
[Gui05] M. Guidal, M.V. Polyakov, A.V. Radyushkin, M. Vanderhaeghen, Phys. Rev. D **72** (2005) 054013.
[Gui08] M. Guidal, Eur. Phys. J. A **37** (2008) 319.
[Gui08-1] P.A.M. Guichon, M. Vanderhaeghen, *Private Communication* (2008).
[Gui13] M. Guidal, H. Moutarde, M. Vanderhaeghen, Rep. Prog. Phys. **76** (2013) 066202.
[Guz06] V. Guzey, T. Teckentrup, Phys. Rev. D **74** (2006) 054027.
[Guz09] V. Guzey, T. Teckentrup, Phys. Rev. D **79** (2009) 017501.
[Hen17] (OLYMPUS Collaboration) B.S. Henderson *et al.* Phys. Rev. Lett. **118** (2017) 092501.
[Hol86] B. Holdom, Phys. Lett. B **166** (1986) 186.
[Hos16] N. d'Hose, S. Niccolai, A. Rostomyan, Eur. Phys. J. A **52** (2016) 151.
[Jag10] C.W. de Jager *et al.* Super BigBite Spectrometer CDR, Jefferson Lab (2010).
[Jag10-1] C.W. de Jager, Int. J. Mod. Phys. E **19** (2010) 844.
[Ji03] X. Ji, Phys. Rev. Lett. **91** (2003) 062001.
[Ji97] X. Ji, Phys. Rev. Lett. **78** (1997) 610.
[Ji97-1] X. Ji, Phys. Rev. D **55** (1997) 7114.
[Ji97-2] X. Ji, W. Melnitchouk, X. Song, Phys. Rev. D **56** (1997) 5511.
[Jo15] (CLAS Collaboration) H.S. Jo, Phys. Rev. Lett. **115** (2015)

212003.
[Jon00] (Hall A Collaboration) M.K. Jones *et al.* Phys. Rev. Lett. **84** (2000) 1398.
[Jon06] M.K. Jones *et al.* Phys. Rev. C **74** (2006) 035201.
[Kim12] H.C. Kim, P. Schweitzer, Phys. Lett. B **718** (2012) 625.
[Kiv01] N. Kivel, M.V. Polyakov, M. Vanderhaeghen, Phys. Rev. D **63** (2012) 114014.
[Kro13] P. Kroll, H. Moutarde, F. Sabatié, Eur. Phys. J C **73** (2013) 2278.
[KubO6] (PrimEx Collaboration) M. Kubantsev, I. Larin, A. Gasparyan, AIP Conf. Proc. **867** (2006) 51.
[Kum10] K. Kumerički, D. Müller, Nucl. Phys. B **841** (2010) 1.
[Kum12] K. Kumerički, D. Müller, DESY-PROC-2012-02 (2012) 236; arXiv:1205.6967.
[Kur08] E.A. Kuraev *et al.* Phys. Rev. C **78** (2008) 015205.
[Lac80] M. Lacombe *et al.* Phys. Rev C **21** (1980) 861.
[Lep80] G.P. Lepage, S.J. Brodsky, Phys. Rev. D **22** (1980) 2157.
[Lia04] (Hall C E94-110 Collaboration) Y. Liang *et al.* (2004) arXiv:nucl-ex/0410027.
[Lit70] J. Litt *et al.* Phys. Lett. B **31** (1970) 40.
[Mac06] G. MacLachlan *et al.* Nucl. Phys. A **764** (2006) 261.
[Mar17] L. Marsicano, AIP Conf. Proc. **1970** (2018) 020008-1.
[Maz07] (Hall A Collaboration) M. Mazouz *et al.* Phys. Rev. Lett. **99** (2007) 242501.
[Max00] L.C. Maximon, J.A. Tjon, Phys. Rev. C **62** (2000) 054320.
[Mez11] (GEp2$\gamma$ Collaboration) M. Meziane *et al.* Phys. Rev. Lett. **106** (2011) 132501.
[Mil98] B.D. Milbrath *et al.* Phys. Rev. Lett. **80** (1998) 452; *err.* Phys. Rev. Lett. **82** 2221.
[Mo69] L.W. Mo, Y.-S. Tsai, Rev. Mod. Phys. **41** (1969) 205.
[Mot13] (CLAS Collaboration) M. Moteabbed *et al.* Phys. Rev. C **88** (2013) 025210.
[Mou13] H. Moutarde (TGV code for fast calculation of DVCS cross sections from CFFs) *Private Communication* (2013).
[Mul94] D. Müller, D. Robaschick, B. Geyer, F.M. Dittes, J. Hořejši, Fortschr. Phys. **42** (1994) 101.
[Mul13] D. Müller, D. Lautenschlager, K. Passek-Kumericki, A. Schäfer, Nucl. Phys. B **884** (2014) 438.
[Mul16] D. Müller, K. Kumerički, http://calculon.phy.pmf.unizg.hr/gpd/, Model 3 (2016).
[Mun06] (Hall A Collaboration) C. Muñ oz Camacho *et al.* Phys. Rev. Lett. **97** (2006) 262002.
[Mun13] C. Muñ oz Camacho, T. Horn, C. Hyde, R. Paremuzyan, J. Roche *et al.* JLab Experiment **E12-13010** (2013).
[Nic11] S. Niccolai, V. Kubarovsky, S. Pisano, D. Sokhan *et al.* JLab Experiment **E12-11-003** (2011).
[Nic15] S. Niccolai, A. Biselli, C. Keith, S. Kuhn, S. Pisano, D. Sokhan *et al.* JLab Experiment **C12-15-004** (2015).
[Omo06] T. Omori et al., Phys. Rev. Lett. **96** (2006) 114801.
[Pao10] M. Paolone *et al.* Phys. Rev. Lett. **105** (2010) 072001.
[Pas14] B. Pasquini, M.V. Polyakov, M. Vanderhaeghen, Phys. Lett. B **739** (2014) 133.

[Pis15] (CLAS Collaboration) S. Pisano *et al.* Phys. Rev. D **91** (2015) 052014.
[Pol99] M.V. Polyakov, C. Weiss, Phys. Rev. D **60** (1999) 114017.
[Pos01] (A1 Collaboration) T. Pospischil *et al.* Eur. Phys. J. A **12** (2001) 125.
[Puc10] (Hall A Collaboration) A.J.R. Puckett *et al.* Phys. Rev. Lett. **104** (2010) 242301.
[Puc12] (Hall A Collaboration) A.J.R. Puckett *et al.*, Phys. Rev. C **85** (2012) 045203.
[Puc17] (Hall A Collaboration) A.J.R. Puckett *et al.* Phys. Rev. C **96** (2017) 055203.
[Puk04] A. Pukhov, (2004) arXiv:hep-ph/0412191.
[Pun05] (Hall A Collaboration) V Punjabi *et al.* Phys. Rev. C **71** (2005) 055202; *err.* Phys. Rev. C **71** (2005) 069902.
[Pun15] V. Punjabi, C.F. Perdrisat, M.K. Jones, E.J. Brash, C.E. Carlson, Eur. Phys. J. A **51** (2015) 79.
[Qat05] I.A. Qattan *et al.* Phys. Rev. Lett. 94 (2005) 142301.
[Rac15] I.A. Rachek *et al.* Phys. Rev. Lett. **114** (2015) 062005.
[Rad96] A.V. Radyushkin, Phys. Lett. B **380** (1996) 417.
[Rad97] A.V. Radyushkin, Phys. Rev. D **56** (1997) 5524.
[Rad13] A.V. Radyushkin, Phys. Rev. D **87** (2013) 096017.
[Rad13-1] A.V. Radyushkin, Phys. Rev. D **88** (2013) 056010.
[Rag14] M. Raggi, V. Kozhuharov, Adv. High Energy Phys.**2014** (2014) 959802; arXiv:1403.3041.
[Rek04] M.P. Rekalo, E. Tomasi-Gustafsson, Nucl. Phys. A **742** (2004) 322.
[Rim17] (CLAS Collaboration) D. Rimal *et al.* Phys. Rev. C **95** (2017) 065201.
[Ron11] G. Ron *et al.* Phys. Rev. C **84** (2011) 055204.
[Ros50] M.N. Rosenbluth, Phys. Rev. **79** (1950) 615.
[Sab11] F. Sabatié, A. Biselli, H. Egiyan, L. Elouadrhiri, M. Holtrop, D. Ireland, K. Wooyoung *et al.* JLab Experiment **E12-06-119** (2006).
[Sed14] (CLAS Collaboration) E. Seder *et al.* Phys. Rev. Lett. **114** (2015) 032001.
[Sok64] A.A. Sokolov, I.M. Ternov, Sov. Phys. Dokl. **8** (1964) 1203.
[Ste01] (CLAS Collaboration) S. Stepanyan *et al.* Phys. Rev. Lett. **87** (2001) 182002.
[Ter05] O.V. Teryaev, (2005) arXiv:hep-ph/0510031.
[Ter16] O.V. Teryaev, Front. Phys. (Beijing) **11** (2016) 111207.
[Tom15] O. Tomalak, M. Vanderhaeghen, Eur. Phys. J. A **51** (2015) 24.
[Tva06] V. Tvaskis, J. Arrington, M.E. Christy, R. Ent, C.E. Keppel, Y. Liang, G. Vittorini, Phys. Rev. C **73** (2006) 025206.
[Van99] M. Vanderhaeghen, P.A.M. Guichon, M. Guidal, Phys. Rev. D **60** (1999) 094017.
[Vou14] E. Voutier, Nuclear Theory **33** (Heron Press, Sofia) (2014) 142; arXiv:1412.1249.
[Wal94] R.C. Walker *et al.* Phys. Rev. D **49** (1994) 5671.
[Woj09] B. Wojtsekhowski, AIP Conf. Proc. **1160** (2009) 149.
[Woj17] B. Wojtsekhowski *et al.* (2017) arXiv:1708.07901.
[You06] R.D. Young, J. Roche, R.D. Carlini, A.W. Thomas, Phys. Rev. Lett. **97** (2006) 102002.
[Yur17] M. Yurov, J. Arrington, arXiv:1712.07171.

[Zha11] X. Zhan *et al.* Phys. Lett. B **705** (2011) 59.
[Zhe09] X. Zheng, AIP Conf. Proc. **1160** (2009) 160.